Chapter 2
Interaction of Polarizable Particles with Light

More light!—Johann Wolfgang von Goethe's last words

A proper understanding of the mechanics and susceptibility of nanoparticles under the influence of coherent light fields will be a core ingredient throughout this thesis. It will be required for the description of new matter-wave interferometry schemes and of optical methods to manipulate the motion or measure the optical properties of molecules and clusters. This chapter is dedicated to the light-matter interaction in the presence of coherent laser fields, of high-finesse cavity modes and, not least, of a (thermally occupied) radiation field. The latter will mainly be useful to describe decoherence processes by the emission, absorption and scattering of photons, whereas the coherent interaction with laser fields and cavity modes is the basis of optical interference gratings and cavity-induced slowing and trapping methods.

I will start by introducing the basic effect of coherent light fields on the center-of-mass motion of small particles in Sect. 2.1. In the limit of short interaction times this directly leads to the description of optical gratings, as commonly used in matter-wave interferometry. I will proceed with the more complex long-time dynamics of polarizable point particles (PPP) coupled to strong laser fields in Sect. 2.2, where I will present in detail the influence of high-finesse cavity modes. They can be used to dissipatively slow down single particles, or to cool the motion of a hot ensemble of particles, respectively [1].

In Sect. 2.3 I eventually take a step beyond the point-particle approximation and study the effect of standing-wave fields on wavelength-sized dielectric spheres using Mie theory [2, 3]. The results derived there will be directly applied in Sect. 2.3.3 where I discuss the radial slowing and trapping of microspheres in a strongly pumped cavity mode.

2.1 Mechanics of Polarizable Point Particles in Coherent Light Fields

In a first and most elementary approach to the light-matter problem let us study the classical and quantum dynamics of a polarizable point particle (PPP) in the presence of a classical electromagnetic field mode. The point-particle idealization is considered valid in many experimental situations where subwavelength molecules or clusters are coupled to high-intensity light fields of laser beams or strongly pumped cavity modes. Consequences and applications of the basic effect are discussed here, before the restriction to point particles and classical light fields will successively be lifted in the next sections.

For the moment let us represent the light by a single-mode electric and magnetic field

$$\boldsymbol{E}\left(\boldsymbol{r}, t\right) = E_0 e^{-i\omega t} \boldsymbol{u}\left(\boldsymbol{r}\right), \qquad \boldsymbol{H}\left(\boldsymbol{r}, t\right) = \frac{E_0}{i\mu_0\omega} e^{-i\omega t} \nabla \times \boldsymbol{u}\left(\boldsymbol{r}\right) \qquad (2.1)$$

with a harmonic time dependence on the frequency $\omega = ck$. It will be convenient to work with complexified fields and allow for complex mode-polarization functions $\boldsymbol{u}\left(\boldsymbol{r}\right) \in \mathbb{C}$, as discussed in Appendix A.1. The physical fields are then represented by the real parts $\mathfrak{Re}\left\{\boldsymbol{E}\right\}$ and $\mathfrak{Re}\left\{\boldsymbol{H}\right\}$. We will mostly deal with the important case of linearly polarized standing or running waves,

$$\boldsymbol{E}_{\mathrm{sw}}\left(\boldsymbol{r}, t\right) = E_0 e^{-i\omega t} \boldsymbol{e}_x f\left(x, y\right) \cos\left(kz\right), \quad \boldsymbol{H}_{\mathrm{sw}}\left(\boldsymbol{r}, t\right) = \frac{iE_0}{\mu_0 c} e^{-i\omega t} \boldsymbol{e}_y f\left(x, y\right) \sin\left(kz\right),$$
$$(2.2)$$

$$\boldsymbol{E}_{\mathrm{rw}}\left(\boldsymbol{r}, t\right) = E_0 \boldsymbol{e}_x f\left(x, y\right) \exp\left(ikz - i\omega t\right), \quad \boldsymbol{H}_{\mathrm{rw}}\left(\boldsymbol{r}, t\right) = \frac{E_0}{\mu_0 c} \boldsymbol{e}_y f\left(x, y\right) \exp\left(ikz - i\omega t\right),$$
$$(2.3)$$

with $f\left(x, y\right)$ the transverse mode profile. Realistic light fields occupy only a finite region in space, as described by their mode volume $V = \int \mathrm{d}^3 r \, |\boldsymbol{u}\left(\boldsymbol{r}\right)|^2$, and we may associate with the field of strength E_0 a complex amplitude $\alpha = \sqrt{\varepsilon_0 V / 2\hbar\omega} E_0$ and a mean photon number $|\alpha|^2$. With this the Hamiltonian, that is, the field energy contained in the mode, takes the well-known form

$$H_{\mathrm{f}} = \frac{1}{2} \int_V \mathrm{d}^3 r \left[\varepsilon_0 \mathfrak{Re}\left\{\boldsymbol{E}\left(\boldsymbol{r}, t\right)\right\}^2 + \mu_0 \mathfrak{Re}\left\{\boldsymbol{H}\left(\boldsymbol{r}, t\right)\right\}^2\right] = \frac{\hbar\omega}{2}\left(\alpha^*\alpha + \alpha\alpha^*\right) = \hbar\omega |\alpha|^2.$$
$$(2.4)$$

The amplitude is replaced by the photon annihilation operator a when generalizing to quantum fields. A Gaussian mode[1] is described by two waist parameters w_x, w_y and the transverse mode profile $f\left(x, y\right) = \exp\left(-x^2/w_x^2 - y^2/w_y^2\right)$.

---

[1] The full mathematical description of Gaussian light fields, as generated by focused laser beams or found in curved-mirror cavities, is a little bit more involved than presented here. I give a detailed formula for symmetric Gaussian mode functions with $w_x = w_y = w$ in Appendix A.2. Strictly speaking, the above representations (2.2) and (2.3) are zeroth order approximations of the Gaussian

2.1.1 The Linear Response of a Polarizable Point Particle to Light

In order to model the interaction of a polarizable point particle with harmonic light fields one generally associates to the particle a scalar polarizability $\chi = \chi(\omega)$, which represents its linear response to the electric light field E. In most cases beyond the level of a single atom, the polarizability is taken to be a phenomenological frequency-dependent parameter.[2] It determines the induced electric dipole moment $d = \chi E$ and the associated Lorentz force [6], $F(r, t) = (\mathfrak{Re}\{d\} \cdot \nabla)\,\mathfrak{Re}\{E\} + \mu_0 \mathfrak{Re}\{\partial_t d\} \times \mathfrak{Re}\{H\}$. It involves only real physical quantities. The first term represents the net Coulomb force of the electric field component $E(r)$ acting on the dipole d at position r, whereas the second term describes the force exerted by the magnetic field component $H(r')$ on the associated current density $j(r') = \partial_t d\delta(r - r')$. We find that the overall force oscillates rapidly at the given optical frequency, and it is therefore expedient to restrict to the time-averaged expression[3]

$$
\begin{aligned}
\langle F(r) \rangle_t &= \left\langle \left(\mathfrak{Re}\left\{\chi E(r)\,e^{-i\omega t}\right\} \cdot \nabla\right)\mathfrak{Re}\left\{E(r)\,e^{-i\omega t}\right\}\right\rangle_t \\
&\quad + \left\langle \mu_0 \mathfrak{Re}\left\{-i\omega\chi E(r)\,e^{-i\omega t}\right\} \times \mathfrak{Re}\left\{H(r)\,e^{-i\omega t}\right\}\right\rangle_t \\
&= \frac{1}{2}\mathfrak{Re}\left\{\chi\,[E(r) \cdot \nabla]\,E^*(r)\right\} + \frac{1}{2}\mathfrak{Re}\left\{\chi E(r) \times [\nabla \times E^*(r)]\right\} \\
&= \frac{\mathfrak{Re}\{\chi\}}{4}\nabla |E(r)|^2 - \frac{\mathfrak{Im}\{\chi\}}{2}\mathfrak{Im}\left\{[\nabla \circ E^*(r)]\,E(r)\right\}.
\end{aligned}
\tag{2.5}
$$

In the absence of absorption, $\mathfrak{Im}\{\chi\} = 0$, the average force is conservative, and it can be written as the negative gradient of the time-averaged dipole interaction potential,

$$
H_{\text{int}}(r) = -\frac{1}{4}\mathfrak{Re}\{\chi\}\,|E(r)|^2.
\tag{2.6}
$$

The second term in (2.5) represents the non-conservative radiation pressure force related to the net absorption of field momentum per time. It appears only in the

---

(Footnote 1 continued)
mode fields in the waist parameter $1/kw$, and additional polarization components must be taken into account for higher orders.

[2] Note that the light-atom interaction can also be modeled by a complex linear polarizability provided the light is far detuned from any internal electronic transition and the transition is not strongly driven. In the latter case the atom's response saturates at sufficiently high field intensities, as described by the Jaynes-Cummings model [4, 5].

[3] The vector identities [7],

$$
\begin{aligned}
\nabla(a \cdot b) &= a \times (\nabla \times b) + b \times (\nabla \times a) + (b \cdot \nabla)a + (a \cdot \nabla)b, \\
(\nabla \circ b)a &= a \times (\nabla \times b) + (a \cdot \nabla)b,
\end{aligned}
$$

might occasionally be useful here and in the following. The dyadic term $B = \nabla \circ b$ is defined as the matrix $B_{jk} = \partial b_k/\partial x_j$.

case of complex running-wave fields with a directed momentum flux, and it acts only on particles with a nonzero light absorption cross-section $\sigma_{abs} = \sigma_{abs}(\omega)$, which determines the imaginary part of the complex polarizability χ. We find the relation $\sigma_{abs} = k\Im\{\chi\}/\varepsilon_0$ between both parameters by looking at the average power absorbed by the dipole. It is determined by the average rate of work the field does on the dipole [7, 8],

$$P_{abs}(\boldsymbol{r}) = \left\langle \int d^3r' \, \Re\{\boldsymbol{j}(\boldsymbol{r}', t)\} \cdot \Re\{\boldsymbol{E}(\boldsymbol{r}', t)\} \right\rangle_t = \frac{1}{2}\Re\{[\partial_t \boldsymbol{d}(\boldsymbol{r})]^* \cdot \boldsymbol{E}(\boldsymbol{r})\}$$

$$= \frac{\omega}{2}\Im\{\chi\}|\boldsymbol{E}(\boldsymbol{r})|^2 = \sigma_{abs}I(\boldsymbol{r}), \qquad (2.7)$$

with $I(\boldsymbol{r}) = c\varepsilon_0 |\boldsymbol{E}(\boldsymbol{r})|^2/2$ the local electric field intensity.

Another contribution to the radiation pressure effect on the particle is due to the Rayleigh scattering of light from the coherent field into free space. The absorption cross-section σ_{abs} is thus complemented by the elastic light scattering cross-section $\sigma_{sca} = k^4 |\chi|^2/6\pi\varepsilon_0^2$, as given by the total radiated power of the oscillating dipole [8],

$$P_{sca}(\boldsymbol{r}) = \frac{\omega^4}{12\pi\varepsilon_0 c^3}|\boldsymbol{d}|^2 = \frac{ck^4|\chi|^2}{12\pi\varepsilon_0}|\boldsymbol{E}(\boldsymbol{r})|^2 = \sigma_{sca}I(\boldsymbol{r}). \qquad (2.8)$$

The cross-section $\sigma_{ext} = \sigma_{abs} + \sigma_{sca}$ describes the combined extinction of the light by absorption and Rayleigh scattering. The influence of Rayleigh scattering on the force (2.5) can usually be neglected for point-like particles of diameter $a \ll \lambda$. Since their polarizability is roughly determined by the volume, $\chi \sim a^3$, the scattering contribution to the total force is then strongly suppressed by the factor $(ka)^3 \ll 1$.

The conservative part of the interaction generalizes to the case of a quantum particle in a straightforward manner; we simply replace the position $\boldsymbol{r}$ by the operator $\mathbf{r}$ and add the dipole potential $H_{int}(\mathbf{r})$ to the Hamiltonian of the free particle,

$$\mathsf{H}_{PPP} = \frac{\mathbf{p}^2}{2m} - \frac{\Re\{\chi\}}{4}|\boldsymbol{E}(\mathbf{r})|^2 = \frac{\mathbf{p}^2}{2m} + \hbar U_0 |\alpha|^2 |\boldsymbol{u}(\mathbf{r})|^2. \qquad (2.9)$$

In the second equation I have introduced the coupling frequency

$$U_0 = -\frac{\omega}{2\varepsilon_0 V}\Re\{\chi\}, \qquad (2.10)$$

which represents the single-photon interaction strength or, in the case of a high-finesse cavity field, the cavity resonance shift due to the presence of the particle. A full quantum treatment of both light and matter is obtained by replacing $|\alpha|^2 \rightarrow \mathsf{a}^\dagger \mathsf{a}$ and adding the single-mode Hamiltonian $\mathsf{H}_f = \hbar\omega\mathsf{a}^\dagger\mathsf{a}$.

The quantum counterpart of the non-conservative light-matter interaction cannot be obtained by such simple means as it cannot be expressed in terms of the particle's Hamilton operator. We expect that, apart from exerting a net radiation pressure

force, it also contributes a diffusion in momentum space as the particle randomly absorbs and scatters single photons from the field mode. That is to say, the full quantum dynamics of the particle must be phrased in terms of a Lindblad-type master equation [9, 10].

2.1.2 Absorption, Emission and Rayleigh Scattering of Photons

A physical derivation of the nonconservative radiation pressure forces, of momentum diffusion and the associated decoherence effects requires a full quantum description of the coupling to both the coherent light field and the free-space mode vacuum. This will be given in Sect. 2.2. At this point we take a more intuitive, operational approach to arrive at the same results based on a formulation in terms of quantum jumps [10].

The absorption, emission, or scattering of single photons can be understood as a stochastic Poisson process, where the random variable $N(t) \in \mathbb{N}_0$ denotes the number of absorbed, emitted, or scattered photons at each point in time t starting from $N(0) = 0$. Given a mean rate of events Γ the Poisson process is determined by the time evolution of the probability $P(n, t)$ of counting a total of n events until time t,

$$\frac{\mathrm{d}}{\mathrm{d}t} P(n, t) = \Gamma \left[P(n-1, t) - P(n, t) \right], \quad P(n, 0) = \delta_{n,0}. \qquad (2.11)$$

As time evolves, the number of events increases stepwise by the increment $\mathrm{d}N(t) = N(t + \mathrm{d}t) - N(t) \in \{0, 1\}$ in each coarse-grained time step[4] $\mathrm{d}t$, with the expectation value $\mathcal{E}[\mathrm{d}N(t)] = \Gamma \mathrm{d}t$.

The binary random variable $\mathrm{d}N(t) = \mathrm{d}N^2(t)$ can now be employed in the stochastic time evolution of the quantum state of motion $|\psi(t)\rangle$ of a particle absorbing, emitting or scattering photons at an average rate Γ. Let us suppose that the system state undergoes the transition $|\psi\rangle \mapsto \mathsf{A}|\psi\rangle / \langle\psi|\mathsf{A}^\dagger\mathsf{A}|\psi\rangle^{1/2}$ in the case of an event (which would correspond to a momentum kick in our case), while it evolves coherently under the influence of the Hamiltonian H otherwise. The random trajectory of the system state is then described by the stochastic Schrödinger equation [10]

$$\mathrm{d}|\psi(t)\rangle = \left(-\frac{i}{\hbar}\mathsf{H} + \Gamma \frac{\langle\psi(t)|\mathsf{A}^\dagger\mathsf{A}|\psi(t)\rangle - \mathsf{A}^\dagger\mathsf{A}}{2} \right) |\psi(t)\rangle \mathrm{d}t$$

$$+ \left(\frac{\mathsf{A}}{\sqrt{\langle\psi(t)|\mathsf{A}^\dagger\mathsf{A}|\psi(t)\rangle}} - 1 \right) |\psi(t)\rangle \mathrm{d}N(t), \qquad (2.12)$$

---

[4] Stochastic differential equations can serve to describe the effective time evolution of open systems in contact with an environment inducing rapid (uncontrollable) state transitions that cannot be examined with the coarse-grained time resolution of observation [9]. The transitions thus show up as random events, or 'jumps'. Using a Poissonian model we assume single infrequent jumps that can be clearly distinguished.

where the antihermitian addition to the coherent time evolution in the first line ensures norm conservation. An ensemble average over all random trajectories leads to a master equation for the motional state ρ of the system, which is of the renowned Lindblad form,

$$\partial_t \rho = -\frac{i}{\hbar} \left[\mathsf{H}, \rho \right] + \Gamma \left(\mathsf{A}\rho\mathsf{A}^\dagger - \frac{1}{2} \left\{ \mathsf{A}^\dagger\mathsf{A}, \rho \right\} \right) =: -\frac{i}{\hbar} \left[\mathsf{H}, \rho \right] + \mathcal{L}(\rho). \quad (2.13)$$

Additional Lindblad superoperators $\mathcal{L}$ appear in the presence of several statistically independent jump processes influencing the system.

We are left with specifying the rate constants Γ and the jump operators A of the Lindblad terms that correspond to photon absorption, emission and scattering at a PPP,

$$\partial_t \rho = -\frac{i}{\hbar} \left[\mathsf{H}_{\mathrm{PPP}}, \rho \right] + \mathcal{L}_{\mathrm{abs}}(\rho) + \mathcal{L}_{\mathrm{emi}}(\rho) + \mathcal{L}_{\mathrm{sca}}(\rho) \quad (2.14)$$

2.1.2.1 Photon Absorption

Complex polarizabilities represent point-like particles that absorb light. Dividing the average absorption power (2.7) by the energy of a single photon yields the rate constant $\Gamma_{\mathrm{abs}} = P_{\mathrm{abs}}/\hbar\omega = \gamma_{\mathrm{abs}} |\alpha|^2$, which can be expressed as a product of the photon number in the field times the *single-photon absorption rate* $\gamma_{\mathrm{abs}} = c\sigma_{\mathrm{abs}}/V = \omega\mathfrak{Im}\{\chi\}/\varepsilon_0 V$.

Each absorbed photon modifies the particle momentum state according to the mode function $\boldsymbol{u}(\boldsymbol{r})$ of the coherent light field. In the simple case of a plane wave, for instance, the absorbed photon shifts the particle by $\hbar\boldsymbol{k}$ in momentum space, so that the jump operator reads as $\mathsf{A} = \exp(i\boldsymbol{k} \cdot \mathbf{r})$. Different mode structures emerge when plane waves are reflected and transmitted at particular geometries. We restrict our view here to modes with a fixed (linear, circular or elliptic) polarization vector, $\boldsymbol{u}(\boldsymbol{r}) = \boldsymbol{\epsilon}u(\boldsymbol{r})$. The spatial structure of the mode is then contained in the scalar mode function[5] $u(\boldsymbol{r})$, which can be decomposed into a Fourier sum of polarized plane-wave components, $u(\boldsymbol{r}) = \sum_{\boldsymbol{k}} u_{\boldsymbol{k}} \exp(i\boldsymbol{k} \cdot \boldsymbol{r})$. The momentum components $u_{\boldsymbol{k}}$ being indistinguishable, photon absorption transforms a momentum state $|\boldsymbol{p}\rangle$ of the particle into the superposition state

$$|\boldsymbol{p}\rangle \mapsto \sum_{\boldsymbol{k}} u_{\boldsymbol{k}} |\boldsymbol{p} + \hbar\boldsymbol{k}\rangle = \sum_{\boldsymbol{k}} u_{\boldsymbol{k}} e^{i\boldsymbol{k} \cdot \mathbf{r}} |\boldsymbol{p}\rangle = u(\mathbf{r}) |\boldsymbol{p}\rangle, \quad (2.15)$$

---

[5] Using a fixed polarization $\boldsymbol{\epsilon}(\boldsymbol{r}) = \boldsymbol{\epsilon}$ is a good approximation in many practical cases such as Gaussian TEM modes, where position-dependent corrections are negligibly small. A detailed description of modes with a position-dependent polarization vector is more involved and requires a specific physical model of the particle's response during the absorption process. This is because the orientation of the induced dipole moment then contains information about the position of the particle in the field mode, which is traced out when only the center-of-mass state is monitored.

accordingly. The jump operator is thus given by $\mathsf{A} = u(\mathbf{r})$, and the corresponding Lindblad term of photon absorption reads as

$$\mathcal{L}_{\mathrm{abs}}(\rho) = \gamma_{\mathrm{abs}} |\alpha|^2 \left[u(\mathbf{r}) \rho u^*(\mathbf{r}) - \frac{1}{2} |u(\mathbf{r})|^2 \rho - \frac{1}{2} \rho |u(\mathbf{r})|^2 \right]. \qquad (2.16)$$

Note that this form of the superoperator fully accounts for the local intensity distribution of the field. If the particle state is localized, say, at the node of a standing-wave field (2.2), where the mode function vanishes, the Lindblad term will not contribute to the master equation of the particle. In contrast, the particle is most strongly affected in the antinodes.

From the resulting master equation $\partial_t \rho = -i \left[\mathsf{H}_{\mathrm{PPP}}, \rho \right] / \hbar + \mathcal{L}_{\mathrm{abs}}(\rho)$ we can deduce the mean force acting on the particle by means of the Ehrenfest theorem. The time derivative of the momentum operator expectation value in the Heisenberg picture should correspond to the expected classical force expression (2.5). A straightforward calculation (using the commutator identity $\left[\mathbf{p}, f(\mathbf{r}) \right] = -i\hbar \nabla f(\mathbf{r})$) reveals that this is indeed the case,

$$\begin{aligned}
\partial_t \langle \mathbf{p} \rangle &= \mathrm{tr} \left(-\frac{i}{\hbar} \mathbf{p} \left[\mathsf{H}_{\mathrm{PPP}}, \rho \right] + \mathbf{p} \mathcal{L}_{\mathrm{abs}}(\rho) \right) \\
&= \frac{i}{\hbar} \left\langle \left[H_{\mathrm{int}}(\mathbf{r}), \mathbf{p} \right] \right\rangle + \frac{\gamma_{\mathrm{abs}}}{2} |\alpha|^2 \left\langle \left[u^*(\mathbf{r}), \mathbf{p} \right] u(\mathbf{r}) + u^*(\mathbf{r}) \left[\mathbf{p}, u(\mathbf{r}) \right] \right\rangle \\
&= -\hbar U_0 |\alpha|^2 \left\langle \nabla |u(\mathbf{r})|^2 \right\rangle + \hbar \gamma_{\mathrm{abs}} |\alpha|^2 \left\langle \mathfrak{Im} \left\{ u^*(\mathbf{r}) \nabla u(\mathbf{r}) \right\} \right\rangle \\
&= \frac{\mathfrak{Re}\{\chi\}}{4} \left\langle \nabla |\mathbf{E}(\mathbf{r})|^2 \right\rangle - \frac{\mathfrak{Im}\{\chi\}}{2} \left\langle \mathfrak{Im} \left\{ \left[\nabla \circ \mathbf{E}^*(\mathbf{r}) \right] \mathbf{E}(\mathbf{r}) \right\} \right\rangle, \qquad (2.17)
\end{aligned}$$

with the electric field $\mathbf{E}(\mathbf{r}) = E_0 \boldsymbol{\epsilon} u(\mathbf{r})$. The absorption superoperator (2.16) reproduces the classical radiation pressure force correctly, but it also contributes a diffusion of the particle momentum. The time derivative of the energy expectation value $\partial_t \langle \mathsf{H}_{\mathrm{PPP}} \rangle$ becomes non-zero due to the presence of the absorption-induced momentum diffusion,[6]

$$\begin{aligned}
\partial_t \langle \mathsf{H}_{\mathrm{PPP}} \rangle &= \mathrm{tr} \left(\frac{\mathbf{p}^2}{2m} \mathcal{L}_{\mathrm{abs}}(\rho) \right) = \frac{\gamma_{\mathrm{abs}} |\alpha|^2}{4m} \left\langle \left[u^*(\mathbf{r}), \mathbf{p}^2 \right] u(\mathbf{r}) + u^*(\mathbf{r}) \left[\mathbf{p}^2, u(\mathbf{r}) \right] \right\rangle \\
&= \frac{\hbar \gamma_{\mathrm{abs}} |\alpha|^2}{m} \left\langle \mathfrak{Im} \left\{ u^*(\mathbf{r}) \nabla u(\mathbf{r}) \right\} \cdot \mathbf{p} \right\rangle + \frac{\hbar^2 \gamma_{\mathrm{abs}} |\alpha|^2}{2m} \left\langle |\nabla u(\mathbf{r})|^2 \right\rangle. \quad (2.18)
\end{aligned}$$

The first term is related to the radiation pressure force exerted by directed running waves; it vanishes in the case of standing-wave modes $u(\mathbf{r}) \in \mathbb{R}$. The positive second term is always present, it describes the heating of the particle by momentum

---

[6] Here I have used the identity $\left[\mathbf{p}^2, f(\mathbf{r}) \right] = -\hbar^2 \Delta f(\mathbf{r}) - 2i\hbar \nabla f(\mathbf{r}) \cdot \mathbf{p} = \hbar^2 \Delta f(\mathbf{r}) - 2i\hbar \mathbf{p} \cdot \nabla f(\mathbf{r})$, as well as the fact that the mode function by construction solves the Helmholtz equation $\Delta u = -k^2 u$.

diffusion, and it represents the main quantum correction to the classical derivation of the non-conservative radiation pressure force.

This raises the question as to whether, or when, the diffusion correction becomes relevant in practice. Given that the mode function solves the Helmholtz equation $\Delta u = -k^2 u$ we can estimate the magnitude of the gradient by $|\nabla u| \sim k$, which leads to an energy increase per time of the order of $\gamma_{\text{abs}} |\alpha|^2 \, \hbar^2 k^2 / 2m = \Gamma_{\text{abs}} \hbar \omega_r$ due to diffusion. That is, the energy grows at the total absorption rate Γ_{abs} in units of the so-called *recoil energy* $\hbar \omega_r = \hbar^2 k^2 / 2m$, or *recoil frequency* ω_r if units of $\hbar$ are discarded. This diffusion heating must be compared to the rate of change in potential energy $\sim 2\hbar k v U_0 |\alpha|^2$ when the particle is moving at the velocity v. The ratio of non-conservative heating to the conservative change in potential energy $\gamma_{\text{abs}} \omega_r / 2U_0 k v$ then scales as the quotient of recoil frequency over Doppler frequency $\omega_r / kv = \hbar k / 2mv$—a tiny quantity in many practical cases dealing with fast and large molecules or clusters.

The diffusion effect becomes relevant in the quantum limit of motion, where particles are so slow that their momentum $p = mv$ becomes comparable to the photon momentum $\hbar k$. The minimal kinetic energy a particle can reach in the presence of the photon field is then given by the recoil energy $\hbar \omega_r$. The absorption, emission, or scattering of photons induces a random walk in momentum space and thereby prevents the particle from reaching even lower velocities.

A purely classical treatment of the radiation pressure forces may suffice far above the quantum limit as long as decoherence is of no concern. On the other hand, if the particle is prepared in a nonclassical state of motion, the Lindblad superoperator (2.16) accounts for the coherence loss due to photon absorption.

2.1.2.2 Photon Emission into Free Space

The discussed absorption model eventually runs into constraints once the total absorbed photon energy during the time scale of the experiment reaches a critical level where it significantly modifies or destroys the internal structure of the particle such that the linear response regime breaks down.

On the other hand, an internally hot or excited particle may gradually reduce its internal energy by fluorescence or thermal emission of radiation, which results in a similar diffusion and decoherence effect as in the absorption process. The associated Lindblad term can be modeled as a random unitary process [11]. Each emitted photon with a wave vector $\boldsymbol{k}$ exerts a momentum kick of $-\hbar \boldsymbol{k}$ onto the particle, as described by the unitary transformation $\mathsf{U}_{\boldsymbol{k}} = \exp(-i\boldsymbol{k} \cdot \mathbf{r})$. Given the spectral emission rate $\gamma_{\text{emi}}(\omega)$ and the normalized angular distribution $R(\boldsymbol{n})$ of the emitted radiation, $\int_{|\boldsymbol{n}|=1} \mathrm{d}^2 n \, R(\boldsymbol{n}) = 1$, the Lindblad term reads as

$$\mathcal{L}_{\text{emi}}(\rho) = \int\limits_0^\infty \mathrm{d}\omega \, \gamma_{\text{emi}}(\omega) \left[\int \mathrm{d}^2 n \, R(\boldsymbol{n}) \, e^{-i\omega \boldsymbol{n} \cdot \mathbf{r}/c} \rho \, e^{i\omega \boldsymbol{n} \cdot \mathbf{r}/c} - \rho \right]. \qquad (2.19)$$

While the details on the radiation spectrum $\gamma_{\text{emi}}(\omega)$ and pattern $R(\boldsymbol{n})$ depend on the nature of the emission process, we should certainly expect that there is no preferred direction of emission, $\int d^2n\, R(\boldsymbol{n})\, \boldsymbol{n} = 0$. This is fulfilled in the case of an isotropic radiation pattern, $R(\boldsymbol{n}) = 1/4\pi$. As a consequence, the emission process does not contribute another net force term to (2.17), but it naturally contributes to the momentum diffusion effect,

$$\left\langle \mathbf{p}^2 \mathcal{L}_{\text{emi}}(\rho) \right\rangle = \int\limits_0^\infty d\omega\, \gamma_{\text{emi}}(\omega) \left(\frac{\hbar\omega}{c} \right)^2, \tag{2.20}$$

as well as to decoherence. For instance, nondiagonal elements in the position representation decay like

$$\langle \boldsymbol{r} | \mathcal{L}_{\text{emi}}(\rho) | \boldsymbol{r}' \rangle = - \int\limits_0^\infty d\omega\, \gamma_{\text{emi}}(\omega) \left[1 - \int d^2n\, R(\boldsymbol{n}) \exp\left(-i\omega\boldsymbol{n} \cdot \frac{\boldsymbol{r} - \boldsymbol{r}'}{c} \right) \right] \langle \boldsymbol{r} | \rho | \boldsymbol{r}' \rangle \tag{2.21}$$

due to emission. The decay saturates at the maximum rate $\Gamma_{\text{emi}} = \int d\omega\, \gamma_{\text{emi}}(\omega)$ for nondiagonal elements that are further apart than the spectrum of emitted wavelengths. We can distinguish between three types of emission spectra:

- **Fluorescence** Some species of excited molecules or clusters may get rid of their excess energy by emitting a fluorescence photon, which typically happens within nanoseconds after the excitation [12]. The emission spectrum is expected to be narrow, but it is often red-shifted with respect to the excitation energy due to fast internal relaxation before reemission. In fact, these energy conversion processes may be so efficient that the particle hardly fluoresces at all. One generally observes a low *quantum yield of fluorescence* $P_{\text{fluo}} \ll 1$ in a variety of complex organic molecules which may even absorb energies beyond the ionization threshhold emitting neither an electron nor a fluorescence photon [13, 14]. Such particles then simply heat up internally and will cool down slowly by thermal radiation.
- **Thermal radiation of a hot particle** Large and hot particles with many internal degrees of freedom can be regarded as a (microcanonical) heat bath of fixed energy [15]. Neglecting small corrections due to the finite number of excited degrees of freedom (finite heat capacitance $C_V < \infty$), we may approximate the particle as a canonical heat bath at a temperature T that is much higher than the temperature T_0 of the environment. The particle can thus freely emit photons into the essentially unoccupied free-space radiation field, at a rate given by the spectral free-space mode density, the frequency-dependent photon absorption (and emission) cross-section $\sigma_{\text{abs}}(\omega)$ and a Boltzmann factor relating the internal density of states before and after the emission of $\hbar\omega$ [16],

$$\gamma_{\text{emi}}(\omega) = \frac{\omega^2 \sigma_{\text{abs}}(\omega)}{\pi^2 c^2} \exp\left(-\frac{\hbar\omega}{k_B T} \right). \tag{2.22}$$

If thermal emission is to be observed over a long period of time the gradual temperature decrease must be taken into account, which may also impact the absorption cross section.

- **Blackbody radiation in thermal equilibrium** The radiation spectrum changes if the particle and the environment are in thermal equilibrium, $T = T_0$. We may then approximate the particle as a blackbody radiator with an aperture given by its photon absorption cross section, and the emission spectrum is of the well-known Planck form

$$\gamma_{\text{emi}}(\omega) = \frac{\omega^2 \sigma_{\text{abs}}(\omega)}{\pi^2 c^2} \left[\exp\left(\frac{\hbar\omega}{k_B T} \right) - 1 \right]^{-1}. \tag{2.23}$$

The particle becomes a colored body if finite-size corrections are taken into account [16].

2.1.2.3 Elastic Light Scattering into Free Space

The effect of Rayleigh scattering on the particle can now be understood as a combination of photon absorption from the coherent light field followed by a reemission of the same energy into free space. Hence, the net momentum transfer of a single scattering event is described by applying the mode function operator $u(\mathbf{r})$ times the unitary operator $\exp(-i\mathbf{k} \cdot \mathbf{r})$ on the particle state, with $|\mathbf{k}| = k$ the wave number of the original light mode. Averaging over all possible scattering directions (in the same way as in the emission case (2.19)) yields the Lindblad term

$$\mathcal{L}_{\text{sca}}(\rho) = \gamma_{\text{sca}} |\alpha|^2 \left[\int d^2n\, R(\mathbf{n})\, u(\mathbf{r})\, e^{-ik\mathbf{n}\cdot\mathbf{r}} \rho e^{ik\mathbf{n}\cdot\mathbf{r}} u^*(\mathbf{r}) - \frac{1}{2} \left\{ |u(\mathbf{r})|^2, \rho \right\} \right], \tag{2.24}$$

with the single-photon scattering rate $\gamma_{\text{sca}} = ck^4 |\chi|^2 / 6\pi\varepsilon_0^2 V$. The Rayleigh scattering pattern of the PPP is that of a radiating dipole [8], $R(\mathbf{n}) = 3\sin^2\theta/8\pi$, where θ denotes the angle of $\mathbf{n}$ with respect to the polarization direction $\boldsymbol{\epsilon}$ of the electric field (and therefore of the induced dipole).

Rayleigh scattering contributes to both the radiation pressure force and the momentum diffusion effect. The former has the same form as the absorption term in (2.17), as is immediately understood by viewing a scattering event as a subsequent absorption and emission process. The latter does not induce any net force since there is no preferred direction of emission, $\int d^2n\, R(\mathbf{n})\, \mathbf{n} = 0$.

In summery, we find that the total non-conservative radiation-pressure part of the force on a PPP reads as

$$\mathbf{F}_{\text{nc}} = \langle \mathbf{p} \left[\mathcal{L}_{\text{abs}}(\rho) + \mathcal{L}_{sca}(\rho) \right] \rangle = \hbar (\gamma_{\text{abs}} + \gamma_{\text{sca}}) |\alpha|^2 \left\langle \Im \left\{ u^*(\mathbf{r}) \nabla u(\mathbf{r}) \right\} \right\rangle. \tag{2.25}$$

It complements the conservative force from the optical potential, $\mathbf{F}_{\text{c}} = -\hbar U_0 |\alpha|^2 \left\langle \nabla |u(\mathbf{r})|^2 \right\rangle$. Both the absorption and the reemission part of the scattering process induce momentum diffusion,

$$\left\langle \mathbf{p}^2 \mathcal{L}_{\text{sca}}(\rho) \right\rangle = \hbar \gamma_{\text{sca}} |\alpha|^2 \left\langle 2\mathfrak{Im}\left\{ u^*(\mathbf{r}) \nabla u(\mathbf{r}) \right\} \cdot \mathbf{p} + \hbar |\nabla u(\mathbf{r})|^2 + \hbar k^2 |u(\mathbf{r})|^2 \right\rangle.$$

(2.26)

The total increase of kinetic energy due to absorption, emission and elastic light scattering then becomes

$$\partial_t \langle \mathsf{H}_{\text{PPP}} \rangle = \frac{\hbar (\gamma_{\text{abs}} + \gamma_{\text{sca}}) |\alpha|^2}{2m} \left\langle 2\mathfrak{Im}\left\{ u^*(\mathbf{r}) \nabla u(\mathbf{r}) \right\} \cdot \mathbf{p} + \hbar |\nabla u(\mathbf{r})|^2 \right\rangle$$
$$+ \frac{\hbar^2 k^2 |\alpha|^2}{2m} \gamma_{\text{sca}} \left\langle |u(\mathbf{r})|^2 \right\rangle + \int_0^\infty \frac{d\omega}{2m} \gamma_{\text{emi}}(\omega) \left(\frac{\hbar\omega}{c} \right)^2. \quad (2.27)$$

The emission part can be safely neglected in the presence of strong coherent fields, $|\alpha|^2 \gg 1$, and the scattering part is only relevant if the particle does not absorb considerably at that particular wavelength.

In the course of this work, I will focus on two main types of applications of the developed formalism, corresponding to two distinct interaction regimes between the PPP and the strong coherent light field:

- **Cavity-assisted motion control** The non-conservative nature of the light-matter coupling can be exploited to dissipatively manipulate and slow down the motion of hot and free-flying polarizable particles while they interact with the strong coherent field inside a high-finesse optical cavity. This requires sufficiently long interaction times, as compared to the time scale of the cavity field dynamics. I will present a basic classical assessment of the general effect in the next Sect. 2.1.3, before turning to a more rigorous quantum model in Sect. 2.2, and before I generalize the description to objects beyond the point-particle approximation in Sect. 2.3.
- **Diffraction elements for matter-wave interferometry** Coherent light fields act as beam splitters and optical diffraction elements for matter-waves of polarizable particles in the limit of short interaction times (i.e. passage times through the field mode). Modern-day interference experiments with molecules and clusters [17] rely on the coherent part of the light-matter interaction to create optical gratings for matter-waves, while the non-conservative part of the interaction plays only a minor role in these applications. I will discuss in Sect. 2.1.4 how light fields can coherently modulate the phase or the amplitude of matter-waves of polarizable particles. This effect will be an essential ingredient in the general assessment of matter-wave interferometry in Chap. 3 of this thesis.

2.1.3 Classical Dynamics of a Polarizable Point Particle Coupled to a Strongly Pumped Cavity Mode

Both the conservative and the non-conservative light forces can be employed to dissipate kinetic energy of a PPP when it is coupled to the retarded dynamics of a
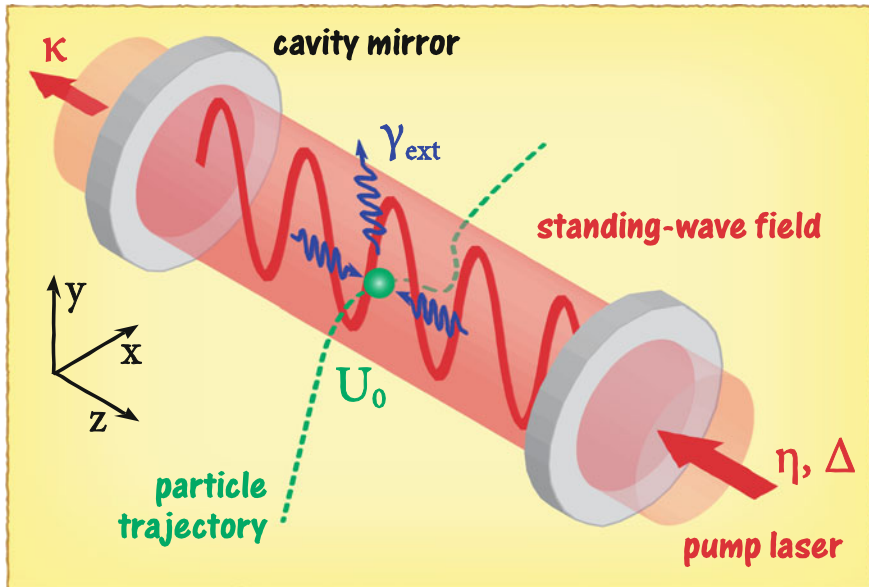
Fig. 2.1 Sketch of the experimental situation when a polarizable point particle (PPP) passes a standing-wave Fabry-Pérot cavity pumped by a strong laser field through one of the cavity mirrors. The steady-state amplitude of the cavity is determined by the pump rate η, the cavity decay rate κ, and the detuning Δ between the cavity resonance and the pump laser frequency. The PPP couples coherently to the intra-cavity field through the single-photon coupling frequency U_0, and it may also scatter or absorb cavity photons at the total extinction rate γ_{ext}

high-finesse optical resonator. Off-resonant cavity-assisted slowing is a well-studied effect [18–20] (so far only observed in experiments with atoms [21–24]), whose potential lies in its applicability to arbitrary polarizable particles without the need to address a distinct internal level structure [1, 25].

To begin with, let me present the cavity-assisted slowing effect by the example of a PPP inside an ideal Fabry-Pérot standing-wave cavity. A sketch of the geometry is given in Fig. 2.1. For the time being, I shall restrict the view to a classical one-dimensional treatment of the particle motion, assuming that it stays far above the quantum limit of motion (where momentum diffusion would have a strong impact) and that we may neglect weak light forces perpendicular to the standing-wave direction due to the finite-size intensity profile $f(x, y)$ of the cavity mode.[7]

2.1.3.1 Intra-Cavity Field Dynamics

The field dynamics is comprised of the pump laser power P_{in} leaking through the mirrors into the Fabry-Pérot resonator and the power loss P_{out} leaking out. In the

---

[7] In this approximation, the intensity profile merely limits the interaction time between the field mode and the PPP traversing the cavity volume.

steady-state situation when no particle is present, the net power flow must cancel, $P_{\text{in}} = P_{\text{out}}$ (assuming other scattering losses at the mirrors are negligible). The description of the field dynamics is based on the simple differential equation

$$\partial_t \alpha(t) = -i\omega_c \alpha(t) + \eta e^{-i\omega_P t} - \kappa \alpha(t). \tag{2.28}$$

It complements the harmonic oscillation of the intra-cavity field amplitude $\alpha(t)$ at its resonance frequency ω_c by the input term $\eta \exp(-i\omega_P t)$ and the output term $-\kappa \alpha(t)$. The former represents the driving of the amplitude by a strong pump laser at frequency ω_P that leaks into the resonator volume at a rate η. The latter represents the loss of field amplitude due to the finite reflectivity of the mirrors. Equation (2.28) describes a harmonically driven damped oscillator, where the steady-state amplitude

$$\alpha_{ss}(t) = \frac{\eta}{\kappa + i\Delta} e^{-i\omega_P t} \tag{2.29}$$

oscillates at the driving frequency ω_P. The steady-state intensity, proportional to $|\alpha_{ss}|^2 = |\eta|^2 / (\kappa^2 + \Delta^2)$, has a Lorentzian shape as a function of the detuning $\Delta = \omega_c - \omega_P$ between cavity resonance and pump frequency, with κ the cavity linewidth. For far detuned driving frequencies, $|\Delta| \gg \kappa$, the cavity volume inside the Fabry-Pérot mirror geometry is impenetrable, and the pump field is totally reflected on the outside. On resonance, $\Delta = 0$, the cavity becomes perfectly transmissive, and the intra-cavity field energy assumes its maximum $E_{\text{f}} = \hbar\omega_P |\eta|^2 / \kappa^2$. The transmitted power is obtained by decomposing the standing-wave field into two running-wave components; only the forward-directed part can be transmitted. This amounts to 50 % of the intra-cavity amplitude, or 25 % of the intra-cavity intensity, which leaks out at the rate κ, or 2κ, respectively. The fully transmitted input power thus reads as $P_{\text{in}} = P_{\text{out}} = 2\kappa E_{\text{f}}/4 = \hbar\omega_P |\eta|^2 / 2\kappa$, which determines the pump rate η up to an arbitrary phase by $|\eta| = \sqrt{2\kappa P_{\text{in}}/\hbar\omega_P}$.

2.1.3.2 Coupled Cavity-Particle Dynamics

Inserting a PPP into the cavity mode volume modifies the steady-state field amplitude by detuning the cavity resonance frequency and by introducing an additional damping channel. The detuning scales with the single-photon coupling frequency U_0 of the particle, and it is accounted for by adding the dipole interaction potential $H_{\text{int}}(\boldsymbol{r})$ from Eq. (2.6) to the field Hamiltonian. The additional damping is given by the combined photon absorption and scattering rate of the particle, $\gamma_{\text{ext}} = \gamma_{\text{abs}} + \gamma_{\text{sca}}$; the field amplitude decays at half this rate. One usually formulates the resulting field evolution equation in a rotating frame, which removes the fast oscillation at the optical pump frequency ω_P from the much slower particle-field dynamics [26],

$$\partial_t \alpha(t) = -(i\Delta + \kappa)\alpha(t) + \eta - \left(iU_0 + \frac{\gamma_{\text{ext}}}{2}\right)\alpha(t)|f(x,y)|^2 \cos^2 kz(t). \tag{2.30}$$
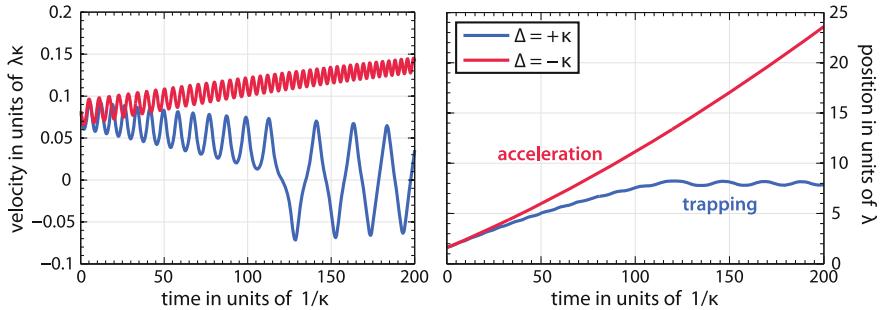
Fig. 2.2 Trajectories of a model particle along the standing wave of a Fabry-Pérot cavity for positive (*blue, bottom curve*) and negative (*red, top curve*) cavity-pump detuning, $\Delta = \pm\kappa$. The *left* and the *right panel* depict the particle's position and velocity, respectively. Natural, cavity-related units are used. The simulation is based on Eqs. (2.30) and (2.31), using the parameters $\eta = 10^3\kappa$, $U_0 = -0.1\kappa$, $\gamma_{\text{ext}} = 0$, $\omega_r = 10^{-6}\kappa$. We assumed an initial velocity of $kv_z = 0.5\kappa$. While the *red* trajectory is constantly accelerated, the *blue* trajectory is slowed until trapping occurs after about 100 cavity lifetimes

The motion of the particle along the cosine pattern of the standing wave is then governed by the z-component of the dipole force (2.5),

$$\partial_t^2 z\,(t) = \frac{2\hbar k}{m} U_0 \,|\alpha\,(t)\,f\,(x,y)|^2 \sin kz\,(t)\cos kz\,(t)$$
$$= \frac{2\omega_r U_0}{k} |\alpha\,(t)\,f\,(x,y)|^2 \sin 2kz\,(t)\,. \tag{2.31}$$

There is no radiation pressure force in the standing-wave case. The two coupled differential equations (2.30) and (2.31) describe the one-dimensional particle-cavity dynamics in the classical limit if transverse light forces are neglected. For a particle traversing the cavity we can introduce a finite time window of the interaction by setting $x = x_0 + v_x t$ and $y = y_0 + v_y t$.

Figure 2.2 depicts two simulated trajectories of a model particle moving along the central z-axis of a pumped standing-wave cavity ($x = y = 0$). The upper (red) and lower (blue) trajectories correspond to a negative and positive detuning Δ between the cavity and the laser, respectively. In both cases we observe a sinusoidal velocity modulation as the particle moves along the periodic optical potential of the standing-wave cavity field. Indeed, if the cavity field α were not modified by the presence of the particle, Eq. (2.31) would describe the oscillatory motion of a mathematical pendulum.

On a time scale larger than the cavity reaction time $1/\kappa$, the trajectories exhibit a gradual decrease (blue, bottom curve) or increase (red, top curve) in velocity, which cannot be explained by the conservative dipole force. In the former case, the particle is eventually trapped in the optical potential, and its total energy becomes negative. Its velocity then oscillates between negative and positive values as it bounces between the walls of the standing-wave potential.

It is the delayed reaction of the cavity to the particle that is responsible for the effective dissipation (or heating) of the kinetic energy. This effect establishes the basis of potential cavity-induced slowing and trapping methods for molecules, clusters and other polarizable objects. In the following I will study this effect in more detail, including also an assessment of its strength and applicability under realistic conditions.

2.1.3.3 Estimated Friction Force

The characteristics of the dissipation effect are best studied in a first order approximation of the delayed reaction of the cavity to the moving particle. For this we expand the field amplitude $\alpha(t) = \alpha_0(t) + \alpha_1(t)$ into the modified steady-state term

$$\alpha_0(t) = \frac{\eta}{\kappa + i\Delta + \left(i\widetilde{U}_0 + \widetilde{\gamma}_{\text{ext}}/2\right)\cos^2 kz(t)} =: \frac{\eta}{\Omega(t)}, \qquad (2.32)$$

which would be the solution if the field adjusted instantaneously to the current position $z(t)$ of the particle, and the term $\alpha_1(t)$ incorporating the corrections due to the finite reaction time scale of the cavity. Here I have absorbed the transverse coordinates into the coupling parameters $\widetilde{U}_0 = U_0|f(x, y)|^2$, $\widetilde{\gamma}_{\text{ext}} = \gamma_{\text{ext}}|f(x, y)|^2$. Neglecting again their time dependence, we find that the correction term evolves according to

$$\partial_t \alpha_1(t) = \eta \frac{\partial_t \Omega(t)}{\Omega^2(t)} - \Omega(t)\alpha_1(t), \qquad (2.33)$$

which can be formally solved by applying the same expansion procedure iteratively, $\alpha_1(t) = \eta \partial_t \Omega/\Omega^3 + \alpha_2(t)$ etc. Let us, however, stop the iteration at the first order correction term, $\alpha_1(t) \approx \eta \partial_t \Omega(t)/\Omega^3(t)$, neglecting all higher-order delayed reaction contributions. This is valid if the particle does not couple too strongly to the cavity and moves slowly along the standing wave profile so that the field amplitude can keep up. In other words, the approximation holds for coupling frequencies U_0 and Doppler frequencies kv smaller than the parameters κ and Δ which determine the reaction time scale of the cavity. The approximate field amplitude now also depends on the velocity $v(t) = \partial_t z(t)$ of the particle,

$$\alpha(t) \approx \frac{\eta}{\Omega(t)} \left[1 - \frac{kv(t)}{\Omega^2(t)} \left(i\widetilde{U}_0 + \frac{\widetilde{\gamma}_{\text{ext}}}{2}\right) \sin 2kz(t)\right], \qquad (2.34)$$

which results in a velocity-dependent force when inserted into the equation of motion (2.31). Looking only at the friction force term that is linear in velocity, $F_v = m\beta v$, we find as the approximate friction coefficient

$$\beta = -\omega_r \left|\frac{\eta}{\Omega^3}\right|^2 \sin^2 2kz \left[8\kappa \Delta \widetilde{U}_0^2 + 2\left(\kappa^2 - \Delta^2\right) \widetilde{U}_0 \widetilde{\gamma}_{\text{ext}}\right.$$
$$\left. +2\kappa \widetilde{U}_0 \left(\widetilde{\gamma}_{\text{ext}}^2 + 4\widetilde{U}_0^2\right) \cos^2 kz + \widetilde{U}_0 \widetilde{\gamma}_{\text{ext}} \left(\widetilde{\gamma}_{\text{ext}}^2 + 2\widetilde{U}_0^2\right) \cos^4 kz\right]. \quad (2.35)$$

Only the first two terms in the square brackets can change their sign by varying the detuning Δ. Given that most polarizable particles in question are high-field seeking, $U_0 < 0$, and that γ_{ext} is small, we observe that a negative friction coefficient β is obtained for positive detuning $\Delta > 0$. That is to say, dissipative slowing requires the pump laser to be red-detuned with respect to the cavity resonance, whereas a blue-detuned laser will always lead to the opposite effect.

The basic physical picture underlying the slowing effect is sketched in Fig. 2.3. Suppose the pump laser is red-detuned to the steep flank of the Lorentzian cavity resonance line, $\Delta \sim \kappa$, and the particle moves towards the antinode of the intra-cavity standing-wave field. As it enters the high-insensity region its potential energy decreases immediately, and it speeds up until it reaches the potential minimum at the antinode. At the same time, the particle shifts the cavity resonance towards the laser frequency, thereby effectively decreasing the detuning Δ and increasing the field intensity. This leads to a slightly delayed lowering of the optical potential 'valley', while the particle is already moving out of the minimum and up the potential 'hill', which is now higher than it was when the particle came in. Hence, if the cavity delay matches the particle's velocity, $kv < \kappa$, the latter must on average climb up more than it falls down, gradually losing kinetic energy.

Are the simulated results comparable to a realistic scenario? I list the light coupling parameters of different polarizable particles in Table 2.1. The selection covers a mass range of 9 orders of magnitude between a single lithium atom and a gold nanosphere. The coupling parameters are evaluated for a standing-wave cavity operating at the IR wavelength $\lambda = 1.56\,\mu\text{m}$ with $\kappa = 1\,\text{MHz}$ linewidth, which is pumped at the detuning $\Delta = -\kappa$ by a laser of $P_{\text{in}} = 1\,\text{W}$ continuous-wave power. These rather demanding parameters should be feasible using a resonator geometry with 25 mm curved mirrors that are positioned at $L = 1\,\text{mm}$ distance [27].[8] By pumping a Gaussian TEM_{00} mode with a waist of $w = 40\,\mu\text{m}$ it should be possible to achieve a mode volume as small as $V = \pi L w^2/4 = 0.0013\,\text{mm}^3$, which trumps our earlier estimates for the light-matter coupling parameters in [1] by orders of magnitude. This leads to considerable friction rates $|\overline{\beta}|$, as given by the position-averaged expression (2.35). The latter predicts an average dissipation of the z-velocity on a time scale $\sim 1/|\overline{\beta}|$. Within the boundaries of the above model, the obtained values that can be as small as a few nanoseconds for the heaviest nanoparticles in the table. Being 100 nm large in diameter, these are at the top end of the point particle regime; the

---

[8] A cavity linewidth of 1 MHz corresponds to a so-called cavity finesse parameter $F = \pi c/2\kappa L \approx 5 \times 10^{-5}$. The latter is related to the reflectivity R of both mirrors via the relation $F = \pi \sqrt{R}/(1-R)$ in the absence of additional losses in the resonator [28]. The suggested cavity setup requires $1 - R \approx 7 \times 10^{-6}$.
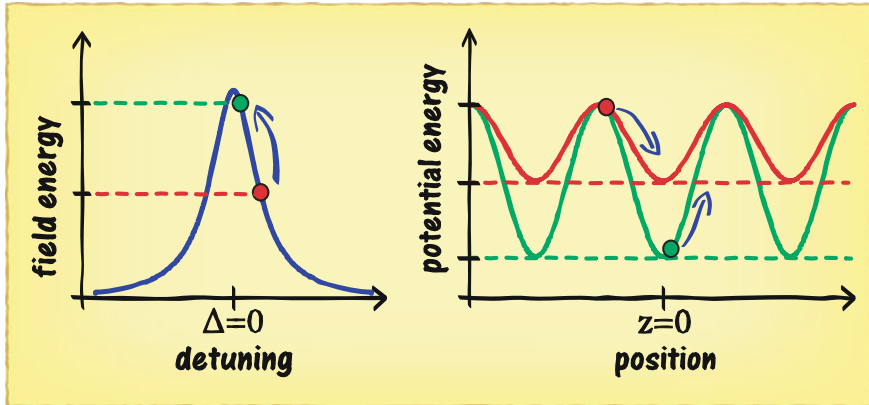
Fig. 2.3 Schematic energy diagram of Fabry-Pérot cavity and particle for two different particle positions (*red* and *green circles*). The initial detuning of the pump laser to the red side flank of the cavity resonance line ($\Delta = \omega_c - \omega_P > 0$) facilitates a dissipative slowing effect. A high-field seeking particle moving from a node (*red circle*) to an antinode (*green circle*) of the standing wave is accelerated due to the change in optical potential. In addition, it tunes the cavity resonance closer to the pump frequency, thereby lowering its own optical potential. As the latter effect lags behind due to the finite reaction time of the cavity, the particle must climb up a steeper potential hill, and gradually loses kinetic energy, when moving towards the next field node

description of larger objects will be discussed in Sect. 2.3. Moreover, a more rigorous quantum treatment of the dissipative slowing effect in the limit of weakly coupling point particles will be discussed in detail in Sect. 2.2.

2.1.4 Optical Gratings for Matter-Waves

Having discussed the classical long-time dynamics of a PPP in the presence of a (classical) strong cavity field I now turn to quite the opposite regime: The short-time effect of strong coherent fields on the propagation of PPP matter-waves. Rather than trying to explicitly solve the time evolution in the presence of the field, I am going to adhere to the scattering picture and implement the short presence of the field as a scattering *event* that transforms an incoming matter-wave state ρ to an outgoing, scattered state $\rho' = \mathcal{S}(\rho)$.

The coherent standing-wave (or running-wave) light field in question shall be generated by a strong laser that is (or is not) retroreflected off a mirror (rather than by a driven high-finesse resonator mode, as in the previous section). The laser may either be shortly pulsed [9] or continuous, in which case we shall assume the particle to be fast in traversing the light mode. This regime provides the means to employ light

---

[9] Since the wavelength of the laser is required to be sufficiently well defined for the present purposes, ultrashort pulses with a broad frequency spectrum are excluded here.

Table 2.1 Coupling parameters between the standing-wave field of an IR high-finesse cavity ($\lambda = 1.56\,\mu m$, $\kappa = 1\,MHz$, $V = 0.0013\,mm^3$) to various polarizable (high-field seeking) particles ranging from a single lithium atom to nanospheres of 50 nm radius

Particle	m (amu)	ω_r (Hz)	$|U_0|$ (Hz)	γ_{abs} (Hz)	γ_{sca} (Hz)	$|\overline{\beta}|$ (Hz)
Li	7	7.4×10^4	0.14	–	3.0×10^{-10}	1.2×10^4
C_{60}	720	715	0.50	2.4×10^{-4}	3.6×10^{-9}	1.4×10^3
He_{1000}	4,000	129	1.2	–	2.1×10^{-8}	1.5×10^3
Li_{1000}	7,000	74	33	0.59	1.6×10^{-5}	6.4×10^5
$(SiO_2)_{1000}$	60,000	8.6	18	1.4×10^{-10}	4.4×10^{-6}	2.1×10^4
Au_{1000}	197,000	2.6	25	0.19	9.2×10^{-6}	1.3×10^4
SiO_2 sphere	6.9×10^8	7.4×10^{-4}	2.0×10^5	1.6×10^{-6}	592	2.9×10^8
Si sphere	7.3×10^8	7.1×10^{-4}	5.9×10^5	–	5.1×10^3	3.2×10^9
Au sphere	6.1×10^9	8.5×10^{-5}	7.8×10^5	5.8×10^3	8.8×10^3	6.9×10^8

The dielectric functions of bulk lithium ($\varepsilon = -50.41 + 7.55i$), gold ($\varepsilon = -91.49 + 10.35i$), silicon ($\varepsilon = 12.05$) and silica ($\varepsilon = 2.1 + 6 \times 10^{-12}i$) are used to estimate the cluster parameters [29, 30]. Their polarizabilities are given by the standard formula [31], $\chi = 4\pi\varepsilon_0 R^3 (\varepsilon - 1) / (\varepsilon + 2)$, with $R = \sqrt[3]{3m/4\pi\varrho}$ the sphere radius and ϱ the bulk mass density. The polarizability of C_{60} is taken from [32], and the static value per atom is used for the Li atom and the He droplet [33, 34]. We neglect the absorption of the IR-transparent particles. The position-averaged friction coefficient $\overline{\beta}$ is evaluated at the cavity-laser detuning $\Delta = \kappa$

fields as diffractive elements in matter-wave interferometry, as will be discussed in the following with a focus on the Viennese near-field interference experiments with molecules and clusters [17].

2.1.4.1 Coherent Grating Interaction

In the absence of photon absorption and Rayleigh scattering the interaction between the laser field and the particle is entirely coherent. That is to say, the impact of the short field presence on the quantum state of motion can be described by a unitary scattering transformation $\mathcal{S}(\rho) = \mathsf{S}\rho\mathsf{S}^\dagger$, $\mathsf{S}^\dagger\mathsf{S} = \mathbb{I}$. An explicit form is obtained in the basis of plane wave states by the renowned eikonal approximation [35–37],

$$\langle r|p\rangle \mapsto \langle r|\mathsf{S}|p\rangle = \exp\left[-\frac{i}{\hbar}\int_{-\infty}^{\infty} dt\, H_{int}\left(r + \frac{pt}{m}\right)\right]\langle r|p\rangle, \qquad (2.36)$$

with $H_{int}(r) = -\mathfrak{Re}\{\chi\}|E(r)|^2/4$ the optical dipole potential of the particle in the field. The approximation holds in a semiclassical high-energy limit where the classical action associated to the motion of the particle over the course of the short interaction time exceeds by far the eikonal action integral over the optical potential in (2.36) [37]. The transformation describes a coherent phase modulation of incoming matter-waves. In the case of a standing-wave field, $E(r) = E_0\epsilon f(x, y)\cos kz$, it constitutes a one-dimensional periodic phase grating.

In practice, one can employ an even simpler form of the transformation that acts only on the reduced one-dimensional state of motion along the z-axis, thus omitting the generally weak modulation effect in the x- and y-direction due to the transverse mode profile $f(x, y)$. Moreover, if the velocities v_z constituting the state of motion of the particle are sufficiently small,[10] we may take the position distribution on the z-axis to be at rest during interaction time. We arrive at the transformation rule

$$\langle z|\psi\rangle \mapsto \exp\left(i\phi_0 \cos^2 kz\right) \langle z|\psi\rangle \tag{2.37}$$

for any state vector $|\psi\rangle$ for the one-dimensional z-motion of the particle that complies with the above constraints. This *longitudinal eikonal approximation* is commonly used to describe thin optical transmission gratings in matter-wave interferometry [38–40], and it will be presumed throughout the remainder of the manuscript. I refer the reader to [36, 37] for an exhaustive study of semiclassical corrections to the eikonal approximation. The eikonal phase factor ϕ_0 is obtained by integrating the interaction potential over the intensity profile of the laser. We distinguish two implementations regarding the interferometry of large molecules and clusters:

- **Kapitza-Dirac Talbot-Lau interferometer (KDTLI)** The KDTLI setup is a three-grating near-field interferometer where the interference effect is related to the periodic phase modulation at the central grating, a standing laser wave [40]. A collimated beam of fast molecules traverses the three-grating geometry along the x-axis, and it is aligned in such a way that it crosses the laser grating centrally and (almost) perpendicular to the standing-wave z-axis.[11] This is made possible by using a cylindrical lens system to narrow the laser spot (down to a few tens of microns) in the direction of flight x, while keeping a large waist (of roughly one millimeter) along y. We may thus assume that the collimated molecule beam passes the laser grating in the xz-plane, setting $y \approx 0$. The phase factor (2.37) then reads as

$$\phi_0 = \frac{\mathfrak{Re}\{\chi\}|E_0|^2}{4\hbar} \int_{-\infty}^{\infty} \frac{\mathrm{d}x}{v} f^2(x, 0), \tag{2.38}$$

---

[10] To be more concrete, the travelled distance $v_z\tau$ during the interaction period τ between the particle and the field must be small compared to the laser wavelength, $|v_z\tau| \ll \lambda$. Given the reduced one-dimensional quantum state of motion ρ_z, the condition should cover its entire velocity distribution $\langle mv_z|\rho|mv_z\rangle$.

[11] Note that the direction of the grating is commonly referred to as the x-axis in the interferometry literature, whereas the standing wave is directed along z in the present notation, which is conventionally used in the description of light scattering at spherical particles. I will resort to the x-notation in Chap. 3.

assuming a fixed longitudinal velocity v of the molecules.[12] Assuming a Gaussian intensity profile $f(x, y) = \exp\left(-x^2/w_x^2 - y^2/w_y^2\right)$ with waist parameters $w_{x,y}$ and an input laser power P_L, we find [40]

$$\phi_0 = \frac{4\sqrt{2\pi}\,\mathfrak{Re}\,\{\chi\}\,P_L}{hc\varepsilon_0 v w_y}. \tag{2.39}$$

Given molecular velocities of the order of 100 m/s and an x-waist of $w_x = 20\,\mu\text{m}$ each molecule spends less than a microsecond in the laser grating. It can travel not more than 100 nm along the grating axis during that period, as the molecule beam is typically collimated to a few milliradians opening angle. Hence, the longitudinal eikonal approximation is well justified.

- **Optical time-domain ionizing Talbot-Lau interferometer (OTITLI)** The OTITLI[13] is a Talbot-Lau setup in the time domain where the gratings are generated by three short laser pulses, which are retroreflected off a mirror [41]. A small cloud of nanoparticles flying alongside the mirror surface illuminated this way may be ionized in the antinodes of the pulses; they play the role of the thin transmission gratings of a regular Talbot-Lau setup. The phase modulation in each pulse is given by

$$\phi_0 = \frac{4\pi\,\mathfrak{Re}\,\{\chi\}\,E_L}{hc\varepsilon_0 a_L} \tag{2.40}$$

if we assume that the particle ensemble is always well localized in the center of focus, $f(x, y) \approx f(0, 0) = 1$, when illuminated by grating laser pulses of sufficiently large spot size $a_L = \int \mathrm{d}x\mathrm{d}y\, f^2(x, y)$ (or a flat-top shaped spot profile). The pulse energy $E_L = \int_\tau \mathrm{d}t\, P_L(t)$ is obtained by integrating the laser power over the temporal pulse shape of length τ. Again, the eikonal expression (2.37) is only valid if the particles are approximately at rest over the pulse duration τ. The present experimental realization of the OTITLI setup in the Vienna group operates with vacuum-ultraviolet (VUV) laser pulses of $\tau \lesssim 10$ ns at a wavelength of $\lambda = 157$ nm. The particle velocities therefore must be restricted to below 10 m/s in z-direction by means of collimation, for instance.

The general working principle of Talbot-Lau interferometry will be discussed in detail in Chap. 3. There I will show how the periodic phase modulation at a standing-wave grating leads to matter-wave interferograms. A full assessment of thin optical gratings, however, must also account for non-conservative effects, most prominently, photon absorption.

---

[12] A realistic description of the molecular beam state involves a broad distribution of velocities v, and the resulting ϕ_0-dependent interferogram must be averaged accordingly.

[13] Also referred to as OTIMA: optical time-domain ionizing matter-wave interferometer.

2.1.4.2 Amplitude Modulation by Means of Optical Depletion Gratings

The absorption of light from an optical standing-wave grating does not necessarily imply the loss of matter-wave coherence. The latter can be avoided (or suppressed) if the absorption of one or more photons removes the particle from the interfering ensemble present in the experiment. Depending on the internal properties of the particles and the selectivity of the detection scheme with respect to these properties, the removal can in principle be achieved by the ionization, fragmentation, isomerization, excitation, or simply internal heating, that may be triggered by the deposited photon energy. Consequently, the particle ensemble is depleted in the antinodes, whereas nothing happens in the nodes of the standing-wave grating. The resulting periodic modulation of the matter-wave amplitude renders the standing laser wave an optical generalization of a material diffraction mask, with the nodes representing the apertures and the antinodes representing (semi-transmissive) walls of the grating.

Optical depletion gratings of this kind have been used in atom interferometry [42], where the absorption of a single photon induces an internal state transition and the atoms are post-selected according to their energy level in the detector. The experimentalists working on the OTITLI setup in the Vienna lab make use of photon-induced ionization to generate depletion gratings from VUV laser pulses,[14] as the energy of a single UV photon exceeds the ionization threshold of most molecular and atomic cluster particles.

Let me now describe the action of an optical depletion grating on the matter-waves interacting with the standing-wave field, in analogy to material diffraction masks. An ideally thin one-dimensional diffraction grating, where the slits are periodically arranged along the z-axis, is described by a periodic aperture function $P(z)$, which can only take the values zero (wall) or one (opening). Given an incoming matter-wave state $\psi(z) = \langle z | \psi \rangle$ we find the density distribution of particles behind the grating to be $P(z) |\psi(z)|^2$. That is to say, the grating transformation modulates the matter-wave state by the square root of the transmission probability, $\psi(z) \mapsto \sqrt{P(z)} \psi(z)$, up to a prefactor that accounts for the renormalization of the state vector.

In the case of a thin optical depletion grating, the transmission probability $P(z)$ may take any value between zero and one, depending on the local standing-wave intensity (with $P(z) = 1$ at the nodes of the standing wave). Including also the phase modulation effect (2.37) due to the dipole interaction, as discussed in the preceding section, we can introduce a complex transmission function $t(z)$ to describe the full modulation of the matter-wave state,

$$\langle z | \psi \rangle \mapsto \sqrt{P(z)} \exp\left(i\phi_0 \cos^2 kz\right) \langle z | \psi \rangle =: t(z) \langle z | \psi \rangle. \qquad (2.41)$$

The density operator ρ transforms as $\rho \mapsto t(\mathbf{z}) \rho t^*(\mathbf{z})$. Using a Poissonian model for the photon absorption, as discussed in Sect. 2.1.2, and following the same arguments as for the phase modulation, we can express the transmission probability in

---

[14] The ionized particles are in practice removed from the ensemble with the help of a constant electric field applied to the interferometer setup.

terms of the mean number of absorbed photons, $\bar{n}(z) = n_0 \cos^2 kz$. In the case of fast particles crossing a stationary thin laser beam of power P_L, the value n_0 at the antinodes reads as

$$n_0 = \frac{8\sigma_{abs} P_L \lambda}{\sqrt{2\pi} hcv w_y},$$
(2.42)

and in the case of illumination by a short laser pulse of energy E_L as

$$n_0 = \frac{4\sigma_{abs} E_L \lambda}{hca_L}.$$
(2.43)

When a single absorbed photon suffices to remove a particle from the ensemble (e.g. by ionization) the transmission probability can be written as the Poisson probability $p_0(z)$ of zero absorption, $P(z) = p_0(z) = \exp[-\bar{n}(z)]$, and the transmission function becomes

$$t(z) = \exp\left[\left(-\frac{n_0}{2} + i\phi_0\right)\cos^2 kz\right].$$
(2.44)

In the inverted situation, where it is the non-absorbing particles that are removed from the ensemble, we arrive at

$$t_{inv}(z) = \sqrt{1 - \exp\left(-n_0 \cos^2 kz\right)} \exp\left(i\phi_0 \cos^2 kz\right).$$
(2.45)

More generally, one could also conceive situations where the depletion threshold is reached by absorbing N or more independent photons, in which case the transmission function reads as

$$t_N(z) = \sqrt{\sum_{n=0}^{N-1} \frac{1}{n!}\left(n_0 \cos^2 kz\right)^n \exp\left[\left(-\frac{n_0}{2} + i\phi_0\right)\cos^2 kz\right]}.$$
(2.46)

Here one must be careful with using the simple Poissonian model of absorption. The latter is only meaningful when subsequent absorption events can be regarded as statistically independent, and it ceases to be valid when the internal state and the absorption cross-section σ_{abs} of the particle are noticeably modified by each absorption. Moreover, one must also take into account the photon momenta transferred to all those particles that did not absorb enough photons to be removed.

2.1.4.3 Momentum Transfer by Absorption and Scattering

Any full description of optical elements, which are not based on single-photon depletion, must include the momentum transfer due to the possible absorption and Rayleigh scattering of laser photons. This generally comes with the loss of matter-wave coherence, an unwanted side-effect in optical gratings. For instance, it would be inexpedient to try interfering strongly absorptive molecules in a KDTLI setup, where the

purpose of the laser grating is to modulate coherently the phase of the matter-waves. On the other hand, for most polarizable subwavelength particles the inevitable coherence loss due to Rayleigh scattering is usually a negligible effect in the short-time interaction regime relevant for interferometry at optical gratings.

Absorption

I presented a model of the absorption-induced momentum transfer in Sect. 2.1.2.1. In accordance with the longitudinal eikonal approximation for the coherent grating transformation, let me omit any action of the Lindblad term (2.16) on the transverse motion in the field mode. This results in the effective one-dimensional transformation

$$\mathcal{L}_{\mathrm{abs}}\left(\rho\right) = \Gamma_{\mathrm{abs}}\left(t\right)\left[\cos\left(kz\right)\rho\cos\left(kz\right) - \frac{1}{2}\left\{\cos^2\left(kz\right),\rho\right\}\right] \qquad (2.47)$$

of the quantum state ρ of motion along the standing-wave axis z. The time-dependent rate term relates to the mean number of absorbed photons $n_0 = \int \mathrm{d}t\,\Gamma_{\mathrm{abs}}\left(t\right)$ through an integration over the transverse laser beam profile in a co-moving frame along the particle trajectory, Eq. (2.42), or over the temporal shape of the laser pulse, Eq. (2.43). The above part of the master equation can be explicitly integrated in the position representation $\langle z|\rho|z'\rangle$, which amounts again to omitting motion during the interaction time,

$$\langle z|e^{\mathcal{L}_{\mathrm{abs}}t}\rho|z'\rangle = \exp\left[-n_0\left(\frac{\cos^2 kz}{2} + \frac{\cos^2 kz'}{2} - \cos kz\,\cos kz'\right)\right]\langle z|\rho|z'\rangle$$

$$= \underbrace{\exp\left[-2n_0\sin^2\left(k\frac{z+z'}{2}\right)\sin^2\left(k\frac{z-z'}{2}\right)\right]}_{=:\mathcal{R}_{\mathrm{abs}}(z,z')}\langle z|\rho|z'\rangle. \qquad (2.48)$$

The decohering effect is evident: All nondiagonal matrix elements are damped except for $z - z' = n\lambda$, the strongest effect occuring between nodes and antinodes.[15]

In the position representation the transformation simply reduces to a multiplication of the density matrix by the positive decoherence function $0 < \mathcal{R}_{\mathrm{abs}}\left(z,z'\right) \leq 1$. Recalling that the coherent grating transformation also contributes a mere multiplication by $t\left(z\right)t^*\left(z'\right)$ in this representation, we are allowed to combine both factors to obtain the overall grating transformation $\langle z|\rho|z'\rangle \mapsto t\left(z\right)t^*\left(z'\right)\mathcal{R}_{\mathrm{abs}}\left(z,z'\right)\langle z|\rho|z'\rangle$.

Scattering

The Rayleigh scattering of photons into free-space discussed in Sect. 2.1.2.3, no matter how weak in practice, can be incorporated in the same manner. Tracing out the transverse part of the motion, the reduced one-dimensional version of the scattering Lindblad term (2.24) reads as

---

[15] This is intuitively clear since the absorption of a photon reveals the information that the particle is not located at a node. On the other hand, the photon cannot distinguish two positions z and z', which differ by an integer multiple of the wavelength.

$$\mathcal{L}_{\text{sca}}(\rho) = \Gamma_{\text{sca}}(t) \left[\int d^2n \, R(\mathbf{n}) \cos(k\mathbf{z}) \, e^{-ikn_z\mathbf{z}} \rho \cos(k\mathbf{z}) \, e^{ikn_z\mathbf{z}} - \frac{1}{2} \left\{ \cos^2(k\mathbf{z}), \rho \right\} \right]$$

$$= \Gamma_{\text{sca}}(t) \left[\int d\Omega \, \frac{3\sin^2\theta}{8\pi} \cos(k\mathbf{z}) \, e^{-ik\sin\theta\sin\varphi\mathbf{z}} \rho \cos(k\mathbf{z}) \, e^{ik\sin\theta\sin\varphi\mathbf{z}} \right.$$

$$\left. - \frac{1}{2} \left\{ \cos^2(k\mathbf{z}), \rho \right\} \right]. \tag{2.49}$$

Note that the solid angle integration over the dipole radiation pattern $R(\mathbf{n}) = 3\sin^2\theta/8\pi$ must be performed on a sphere with its poles oriented along the polarization $\boldsymbol{\epsilon}$ of the electric light field, which is perpendicular to the z-axis. The explicit expression for the decoherence function becomes,[16]

$$\ln\left[\mathcal{R}_{\text{sca}}(z, z')\right] + n_{\text{sca}} \frac{\cos^2 kz + \cos^2 kz'}{2}$$

$$= n_{\text{sca}} \frac{3\cos kz \, \cos kz'}{8\pi} \int d\Omega \, \sin^2\theta e^{ik(z'-z)\sin\theta\sin\varphi}$$

$$= n_{\text{sca}} \frac{3\cos kz \, \cos kz'}{2} \int_0^{\pi/2} \sin^3\theta d\theta \, J_0\left(k(z'-z)\sin\theta\right)$$

$$= 3n_{\text{sca}} \cos kz \, \cos kz' \frac{\sin k(z'-z) - j_1\left(k(z'-z)\right)}{2k(z'-z)}. \tag{2.50}$$

Here, n_{sca} gives the mean number of scattered photons in the antinodes. It is obtained from the expressions (2.42) and (2.43) by replacing the absorption cross section with σ_{sca}.

A slightly different and somewhat simpler result would be obtained if the particle scattered the light isotropically, a frequently used simplification,

$$\mathcal{R}_{\text{sca,iso}}(z, z') = \exp\left\{ -n_{\text{sca}} \left[\frac{\cos^2 kz + \cos^2 kz'}{2} - \cos kz \, \cos kz' \, \text{sinc} \, k(z'-z) \right] \right\}. \tag{2.51}$$

In most cases relevant for interferometry, however, the mean number of scattered photons is negligibly small, $n_{\text{sca}} \ll 1$, and one may omit the Rayleigh scattering effect alltogether.

---

[16] I made use of the integral representation of the Bessel function $\int_0^{2\pi} d\varphi \, \exp(i\xi\sin\varphi) = 2\pi J_0(\xi)$, as well as of the integral identity [43]

$$\int_0^{\pi/2} d\theta \, J_0(\beta\sin\theta) \sin\theta \cos^{2r+1}\theta = 2^r \beta^{-1-r} \Gamma(r+1) J_{r+1}(\beta),$$

with $r = \pm 1/2$ and the Gamma function $\Gamma(3/2) = \sqrt{\pi}/2 = \frac{1}{2}\Gamma(1/2)$. The identity leads naturally to spherical Bessel function expressions $j_n(\beta) = \sqrt{\pi/2\beta} J_{n+1/2}(\beta)$, where $j_0(\beta) = \text{sinc}\beta$.

Taking both the absorption and the scattering effect into account, the overall matter-wave state transformation at an optical standing-wave grating becomes

$$\langle z|\rho|z'\rangle \mapsto t\,(z)\,t^{*}\,(z)\,\mathcal{R}_{\mathrm{abs}}\,(z, z')\,\mathcal{R}_{\mathrm{sca}}\,(z, z')\,\langle z|\rho|z'\rangle. \qquad (2.52)$$

We note that the present absorption and scattering transformations are based on an elementary Markovian model where the laser mode is linearly coupled to an initially cold reservoir of free-space vauum modes (in case of scattering) and of internal degrees of freedom of the particle (in case of absorption). In particular, the model accounts for the correct momentum state of a standing-wave photon, a *superposition* of two counter propagating plane waves, which is coherently transferred to the particle upon absorption. This improves the probabilistic argument presented in [40], where the absorption of standing-wave photons is implemented as a purely classical binary random walk with 50 % chance to be kicked by $+\hbar k$ or $-\hbar k$.

This classical model is indistinguishable from the present treatment in the case of photon absorption from a running-wave field, say, directed into the positive z-direction. The corresponding Lindblad term is then of random unitary type, $\mathcal{L}_{\mathrm{abs}}\,(\rho) = \Gamma_{\mathrm{abs}}\left[\exp\left(ik\mathsf{z}\right)\rho\exp\left(-ik\mathsf{z}\right) - \rho\right]$, and the quantum state of motion transforms as

$$\langle z|\rho|z'\rangle \mapsto \exp\left\{-n_0\left[1 - e^{ik(z-z')}\right]\right\}\langle z|\rho|z'\rangle = e^{-n_0}\sum_{n=0}^{\infty}\frac{n_0^n}{n!}\langle z|e^{inkz}\rho e^{-inkz'}|z'\rangle$$

$$\equiv \langle z|\sum_{n=0}^{\infty}p_n\mathsf{U}_n\rho\mathsf{U}_n^{\dagger}|z'\rangle. \qquad (2.53)$$

This expression is a probabilistic sum of unitary momentum kick transformations $\mathsf{U}_n = \exp\left(ink\mathsf{z}\right)$, which also follows from a classical Poissonian ansatz.

2.2 Quantum Mechanics of Polarizable Point Particles in High-Finesse Cavities

The preceding study of polarizable point particles interacting with coherent light fields has lead to a first assessment of cavity-induced slowing in Sect. 2.1.3, where both the PPP motion and the field were treated classically, and to the description of optical diffraction gratings of PPP matter-waves in Sect. 2.1.4, where the strong coherent field remained a classical degree of freedom.

Let me now proceed with a full quantum treatment of both the light and the particle, a necessary prerequisite to assess the diffusive and dissipative effects arising from the coupling between a PPP and one or more driven or empty high-finesse cavity modes. A rigorous derivation of the friction and diffusion parameters in the presence of one strongly driven *pump mode* will be given in the weak-coupling limit where

the particle-induced field fluctuations are small. This assumption of weak coupling holds true for many subwavelength molecules and clusters, which do not exhibit a distinct internal resonance that could be addressed by the cavity light. Table 2.1 lists several examples where the rate U_0 defined in Eq. (2.10), at which the particle may induce field shifts, is by orders of magnitude smaller than realistic decay rates $\kappa \sim 1\,\text{MHz}$ of optical high-finesse cavities.

This does not mean, however, that it is a lost cause to study the dynamics of weakly coupling particles in a cavity. I will show how a large coherent driving field can effectively enhance the coupling to the empty cavity modes by orders of magnitude. The weak coupling model, as presented in the following, will then admit a systematic assessment of the main dissipative effects of the enhanced coupling. In particular, we will find that the cavity-induced friction force increases with each empty cavity mode that is accessible for the pump light—a potential application for confocal resonator geometries with a large spectrum of degenerate modes. The presented results have been published in [1].

2.2.1 Quantum Model of a PPP Coupled to Multiple Cavity Modes

I start by quantizing the light-matter interaction model of Sect. 2.1 for the generic configuration of one particle in the presence of M empty cavity modes and one strongly driven pump mode, which provides the necessary field input to enhance the coupling of the PPP with the cavity. In practice, one of the cavity modes can play the role of the pump mode when driven by a strong mode-matched laser. An alternative two-dimensional implementation is sketched in Fig. 2.4, where the pump field is generated in a different (free laser or driven cavity) mode oriented perpendicularly to the empty cavity axis. This configuration may be favourable in practice, as it avoids a strong dipole force along the cavity axis as well as the need for selective single-mode driving of a (possibly degenerate) multimode cavity.

The described configuration is characterized by the following parameters:

- The driving field is described by the steady-state pump amplitude α (in the absence of the particle) and by the pump frequency ω_P. The latter serves as the fast reference frequency, and I will switch to the corresponding rotating frame to describe the field dynamics of all other modes.
- The behaviour of each field mode (including the pump) is determined by its detuning $\Delta_n = \omega_n - \omega_P$ with respect to the pump frequency, its decay rate κ_n, its mode function $u_n(\mathbf{r})$, and its mode volume $V_n = \int \mathrm{d}^3 r \, |u(\mathbf{r})|^2$, where $n = 0, 1, \ldots, M$, and $n = 0$ is representing the pump mode. The field polarization vectors are omitted by assuming the same polarization throughout.[17]

---

[17] The coupling strength between fields of different polarizations through a PPP may vary, most notably if the particle is described by a tensorial polarizability. I omit this additional modulation of the coupling for simplicity.
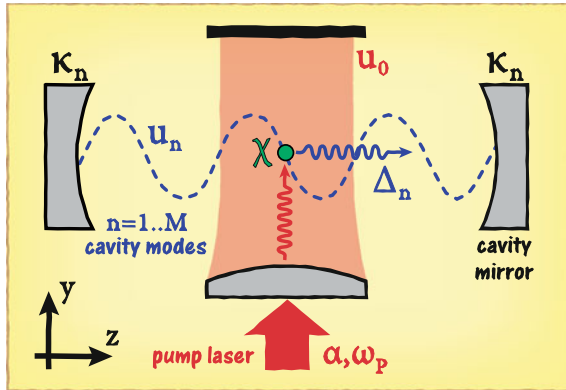
Fig. 2.4 Sketch of an exemplary two-dimensional mode configuration with a strongly driven field mode u_0 directed along the y-axis and a multitude of M empty standing-wave cavity modes u_n along the z-axis (adapted from [1]). In the overlapping region, a particle of polarizability χ redistributes photons between the modes thereby inducing dissipation. Each mode is damped by the rate κ_n and detuned by Δ_n with respect to the driving field. The latter generates a steady-state amplitude α in the absence of the particle

- The particle of mass m_P is described by a scalar polarizability χ, which leads to the effective coupling frequencies $U_{mn} = -\sqrt{\omega_n \omega_m / V_n V_m}\,\mathfrak{Re}\,\{\chi\}\,/2\varepsilon_0$ between the nth and the mth mode.

2.2.1.1 Quantum Description of a Driven Cavity Mode

Before introducing the coupling to the particle, I first translate the classical description of a driven high-finesse cavity mode in Sect. 2.1.3.1 into the quantum picture. Here I make use of the canonical field quantization procedure [44–46] and replace the coherent field amplitude and its complex conjugate by the annihilation and creation operators in the expressions for the physical fields,

$$E\,(r, t) \mapsto \sqrt{\frac{2\hbar\omega_0}{\varepsilon_0 V_0}}\mathsf{a}_0\boldsymbol{\epsilon} u_0\,(\mathbf{r})\,, \qquad H\,(r, t) \mapsto -ic\sqrt{\frac{2\hbar}{\mu_0\omega_0 V_0}}\mathsf{a}_0\nabla \times \boldsymbol{\epsilon} u_0\,(\mathbf{r})\,. \tag{2.54}$$

This results in the free field Hamiltonian $\mathsf{H}_0 = \hbar\omega_0\left(\mathsf{a}_0^\dagger\mathsf{a}_0 + 1/2\right)$, where the constant term is dropped for convenience. In order to describe a driven cavity mode one must include the driving field leaking into the cavity and the losses leaking out. Both effects are covered by a linear coupling model, where the exchange of field amplitude with an external mode b is described by a coupling Hamiltonian of the

form[18] $\propto a_0 b^\dagger + h.c.$ That is, the coupling of the modes can be understood as an exchange of single photons between the field states.

Based on this physical picture we may pin down the loss and driving terms heuristically. The cavity field loss can be seen as a random and uncontrolled elimination of photons as they escape through the cavity mirrors or by scattering into free space at a total rate $2\kappa_0$. In mathematical terms, this is well modelled by a Poisson jump process of the same type as in (2.13), with the jump operator given by the photon annihilator a_0, $\mathcal{L}_{\text{loss}}(\rho) = \kappa_0 \left(2a_0 \rho a_0^\dagger - \left\{ a_0^\dagger a_0, \rho \right\} \right)$.

The same linear description can be applied to the driving by the mode b of a strong laser illuminating the cavity mirror. The quantum representation of a strong coherent laser field is given in terms of coherent states [45]

$$|\beta\rangle = D(\beta)|0\rangle = e^{-|\beta|^2/2} \sum_{n=0}^{\infty} \frac{\beta^n}{\sqrt{n!}} |n\rangle = \exp\left(\beta b^\dagger - \beta^* b \right) |0\rangle, \qquad (2.55)$$

with β the complex field amplitude and $|\beta|^2$ the mean photon number. Coherent states are defined as displaced vacuum states, and they are the eigenvectors of the annihilation operator, $b|\beta\rangle = \beta|\beta\rangle$. Mimicking the behaviour of classical monochromatic light fields they oscillate harmonically at the laser frequency ω_P, $|\beta(t)\rangle = \exp\left(-i\omega_P t b^\dagger b\right)|\beta\rangle = |\beta \exp\left(-i\omega_P t\right)\rangle$. They can be understood as the vacuum state in a displaced and rotating frame.[19] In the classical limit $|\beta| \gg 1$ the vacuum field fluctuations around the displacement amplitude are small compared to $|\beta|$, and we may substitute the laser mode operator b by $\beta \exp\left(-i\omega_P t\right)$ (assuming there is no relevant backaction of the cavity field onto the state of the driving laser). The driving Hamiltonian thus assumes the form $H_{\text{pump}}(t) \propto \beta^* \exp\left(i\omega_P t\right) a_0 + h.c.$ We get rid of the time dependence by switching to a frame rotating at the optical pump frequency ω_P, introducing the cavity-pump detuning $\Delta_0 = \omega_0 - \omega_P$ and the effective pump rate η. This leaves us with the master equation for the field state of a driven cavity mode,

$$\partial_t \rho = -i \left[\Delta_0 a_0^\dagger a_0 + i\eta a_0^\dagger - i\eta^* a_0, \rho \right] + \kappa_0 \left(2a_0 \rho a_0^\dagger - \left\{ a_0^\dagger a_0, \rho \right\} \right). \quad (2.56)$$

The quantum expectation value of the field amplitude evolves in the same way as the classical version (2.28),

---

[18] The form is easily obtained by adding the quantized physical fields (2.54) of the modes a_0 and b to an overall electric and magnetic field. When the corresponding field energy density is integrated over the volume in (2.4) the cross terms between both modes yield the above linear coupling Hamiltonian. Terms of the form $a_0 b$ and $a_0^\dagger b$ are omitted in the *rotating wave approximation* [45], since they oscillate rapidly at twice an optical frequency, $\omega_P + \omega_0$, and thus do not affect the actual mode coupling.

[19] A rotating frame is defined through the unitary state transformation $U(t) = \exp\left(i\omega_P \sum_n a_n^\dagger a_n \right)$, with ω_P the corresponding rotation frequency. Given the quantum state $\rho(t)$ of a system of field modes $\{a_n\}$ in the Schrödinger picture, the state in the rotating picture reads as $\rho' = U(t)\rho(t)U^\dagger(t)$. Analogously, a displaced frame is defined via the unitary displacement operator, $\rho' = D^\dagger(\beta)\rho D(\beta)$. Field observables are displaced as $D^\dagger(\beta) b D(\beta) = b + \beta$.

$$\partial_t \langle \mathsf{a}_0 \rangle = -(i\Delta_0 + \kappa_0)\langle \mathsf{a}_0 \rangle + \eta. \tag{2.57}$$

It is then straightforward to show that the coherent state $\rho_{ss} = |\alpha\rangle\langle\alpha|$ is the steady-state solution of the above master equation for the same steady-state amplitude $\alpha = \eta/(\kappa_0 + i\Delta_0)$ as in the classical case. An elegant and convenient way to incorporate the driving is to work with quantum states in the displaced frame, $\rho \mapsto \rho_\alpha = \mathsf{D}^\dagger(\alpha)\,\rho\mathsf{D}(\alpha)$, where the steady-state amplitude shifts the state of the mode from $|\alpha\rangle\langle\alpha|$ to the ground state $\mapsto |0\rangle\langle0|$. The resulting master equation,

$$\partial_t \rho_\alpha = -i\left[\Delta_0 \mathsf{a}_0^\dagger \mathsf{a}_0, \rho_\alpha\right] + \kappa_0\left(2\mathsf{a}_0 \rho_\alpha \mathsf{a}_0^\dagger - \left\{\mathsf{a}_0^\dagger \mathsf{a}_0, \rho_\alpha\right\}\right), \tag{2.58}$$

does not contain the explicit driving term anymore, and the field operator a_0 now represents the quantum field fluctuations on top of the coherent steady state.

Derivation of the loss term

Note that the non-Hamiltonian loss term in the master equation (2.56) can also be derived using a standard textbook approach [9, 47]. For this let us couple the cavity mode linearly to a bath of harmonic oscillators, $\mathsf{H}_{\text{env}} = \sum_j \hbar\omega_j \mathsf{b}_j^\dagger \mathsf{b}_j$. It represents the environmental vacuum of modes, which can be populated by a photon escaping the cavity. We shall assume a linear coupling term of the form $\mathsf{H}_{\text{int}} = \sum_j \hbar g_j \mathsf{a}_0 \mathsf{b}_j^\dagger + h.c.$, with g_j the effective photon exchange rates between cavity and environment. The coupled dynamics of the combined state $\rho_{SE}(t)$ of system and environment is most conveniently assessed in the interaction frame, $\rho_{SE,I}(t) = \mathsf{U}(t)\rho_{SE}(t)\mathsf{U}^\dagger(t)$, with $\mathsf{U}(t) = \exp\left[i\left(\mathsf{H}_0 + \mathsf{H}_{\text{env}}\right)t/\hbar\right]$. A formal integration and re-insertion of the von Neumann equation yields the integro-differential equation for the combined state,

$$\partial_t \rho_{SE,I}(t) = -\frac{i}{\hbar}\left[\mathsf{H}_I(t), \rho_{SE,I}(0)\right] - \frac{1}{\hbar^2}\int_0^t d\tau\,\left[\mathsf{H}_I(t), \left[\mathsf{H}_I(\tau), \rho_{SE,I}(\tau)\right]\right], \tag{2.59}$$

where

$$\mathsf{H}_I(t) = \mathsf{U}(t)\mathsf{H}_{\text{int}}\mathsf{U}^\dagger(t) = \sum_j \hbar g_j e^{i(\omega_j - \omega_0)t}\mathsf{a}_0\mathsf{b}_j^\dagger + h.c. \tag{2.60}$$

We obtain a closed equation for the reduced cavity state $\rho_I = \text{tr}_E\left(\rho_{SE,I}\right)$ by tracing out the environment and subsequently applying the so-called Born approximation: The cavity leaves the environment practically unaffected at all times, $\rho_{SE,I}(t) \approx \rho_I(t) \otimes |\text{vac}\rangle\langle\text{vac}|$. Every photon that espaces disperses almost immediately, and the cavity is thus effectively surrounded by vacuum[20] on all relevant time scales. We find

---

[20] Optical frequencies in the environmental mode spectrum are practically unoccupied even at finite temperatures. I thus use the zero-temperature vacuum state here, since the cavity only couples to modes of similar frequencies.

$$\partial_t \rho_I\left(t\right) = -\frac{1}{\hbar^2} \int\limits_0^t d\tau \, \mathrm{tr}_E\left(\left[\mathsf{H}_I\left(t\right), \left[\mathsf{H}_I\left(t-\tau\right), \rho_I\left(t-\tau\right) \otimes |\mathrm{vac}\rangle\langle\mathrm{vac}|\right]\right]\right)$$

$$= \sum_j \int\limits_0^t d\tau \, |g_j|^2 \, e^{-i(\omega_j - \omega_0)\tau} \left\{\mathsf{a}_0 \rho_I\left(t-\tau\right) \mathsf{a}_0^\dagger - \mathsf{a}_0^\dagger \mathsf{a}_0 \rho_I\left(t-\tau\right)\right\} + h.c.$$

$$(2.61)$$

Next we can apply the Markov approximation: The environment shall not memorize the cavity state at earlier times and the time evolution equation shall become time-local. That is to say, we may set $\rho_I\left(t-\tau\right) \approx \rho_I\left(t\right)$ and integrate up to infinity. This is formally justified if the cavity field couples to a sufficiently broad frequency range such that $\sum_j |g_j|^2 \exp\left[i\left(\omega_0 - \omega_j\right)\tau\right] \approx \kappa\delta\left(\tau\right)$ and

$$\partial_t \rho_I\left(t\right) \approx \kappa \left[2\mathsf{a}_0 \rho_I\left(t\right) \mathsf{a}_0^\dagger - \mathsf{a}_0^\dagger \mathsf{a}_0 \rho_I\left(t\right) - \rho_I\left(t\right) \mathsf{a}_0^\dagger \mathsf{a}_0\right]. \qquad (2.62)$$

The desired master equation (2.56) follows by combining this with the above driving term of a classical coherent laser field.

2.2.1.2 A Particle, a Driving Laser, and a Handful of Empty Cavity Modes

With the quantum model of a driven cavity mode at hand we can now collect all ingredients to model the system of a single pump mode, M empty cavity modes and a PPP, as sketched in Fig. 2.4. It will be expedient to work in a frame rotating at the optical frequency ω_P of the driving laser, with the pump mode displaced by the steady-state amplitude α. This results in a master equation term of the above form (2.58) for each of the $M + 1$ modes.

The presence of a polarizable particle comes with an additional Hamiltonian representing the optical potential, as well as with scattering and absorption contributions, which couple the motion of the particle to the field degrees of freedom. We obtain directly the optical potential term by quantizing the electric field expression $\boldsymbol{E}\left(\mathbf{r}\right)$ in the PPP Hamiltonian (2.9). However, we must bear in mind that the electric field is now given by a sum of all M cavity modes plus the displaced pump mode. This results in the total particle Hamiltonian

$$\mathsf{H}_{\mathrm{PPP}} = \overbrace{\frac{\mathbf{p}^2}{2m_P} + \hbar U_{00} |\alpha u_0\left(\mathbf{r}\right)|^2}^{=:\mathsf{H}_P} + \overbrace{\sum_{n=0}^M \hbar U_{0n}\left[\alpha \mathsf{a}_n^\dagger u_n^*\left(\mathbf{r}\right) u_0\left(\mathbf{r}\right) + h.c.\right]}^{=:\mathsf{H}_I}$$

$$+ \sum_{k,n=0}^M \hbar U_{kn} \mathsf{a}_n^\dagger \mathsf{a}_k u_n^*\left(\mathbf{r}\right) u_k\left(\mathbf{r}\right). \qquad (2.63)$$

The first term H_P describes the particle motion in the steady-state dipole potential, the second term H_I represents the pump-enhanced linear coupling of the particle to the field fluctuations in each cavity mode, and the remainder represents the inter-mode coupling, which also causes the position-dependent resonance shift of the modes.

The above Hamiltonian must be complemented by the field energy term in the displaced and rotating frame, $H_C = \sum_n \hbar \Delta_n a_n^\dagger a_n$. The free fields are thus included via the superoperator

$$\mathcal{L}_C (\rho) = -i \sum_{n=0}^{M} \Delta_n \left[a_n^\dagger a_n, \rho \right] + \sum_{n=0}^{M} \kappa_n \left(2 a_n \rho a_n^\dagger - \left\{ a_n^\dagger a_n, \rho \right\} \right). \qquad (2.64)$$

It describes the field evolution in the absence of the particle. In addition, the time evolution of the combined state of cavity and particle contains another two field loss terms $\mathcal{L}_{\text{abs}}$ and $\mathcal{L}_{\text{sca}}$ due to absorption and scattering,

$$\partial_t \rho = -\frac{i}{\hbar} \left[H_{\text{PPP}}, \rho \right] + \mathcal{L}_C (\rho) + \mathcal{L}_{\text{abs}} (\rho) + \mathcal{L}_{\text{sca}} (\rho). \qquad (2.65)$$

Both cause additional coupling between the particle motion and the field fluctuations. The explicit form of these terms is found by combining the original expressions (2.16) and (2.24) for a classical field with the above derivation of the Lindblad term (2.62), which represents the incoherent loss of single field quanta. Keeping the displacement of the pump mode in mind, we arrive at

$$\mathcal{L}_{\text{abs}} (\rho) = \sum_{n=0}^{M} \frac{c \sigma_{\text{abs}}}{V_n} \left[(a_n + \alpha \delta_{n0}) u_n (\mathbf{r}) \rho (a_n + \alpha \delta_{n0})^\dagger u_n^* (\mathbf{r}) \right.$$
$$\left. -\frac{1}{2} \left\{ (a_n + \alpha \delta_{n0})^\dagger (a_n + \alpha \delta_{n0}) |u_n (\mathbf{r})|^2, \rho \right\} \right], \qquad (2.66)$$

$$\mathcal{L}_{\text{sca}} (\rho) = \sum_{m=0}^{M} \frac{c \sigma_{\text{sca}}}{V_m} \left[(a_m + \alpha \delta_{m0}) u_m (\mathbf{r}) \int d^2 n \, R (\mathbf{n}) \, e^{-ik\mathbf{n}\cdot\mathbf{r}} \rho e^{ik\mathbf{n}\cdot\mathbf{r}} u_m^* (\mathbf{r}) \right.$$
$$\left. \times (a_m + \alpha \delta_{m0})^\dagger - \frac{1}{2} \left\{ (a_m + \alpha \delta_{m0})^\dagger (a_m + \alpha \delta_{m0}) |u_m (\mathbf{r})|^2, \rho \right\} \right].$$
$$(2.67)$$

Thermal or fluorescent photon emission from the particle into free space is neglected, as well as internal heating of the particle due to photon absorption.[21] In the following I will simplify the overall master equation (2.65) to the case of weak coupling.

---

[21] Practical implementations of the present cavity dissipation scheme are restricted to non-absorbing particle species. The typically large pump field intensities might otherwise lead to the destruction of the particle.

2.2.2 Eliminating the Quantum Field Dynamics in the Weak Coupling Limit

With the quantum model of the coupled cavity-particle dynamics at hand, I will now assess the general effect of the dynamical quantum field on the motion of the PPP. The goal is to find an effective description of the reduced particle state by eliminating the explicit field dynamics. We should expect that such a separation can formally be achieved only in the limit of weak coupling between the particle and the field. I will therefore introduce two weak coupling assumptions which will facilitate a low-order expansion of the coupling effect. Although the resulting model will be strictly valid under those assumptions only, we might retain its qualitative predictions even beyond the weak coupling limit.

2.2.2.1 The First Weak-Coupling Assumption

I assume that the coupling rates of the polarizable particle to the modes are significantly smaller than the mode damping rates, $|U_{mn}| \ll \kappa_n \; \forall m, n$. This means that the particle-induced cavity field fluctuations are limited to a few photons, as they typically escape the cavity much faster than they can be redistributed by the particle. The strong pump amplitude $|\alpha| \gg 1$ then represents the only potential source of large photon numbers that may populate empty modes through coherent scattering at the particle. We may thus omit those coupling terms in the Hamiltonian (2.63) which are of second order in the field fluctuations, $\mathsf{H}_{\mathrm{PPP}} \approx \mathsf{H}_P + \mathsf{H}_I$.

Secondly, if we extend the above weak-coupling assumption for the coherent inter-mode scattering rates to the rates of photon absorption and Rayleigh scattering, we may approximate the Lindblad terms (2.66) and (2.67) as

$$\mathcal{L}_{\mathrm{abs}} (\rho) \approx \gamma_{\mathrm{abs}} |\alpha|^2 \left[u_0 (\mathbf{r}) \rho u_0^* (\mathbf{r}) - \frac{1}{2} \left\{ |u_0 (\mathbf{r})|^2 , \rho \right\} \right], \tag{2.68}$$

$$\mathcal{L}_{\mathrm{sca}} (\rho) \approx \gamma_{\mathrm{sca}} |\alpha|^2 \left[\int \mathrm{d}^2 n \, R (\mathbf{n}) \, u_0 (\mathbf{r}) \, e^{-ik\mathbf{n}\cdot\mathbf{r}} \rho e^{ik\mathbf{n}\cdot\mathbf{r}} u_0^* (\mathbf{r}) - \frac{1}{2} \left\{ |u_0 (\mathbf{r})|^2 , \rho \right\} \right]. \tag{2.69}$$

The terms $\gamma_{\mathrm{abs,sca}} = c\sigma_{\mathrm{abs,sca}}/V_0$ denote the absorption and the Rayleigh scattering rate with respect to the pump mode volume V_0. According to our assumption, both the absorption and the scattering rate must be small compared to the cavity decay rates, and we can safely neglect their contribution to the particle-cavity dynamics. We are left with the momentum diffusion caused by the absorption and scattering of pump photons in (2.68) and (2.69); the only relevant non-conservative contributions to the model, apart from the cavity damping terms in $\mathcal{L}_C$.

The first weak-coupling assumption simplifies considerably the quantum description of cavity and particle at almost no costs. In fact, the assumption is very well fulfilled in practice by a wide range of nanoparticles, as can be seen from the exem-

plary Table 2.1. Using infrared light it remains valid up to a mass of roughly 10^8 amu. The quantum description of the weakly coupling system splits into the two separate superoperators $\mathcal{L}_C$ and $\mathcal{L}_P (\rho) = -i \left[\mathsf{H}_P, \rho \right] / \hbar + \mathcal{L}_{\mathrm{abs}} (\rho) + \mathcal{L}_{\mathrm{sca}} (\rho)$ acting solely on the cavity and particle subspace, respectively. The coupling of both subsystems is mediated by the effective interaction Hamiltonian

$$\mathsf{H}_I = \sum_{n=0}^{M} \hbar U_{0n} \alpha \mathsf{a}_n^\dagger u_n^* (\mathbf{r}) u_0 (\mathbf{r}) + h.c. \tag{2.70}$$

It resembles the standard linear coupling Hamiltonian, but with a coupling rate $|U_{0n}\alpha|$ enhanced by the strong pump field α. In principle, this allows a weakly coupling particle to enter the strong coupling regime $|U_{0n}\alpha| \gtrsim \kappa_n$ with the help of a sufficiently strong pump laser. Note that it requires only one driving mode to enhance the coupling of the particle to all the other modes that overlap with the pump field. However, cavity modes with a large detuning Δ_n cannot be addressed in practice, given that their oscillating amplitude a_n averages out in the interaction Hamiltonian. What counts are degenerate or near-degenerate resonator modes with a detuning of the order of the cavity linewidth. Only they contribute to the interaction. I will analyze the benefit of a large degenerate mode spectrum for cavity-induced cooling in Sect. 2.2.3.4.

While previous weak-coupling approaches towards the cavity-induced slowing of atoms [48] did not yet consider the pump enhancement (because it was not necessary there), it is a practiced technique in the field of optomechanics [49] to reach the strong coupling regime [50, 51]. There, however, the interaction is restricted to a single oscillatory degree of freedom of a rigid system such as a mirror or membrane. It is typically coupled to a single driven cavity mode a_0, and a low-order expansion of the respective mode function $u_0 (\mathbf{r})$ around the equilibrium value of the oscillator yields the standard optomechanical interaction Hamiltonian [52].

The pump enhancement facilitates the strong coupling of a weakly interacting nanoparticle to high-finesse cavity modes. It thus has the potential of inducing a substantial dissipative slowing effect. We have seen this already in the simple classical model calculation in Sect. 2.1.3.1, and I will study the strong coupling regime further in Sect. 2.3.3. On the other hand, an effective master equation for the reduced particle state can only be derived by adiabatically eliminating the cavity degrees of freedom. This requires an even stronger assumption.

2.2.2.2 The Second Weak-Coupling Assumption

I now assume in addition that even the pump-enhanced coupling rates are small compared to the decay rates of all relevant cavity modes, $|U_{0n}\alpha| \ll \kappa_n \ \forall n$. In other words, any excitation of the cavity field will always leak out much faster than it can be built up by the in-mode scattering of pump photons off the particle. As a consequence, the M cavity modes (and the pump mode) will remain empty (relative to the pump displacement) at almost all times, $\left\langle \mathsf{a}_n^\dagger \mathsf{a}_n \right\rangle \ll 1$.

Obviously, the second weak-coupling assumption represents a very restrictive condition, which one should be anxious to violate in actual experiments in order to achieve a significant slowing effect. Still, I make the assumption here to define an effective quantum description of the particle motion under the dissipative influence of the cavity. It will provide us with a clear and rigorous understanding of the origin of cavity-induced friction and diffusion effects. Judging from complementary semi-classical treatments and numerical simulations [48, 53], we should expect the basic features and qualitative behaviour of those effects to remain valid in a strong-coupling regime where our effective quantum model will break down.

In the following I derive the effective master equation for the reduced particle state by employing the projection formalism [54–56]. For this let me define a superoperator $\mathcal{P}$ as the projection of the combined cavity-particle state on the cavity ground state in the displaced frame, $\mathcal{P}\rho = \mathrm{tr}_C(\rho) \otimes |\mathrm{vac}\rangle\langle\mathrm{vac}|$. The complementary projection shall be denoted by $\mathcal{Q} = \mathrm{id} - \mathcal{P}$. As both superoperators represent orthogonal projections in operator space ($\mathcal{P}^2 = \mathcal{P}$, $\mathcal{Q}^2 = \mathcal{Q}$ and $\mathcal{P}\mathcal{Q} = \mathcal{Q}\mathcal{P} = 0$), the master equation $\partial_t \rho = -i\left[\mathsf{H}_I, \rho\right]/\hbar + \mathcal{L}_C(\rho) + \mathcal{L}_P(\rho)$ can be divided into two coupled equations for $\mathcal{P}\rho$ and $\mathcal{Q}\rho$ with help of the following relations:

- Both superprojectors $\mathcal{P}$ and $\mathcal{Q}$ commute with the master equation term $\mathcal{L}_P$, that is, $\mathcal{P}\mathcal{L}_P = \mathcal{L}_P\mathcal{P} = \mathcal{P}\mathcal{L}_P\mathcal{P}$ and $\mathcal{Q}\mathcal{L}_P = \mathcal{L}_P\mathcal{Q} = \mathcal{Q}\mathcal{L}_P\mathcal{Q}$. The reason is that the projectors act solely on the field degrees of freedom, whereas $\mathcal{L}_P$ operates on the particle subspace.
- The relation $\mathcal{L}_C\mathcal{P} = 0$ is obviously true since $\mathcal{P}$ singles out the cavity vacuum state.
- The flipped relation $\mathcal{P}\mathcal{L}_C = 0$ holds as well since $\mathcal{L}_C$ is restricted to the cavity subspace and traceless by construction, $\mathrm{tr}(\mathcal{L}_C\rho) = \mathrm{tr}_C(\mathcal{L}_C\rho) = 0$.
- It follows immediately from the previous two points that $\mathcal{Q}\mathcal{L}_C = \mathcal{L}_C\mathcal{Q} = \mathcal{Q}\mathcal{L}_C\mathcal{Q}$.
- The relation $\mathcal{P}\mathcal{L}_I\mathcal{P} = 0$, with $\mathcal{L}_I(\rho) = -i\left[\mathsf{H}_I, \rho\right]/\hbar$, can easily be verified by plugging in the explicit form of the coupling Hamiltonian (2.70) and noting that $\langle\mathrm{vac}|\mathsf{H}_I|\mathrm{vac}\rangle = 0$.

Putting everything together we arrive at the coupled equations

$$\partial_t \mathcal{P}\rho(t) = \mathcal{P}\mathcal{L}_P\mathcal{P}\rho(t) + \mathcal{P}\mathcal{L}_I\mathcal{Q}\rho(t), \tag{2.71}$$

$$\partial_t \mathcal{Q}\rho(t) = \mathcal{Q}(\mathcal{L}_P + \mathcal{L}_C)\mathcal{Q}\rho(t) + \mathcal{Q}\mathcal{L}_I\mathcal{P}\rho(t) + \mathcal{Q}\mathcal{L}_I\mathcal{Q}\rho(t). \tag{2.72}$$

The initial conditions at time $t = 0$ shall be given by the initial state $\rho_P(0)$ of the particle and the steady state of the cavity system, $\mathcal{P}\rho(0) = \rho_P(0) \otimes |\mathrm{vac}\rangle\langle\mathrm{vac}|$ and $\mathcal{Q}\rho(0) = 0$. The second weak-coupling assumption will now form the basis of three steps of approximation that will finally lead to a closed equation for $\mathcal{P}\rho(t)$ and for the reduced particle state $\rho_P(t) = \langle\mathrm{vac}|\mathcal{P}\rho(t)|\mathrm{vac}\rangle$.

Recall that any particle-induced field excitations in the weak-coupling limit are assumed to decay before they can add up or disperse over the system of modes. The state of the cavity is thus well approximated by the vacuum at almost all times, and the component $\mathcal{Q}\rho$ can be regarded as a small correction to the full quantum state

$\rho = \mathcal{P}\rho + \mathcal{Q}\rho$. This component will only be occupied at the effective coupling rates $|U_{0n}\alpha|$ via the term $\mathcal{QL}_I\mathcal{P}\rho$ in (2.72), while the term $\mathcal{QL}_C\mathcal{Q}\rho$ causes it to decay on a much faster time scale of the order of the cavity lifetimes $1/\kappa_n$. The assumption $|U_{0n}\alpha| \ll \kappa_n$ allows us to neglect the 'second order' term $\mathcal{QL}_I\mathcal{Q}\rho$, which would describe the back-action of persistent field excitations on the particle. The remainder can be formally integrated respecting the initial condition $\mathcal{Q}\rho\,(0) = 0$,

$$\mathcal{Q}\rho\,(t) = \int_0^t \mathrm{d}\tau \; \mathcal{Q}e^{(\mathcal{L}_C+\mathcal{L}_P)(t-\tau)}\mathcal{QL}_I\mathcal{P}\rho\,(\tau)\,. \tag{2.73}$$

Inserting this into Eq. (2.71), we arrive at a closed integro-differential equation for the vacuum component,

$$\partial_t\mathcal{P}\rho\,(t) = \mathcal{PL}_P\mathcal{P}\rho\,(t) + \int_0^t \mathrm{d}\tau \; \mathcal{PL}_I\mathcal{Q}e^{(\mathcal{L}_C+\mathcal{L}_P)(t-\tau)}\mathcal{QL}_I\mathcal{P}\rho\,(\tau)$$

$$= \mathcal{L}_P\mathcal{P}\rho\,(t) + \int_0^t \mathrm{d}\tau \; \mathcal{PL}_Ie^{(\mathcal{L}_C+\mathcal{L}_P)\tau}\mathcal{L}_I\mathcal{P}\rho\,(t-\tau)\,, \tag{2.74}$$

which depends on the whole past trajectory of $\mathcal{P}\rho$. The integral represents the small correction to the particle state evolution in the absence of field fluctuations. A standard way of converting the above expression to a time-local differential equation is to expand it as $\mathcal{P}\rho = \mathcal{P}\rho_0 + \mathcal{P}\rho_1 + \ldots$ using the following iteration process: First one formally solves the time-local equation in the absence of the integral term to obtain the zeroth order solution $\mathcal{P}\rho_0\,(t) = \exp\left[\mathcal{L}_P\,(t-t_0)\right]\mathcal{P}\rho_0\,(t_0)$. This is then plugged into the correction term to obtain an equation for the first-order term $\mathcal{P}\rho_1$, which is again solved in the absence of the next-order correction, and so forth. Here we are only interested in the lowest order, which leaves us with the equation

$$\partial_t\mathcal{P}\rho\,(t) \approx \mathcal{L}_P\mathcal{P}\rho\,(t) + \int_0^t \mathrm{d}\tau \; \mathcal{PL}_Ie^{\mathcal{L}_C\tau}e^{\mathcal{L}_P\tau}\mathcal{L}_Ie^{\mathcal{L}_P(t-\tau-t_0)}\mathcal{P}\rho\,(t_0)\,, \tag{2.75}$$

with $t_0 > 0$ an arbitrary initial time. I have separated the time evolution under $\mathcal{L}_C$ and $\mathcal{L}_P$ since the superoperators commute as they act on distinct subsystems.

Unfortunately, we are now running into trouble when we try to make this equation time-local by setting $t_0 = t$. Temporal inversion of the particle evolution $\mathcal{L}_P$ is not allowed due to the non-unitary contributions $\mathcal{L}_{\mathrm{abs,sca}}$ of absorption and Rayleigh scattering, which increase the entropy of the particle state by diffusion.

Fortunately, we can generally neglect the non-unitary parts when the weak-coupling conditions hold. This is because the past-trajectory integral in (2.75) involves only time periods τ of the order of the cavity lifetimes $1/\kappa_n$ as the rapid

cavity decay term in $\exp\left(\mathcal{L}_C\tau\right)$ suppresses the coupling term $\mathcal{L}_I$. During that period, absorption and scattering events changing the particle momentum in units of $\hbar k$ occur at the rates $\gamma_{\mathrm{abs,sca}}\left|\alpha\right|^2$. We can safely ignore them if they do not modify the particle's momentum $m_P v = \langle\left|\mathbf{p}\right|\rangle$ too much,

$$\frac{\gamma_{\mathrm{abs,sca}}\left|\alpha\right|^2}{\kappa_n}\left|\frac{2\omega_r}{kv}\right| \ll 1 \; \forall n. \tag{2.76}$$

As once again illustrated in Table 2.1 typical nanoparticles (in the absence of strong internal resonances close to the laser frequency) exhibit scattering and absorption rates smaller than their respective coupling frequencies. The weak-coupling limit thus implies $\gamma_{\mathrm{abs,sca}}\left|\alpha\right| \ll \left|U_0\alpha\right| \ll \kappa_n$. At the same time, the massive molecules and nanoparticles of interest feature sub-kHz recoil frequencies $\omega_r = \hbar k^2/2m_P$ when interacting with infrared light. This must be compared to Doppler frequencies of $kv \sim 4\,\mathrm{MHz} \gg \omega_r$ at rather low velocities of $v \sim 1\,$m/s; such slow particles are still orders of magnitude away from the quantum limit of motion.

Moreover, given that the integral in (2.75) is restricted by the integrand to times $\tau \lesssim 1/\kappa_n$, we can replace the upper integral bound by infinity. This leaves us with the time-local equation

$$\partial_t \mathcal{P}\rho\left(t\right) \approx \left[\mathcal{L}_P + \int_0^\infty \mathrm{d}\tau\,\mathcal{P}\mathcal{L}_I e^{\mathcal{L}_C\tau}\mathcal{L}_I\left(\tau\right)\right]\mathcal{P}\rho\left(t\right), \tag{2.77}$$

where $\mathcal{L}_I\left(\tau\right)$ represents the von Neumann commutator with the back-in-time-evolved coupling Hamiltonian

$$\mathsf{H}_I\left(\tau\right) = e^{-i\mathsf{H}_P\tau/\hbar}\mathsf{H}_I e^{i\mathsf{H}_P\tau/\hbar} = \sum_{n=0}^M \hbar U_{0n}\alpha\mathsf{a}_n^\dagger u_n^*\left(\mathbf{r},\mathbf{p};\tau\right)u_0\left(\mathbf{r},\mathbf{p};\tau\right) + h.c., \tag{2.78}$$

$$u_n\left(\mathbf{r},\mathbf{p};\tau\right) = u_n\left(\exp\left[\frac{i\mathbf{p}^2\tau}{2m_P\hbar} + iU_{00}\left|\alpha u_0\left(\mathbf{r}\right)\right|^2\tau\right]^\dagger \mathbf{r}\exp\left[\frac{i\mathbf{p}^2\tau}{2m_P\hbar} + iU_{00}\left|\alpha u_0\left(\mathbf{r}\right)\right|^2\tau\right]\right). \tag{2.79}$$

2.2.2.3 Effective Time Evolution of the Reduced Particle State

The time-local expression (2.77) is now easily turned into an effective time evolution equation for the reduced particle state $\rho_P\left(t\right) = \mathrm{tr}_C\left[\rho\left(t\right)\right]$,

$$\partial_t \rho_P(t) = \langle vac|\partial_t \mathcal{P}\rho(t)|vac\rangle = -\frac{i}{\hbar}\left[\mathsf{H}_P, \rho_P(t)\right]$$

$$-\frac{1}{\hbar^2}\int_0^\infty d\tau \, \mathrm{tr}_C\left\{\left[\mathsf{H}_I, e^{\mathcal{L}_C \tau}\left[\mathsf{H}_I(\tau), \rho_P(t) \otimes |vac\rangle\langle vac|\right]\right]\right\}. \quad (2.80)$$

The free evolution under $\mathcal{L}_C$ and the trace over the cavity subsystem can be performed straightforwardly,[22]

$$\partial_t \rho_P(t) = \mathcal{L}_P \rho_P(t) - \sum_{n=0}^{M} |U_{0n}\alpha|^2 \left(\left[u_0^*(\mathbf{r}) u_n(\mathbf{r}), \mathsf{g}_n \rho_P(t)\right] + h.c.\right). \quad (2.81)$$

Here I introduce the so-called *memory operators*

$$\mathsf{g}_n = \int_0^\infty d\tau \, e^{-(\kappa_n + i\Delta_n)\tau} u_n^*(\mathbf{r}, \mathbf{p}; \tau) u_0(\mathbf{r}, \mathbf{p}; \tau). \quad (2.82)$$

They collect the particle-induced coupling between the pump field and the cavity modes over a short period of time before the present time t. In other words, they represent the delayed reaction of each cavity mode to the position of the particle that continuously scatters pump light into them. The delay, or memory time scale, is determined by the damping rate κ_n and the detuning Δ_n of each mode.

Once again, we can approximate the past trajectory of sufficiently fast particles by neglecting the influence of the optical potential on short time scales. We may follow the same line of argument as in the case of absorption and Rayleigh scattering. The optical dipole potential of a standing-wave pump mode[23] can be viewed as a coherent backscattering process of pump photons within the mode and at the rate $U_{00}|\alpha|^2$. As each backscattering event transfers $2\hbar k$ of momentum to the particle, we find that the optical potential is negligible in the limit of

$$\left|\frac{U_{00}|\alpha|^2}{\kappa_n}\frac{4\omega_r}{kv}\right| \ll 1 \,\forall n. \quad (2.83)$$

If this is the case we can explicitly write

---

[22] Applying the interaction Hamiltonian to the vacuum state leads to nondiagonal elements of the form $|1_n\rangle\langle vac|$, with $|1_n\rangle = \mathsf{a}_n^\dagger|vac\rangle$ a single-excitation multimode Fock state. One can easily show that these nondiagonals evolve like $\exp(\mathcal{L}_C t)|1_n\rangle\langle vac| = \exp(-\kappa_n t - i\Delta_n t)|1_n\rangle\langle vac|$.

[23] Running-wave modes do not exhibit a wavelength-scale oscillatory intensity pattern. Their influence on the particle through the optical potential is considerably weaker.

$$\mathsf{g}_n \approx \int\limits_0^\infty d\tau\, e^{-(\kappa_n + i\Delta_n)\tau} u_n^* \left(\mathbf{r} - \frac{\mathbf{p}\tau}{m_P}\right) u_0 \left(\mathbf{r} - \frac{\mathbf{p}\tau}{m_P}\right). \tag{2.84}$$

The memory operators then average the inter-mode coupling over an approximately straight particle trajectory reaching a few mode lifetimes into the past. Note that the above condition (2.83) is only relevant for a standing-wave pump mode directed along the axis of the other cavity modes. In an orthogonal configuration with a running-wave pump field, as depicted in Fig. 2.4, the optical dipole force merely scales with the transverse pump laser profile.[24]

I will discuss in the following section that the delay effect is responsible for cavity-induced friction forces and the potential slowing of the particle. It vanishes in the limit of far-detuned or bad cavity modes, when the field fluctuations can follow the moving particle almost instantaneously. This happens in the limit of $|kv| \ll \kappa_n, |\Delta_n|$, as the Doppler frequency determines the rate at which the particle-induced coupling changes during motion. We may then approximate $\mathsf{g}_n \approx u_n^*(\mathbf{r}) u_0(\mathbf{r}) / (\kappa_n + i\Delta_n)$ leaving us with the completely positive Lindblad-type master equation

$$\partial_t \rho_P = -\frac{i}{\hbar} \left[\mathsf{H}_P - \sum_{n=0}^M \frac{\hbar\Delta_n |U_{0n}\alpha|^2}{\kappa_n^2 + \Delta_n^2} |u_0(\mathbf{r}) u_n(\mathbf{r})|^2, \rho_P \right] + \mathcal{L}_{\text{abs}}\rho_P + \mathcal{L}_{\text{sca}}\rho_P$$

$$+ \sum_{n=0}^M \frac{\kappa_n |U_{0n}\alpha|^2}{\kappa_n^2 + \Delta_n^2} \left[2u_n^*(\mathbf{r}) u_0(\mathbf{r}) \rho_P u_0^*(\mathbf{r}) u_n(\mathbf{r}) - \left\{ |u_0(\mathbf{r}) u_n(\mathbf{r})|^2, \rho_P \right\} \right]. \tag{2.85}$$

Apart from the addition to the Hamiltonian, it features a positive Lindblad term, which is form-equivalent to the Rayleigh scattering term (2.69). Bad cavity modes simply act as an additional diffusion channel for the particle. On the other side, even good cavity modes will result in a mere momentum diffusion when the particle is sufficiently slow.

2.2.3 Semiclassical Description of Friction and Diffusion

Based on the effective evolution equation (2.81) and the memory operator (2.84) for a particle in the presence of a strongly driven pump and M empty cavity modes, I will formulate the resulting dissipative dynamics using a semiclassical phase-space picture.

To keep things simple and clear let me trace out the particle's xy-motion and resort to a one-dimensional version of the present model along the z-axis of the

---

[24] Condition (2.83) would be alleviated by a factor $kw \ll 1$ in the case of a Gaussian profile with waist w.

standing-wave modes of the cavity, $u_n(x, y, z) \mapsto f_n(x, y) u_n(z)$. This is where a moving particle can cause the fastest field modulation and the most delayed reaction by the cavity. Dissipative effects, and indeed any field-induced forces on the particle, are expected to be much weaker in the xy-directions, given that the transverse mode profiles of the cavity $f_n(x, y)$ extend over much more than a wavelength. To be concrete, the delayed cavity-backaction on the transverse motion is negligible for velocities $|v_{x,y}/w_n| \ll \kappa_n, \Delta_n$, with w_n the characteristic transverse width of the nth mode (as given by the waist in case of an xy-symmetric Gaussian mode profile).

We are left with the one-dimensional memory operator

$$\mathsf{g}_n^{(z)} = \int_0^\infty d\tau\, e^{-(\kappa_n + i\Delta_n)\tau} u_n^*\left(\mathsf{z} - \frac{\mathsf{p}\tau}{m_P}\right) u_0\left(\mathsf{z} - \frac{\mathsf{p}\tau}{m_P}\right). \tag{2.86}$$

for the z-state of the particle, at fixed transverse coordinates x and y. The latter can be sufficiently well described by a straight classical trajectory (x_t, y_t) if we assume that the particle is hardly affected in its transverse motion while it passes the high-intensity region of the cavity. This effective parametric time dependence can be incorporated, if necessary, in the coupling frequencies, $\widetilde{U}_{mn}(t) = U_{mn} f_m^*(x_t, y_t) f_n(x_t, y_t)$, as already done in the simple classical model of cavity-induced slowing in Sect. 2.1.3. For the time being I will simply ignore the transverse trajectory when assessing the one-dimensional friction and diffusion effects. Nevertheless, one should take notice of this time dependence when estimating the overall effect in realistic scenarios. The one-dimensional slowing of the z-motion of a particle crossing the cavity, for instance, would have to be averaged over its limited residence time inside the pump mode. In the complementary case of a trapped particle that overlaps with the cavity modes, one could average the slowing effect over each trapping cycle. In such scenarios, the cavity system could well be given by the configuration sketched in Fig. 2.4, or by the simpler setup of Fig. 2.1, where a single Fabry-Pérot mode is directly pumped by a laser.

The starting point shall now be the master equation for the one-dimensional state of motion ρ, as obtained from (2.85) using the discussed simplifications,

$$\begin{aligned}
\partial_t \rho = {} & -\frac{i}{\hbar}\left[\frac{\mathsf{p}^2}{2m_P} + \hbar\widetilde{U}_{00}\,|\alpha u_0(\mathsf{z})|^2, \rho\right] \\
& - \sum_{n=0}^M |\widetilde{U}_{0n}\alpha|^2 \left(\left[u_0^*(\mathsf{z})\,u_n(\mathsf{z}), \mathsf{g}_n^{(z)}\rho\right] + h.c.\right) \\
& + \widetilde{\gamma}_{\mathrm{abs}}\,|\alpha|^2\left[u_0(\mathsf{z})\,\rho u_0^*(\mathsf{z}) - \frac{1}{2}\left\{|u_0(\mathsf{z})|^2, \rho\right\}\right] \\
& + \widetilde{\gamma}_{\mathrm{sca}}\,|\alpha|^2\left[\int d^2n\, R(\boldsymbol{n})\, u_0(\mathsf{z})\, e^{-ikn_z\mathsf{z}}\rho e^{ikn_z\mathsf{z}} u_0^*(\mathsf{z}) - \frac{1}{2}\left\{|u_0(\mathsf{z})|^2, \rho\right\}\right].
\end{aligned} \tag{2.87}$$

2.2.3.1 Friction and Diffusion Terms in the Fokker-Planck Equation

The effective friction force and diffusion effect can now be extracted in a standard procedure [57] from the phase-space representation of the above master equation (2.87); the resulting partial differential equation can be expanded in orders of $\hbar$, and the respective friction and diffusion terms can be identified by comparison to the standard form of a Fokker-Planck equation [9, 26, 58].

For this purpose I introduce the Wigner function,

$$w(z, p) = \frac{1}{2\pi\hbar} \int ds\, e^{ips/\hbar} \langle z - \frac{s}{2} | \rho | z + \frac{s}{2} \rangle, \qquad (2.88)$$

which represents the one-dimensional quantum state of motion ρ in a phase-space picture with position and momentum coordinates $(z, p) \in \mathbb{R}^2$. It is a real-valued and normalized function, $\int dz dp\, w(z, p) = 1$, and it can be regarded as the natural quantum generalization of the phase-space distribution function $f(z, p) \geq 0$ of a classical particle state [36, 59]. The Wigner function of sufficiently mixed states, such as the thermal state $\rho_{\text{th}} \propto \exp\left(-\mathsf{p}^2/2m_P k_B T\right)$, is in fact indistinguishable from its counterpart in a purely classical description, the Maxwell-Boltzmann distribution $w_{\text{th}}(z, p) = f_{\text{th}}(z, p) \propto \exp\left(-p^2/2m_P k_B T\right)$. At the same time, the time evolution equation for the Wigner function equals the classical Liouville equation up to second order in Planck's quantum of action $\hbar$ if it is governed by a conservative force field [59]. See Appendix A.3 for detailed expressions. In particular, the time evolution under at most harmonic potentials $V(z) = a + bz + cz^2$ is exactly the same in both the quantum and the classical case.

Using the phase-space translation rules given in Appendix A.3 we can translate the above master equation (2.87) into a partial differential equation for the corresponding Wigner function. If, in addition, we omit any derivatives higher than second order in position and momentum we will arrive at a Fokker-Planck-type equation (FPE) of the generic form [9]

$$\partial_t w(z, p) = -\partial_z \left[g_z(z, p) w(z, p) \right] - \partial_p \left[g_p(z, p) w(z, p) \right] + \frac{1}{2} \partial_z^2 \left[D_{zz}(z, p) w(z, p) \right]$$

$$+ \frac{1}{2} \partial_p^2 \left[D_{pp}(z, p) w(z, p) \right] + \partial_z \partial_p \left[D_{zp}(z, p) w(z, p) \right] + \mathcal{O}\left(\hbar^3\right). \quad (2.89)$$

We note that this approximation can also be understood as a semiclassical expansion of the Wigner time evolution up to the second order in $\hbar$. Each term in the FPE has a clear physical meaning which becomes evident when looking at the time evolution of the position and momentum expectation values as well as their second moments,[25]

---

[25] Here I make use of the procedure of integration by parts and of the fact that a well-behaved and normalizable Wigner function should vanish at the infinities.

$$\partial_t \langle \mathsf{z} \rangle = \int \mathrm{d}z \mathrm{d}p \, z \partial_t w \left(z, p\right) = \int \mathrm{d}z \mathrm{d}p \, g_z \left(z, p\right) w \left(z, p\right), \tag{2.90}$$

$$\partial_t \langle \mathsf{p} \rangle = \int \mathrm{d}z \mathrm{d}p \, g_p \left(z, p\right) w \left(z, p\right), \tag{2.91}$$

$$\partial_t \left\langle \mathsf{z}^2 \right\rangle = \int \mathrm{d}z \mathrm{d}p \left[2 z g_z \left(z, p\right) + D_{zz} \left(z, p\right)\right] w \left(z, p\right), \tag{2.92}$$

$$\partial_t \left\langle \mathsf{p}^2 \right\rangle = \int \mathrm{d}z \mathrm{d}p \left[2 p g_p \left(z, p\right) + D_{pp} \left(z, p\right)\right] w \left(z, p\right), \tag{2.93}$$

$$\partial_t \langle \mathsf{zp} + \mathsf{pz} \rangle = 2 \int \mathrm{d}z \mathrm{d}p \left[p g_z \left(z, p\right) + z g_p \left(z, p\right) + D_{zp} \left(z, p\right)\right] w \left(z, p\right). \tag{2.94}$$

The term g_z describes the overall drift of the position coordinate, the other drift term g_p represents the force field acting on the ensemble state. The combined diffusion of both the position and the momentum coordinate, which leads to an increase in the occupied phase-space area, is related to the diffusion matrix[26] $D_{jk} \left(z, p\right)$. An alternative way to describe the semiclassical motion of a particle is to work with a set of stochastic Langevin equations for position and momentum random variables, which reproduces the same ensemble-averaged time evolution as the FPE [26].

Let me split the phase-space representation of the state evolution (2.87) into a coherent part as well as a dissipative and a diffusive part,

$$\partial_t w \left(z, p\right) = \left[\partial_t w \left(z, p\right)\right]_{\mathrm{coh}} + \left[\partial_t w \left(z, p\right)\right]_{\mathrm{dis}} + \left[\partial_t w \left(z, p\right)\right]_{\mathrm{dif}}, \tag{2.95}$$

following my notation in [1]. The first part is associated to the first line in (2.87) which describes the conservative motion under the optical potential of the pumped mode. The second part represents the second line and contains the delayed reaction of all cavity modes. The remainder, that is, the momentum diffusion by absorption and elastic light scattering, is contained in the last part. All three parts are Taylor-expanded and brought into the semiclassical FPE form in a tedious but straightforward calculation with help of the tools in the appendix.

The coherent part

A second-order expansion of the coherent part yields

$$\left[\partial_t w \left(z, p\right)\right]_{\mathrm{coh}} = -\frac{p}{m_P} \partial_z w \left(z, p\right) + \hbar \widetilde{U}_{00} \partial_z \left|\alpha u_0 \left(z\right)\right|^2 \partial_p w \left(z, p\right) + \mathcal{O} \left(\hbar^3\right). \tag{2.96}$$

This equation describes a deterministic evolution of the system along classical trajectories in the dipole force field the pump mode. The conservative motion does not lead to any diffusion effect. This semiclassical approximation amounts to omitting any diffraction effects and treating the motion through the optical potential in a

---

[26] The diffusion matrix generally should be positive semidefinite in order to ensure that the occupied phase-space area increases and that the time evolution produces physical states at all times.

purely classical manner.[27] The lowest order quantum corrections originate from the non-conservative parts of the time evolution.

The dissipative part

Our main interest lies in the dissipative part of the motion, which contains the cavity-induced friction force. The phase-space representation of the memory operators (2.86),

$$
G_n (z, p) = \int_0^\infty d\tau \, e^{-(\kappa_n + i\Delta_n)\tau} u_n^* \left(z - \frac{p\tau}{m_P} \right) u_0 \left(z - \frac{p\tau}{m_P} \right), \tag{2.97}
$$

and several steps of calculation lead to the following additions to the force and to the diffusion:

$$
g_p^{(\text{dis})} (z, p) = \sum_{n=0}^{M} \left| \tilde{U}_{0n} \alpha \right|^2 \mathfrak{Re} \left\{ 2i\hbar G_n (z, p) \, \partial_z u_0^* (z) \, u_n (z) \right.
$$
$$
\left. - \hbar^2 \left[\partial_p G_n (z, p) \right] \partial_z^2 u_0^* (z) \, u_n (z) \right\}, \tag{2.98}
$$

$$
D_{pp}^{(\text{dis})} (z, p) = \sum_{n=0}^{M} 2\hbar^2 \left| \tilde{U}_{0n} \alpha \right|^2 \mathfrak{Re} \left\{ \left[\partial_z G_n (z, p) \right] \partial_z u_0^* (z) \, u_n (z) \right\}, \tag{2.99}
$$

$$
D_{zp}^{(\text{dis})} (z, p) = - \sum_{n=0}^{M} \hbar^2 \left| \tilde{U}_{0n} \alpha \right|^2 \mathfrak{Re} \left\{ \left[\partial_p G_n (z, p) \right] \partial_z u_0^* (z) \, u_n (z) \right\}. \tag{2.100}
$$

There is no dissipative contribution to the drift and the diffusion of the position coordinate, $g_z^{(\text{dis})} = D_{zz}^{(\text{dis})} = 0$. The memory effect due to the delayed cavity reaction lies in the memory term $G_n (z, p)$. It is responsible for the velocity dependence of the dissipation force which may result in a net friction effect. I will analyze the dissipative contributions in more details for specific cavity configurations below.

The diffusive part

The absorption and elastic scattering of pump photons contributes an additional momentum diffusion effect, as we have already seen in Sect. 2.1.2. It complements the non-conservative influence of the high-finesse cavity by the following terms:

$$
g_p^{(\text{dif})} (z, p) = 2\hbar (\gamma_{\text{abs}} + \gamma_{\text{sca}}) |\alpha|^2 \mathfrak{Im} \left\{ u_0 (z) \, \partial_z u_0^* (z) \right\}, \tag{2.101}
$$
$$
D_{pp}^{(\text{dif})} (z, p) = \hbar^2 |\alpha|^2 \left[(\gamma_{\text{abs}} + \gamma_{\text{sca}}) |\partial_z u_0 (z)|^2 + \gamma_{\text{sca}} k^2 \left\langle n_z^2 \right\rangle |u_0 (z)|^2 \right]. \tag{2.102}
$$

---

[27] This would be a bad approximation if the underlying quantum state would be a delocalized matter-wave state that could be diffracted by the standing-wave structure of the pump mode (see Sect. 2.1.4).

They must be added to Eqs. (2.98) and (2.99), respectively. Scattering and absorption mainly enhance the momentum diffusion by $D_{pp}^{\text{(dif)}} \geq 0$. Only for complex running-wave modes u_0 with a directed net momentum flow, there is a radiation-pressure addition $g_p^{\text{(dif)}}$ to the dissipative force (2.98). The diffusion effect consists of two parts related to the absorption and to the scattering of pump photons. The latter depends on the angular scattering distribution of the particle, which is given by the dipole pattern $R(\boldsymbol{n}) = 3\left[1 - (\boldsymbol{n} \cdot \boldsymbol{\epsilon})^2\right]/8\pi$ in the case of a PPP and a pump mode polarization $\boldsymbol{\epsilon}$ perpendicular to the z-axis.[28] This leaves us with $\langle n_z^2 \rangle = \int \mathrm{d}^2 n\, R(\boldsymbol{n})\, n_z^2 = 2/5$.

2.2.3.2 Conditions for Cavity-Induced Slowing

The velocity-dependent part of the overall force acting on the particle lies solely in the expression (2.98) which is a sum over $M+1$ single-mode force terms, $g_p^{\text{(dis)}}(z, p) = \sum_{n=0}^{M} g_p^{(n)}(z, p)$. The potential motional damping induced by each mode can be made explicit by a first-order expansion in the limit of low particle velocities,

$$g_p^{(n)}(z, p) = g_p^{(n)}(z, 0) + \beta^{(n)}(z)\, p + \mathcal{O}\left(p^2\right). \qquad (2.103)$$

The delayed reaction of the nth cavity mode damps the motion when the respective friction coefficient $\beta^{(n)}(z)$ is negative, otherwise it accelerates the particle. To be concrete, the above low-velocity expansion is valid when the Wigner function of the particle covers mainly those velocities $v = p/m_P$ that correspond to a Doppler shift $|kv| < \kappa_n$. The field fluctuations in the nth mode then lag behind the particle motion only a little and we may expand the memory function (2.97) to

$$G_n(z, p) = \frac{u_n^*(z)\, u_0(z)}{\kappa_n + i\Delta_n} - \frac{p}{m_P} \frac{\partial_z u_n^*(z)\, u_0(z)}{(\kappa_n + i\Delta_n)^2} + \frac{p^2}{m_P^2} \frac{\partial_z^2 u_n^*(z)\, u_0(z)}{(\kappa_n + i\Delta_n)^3} + \mathcal{O}\left(p^3\right).$$
$$(2.104)$$

We arrive at the friction coefficient

$$\beta^{(n)}(z) = -\frac{4\hbar\, |\tilde{U}_{0n}\alpha|^2\, \kappa_n}{m_P\left(\kappa_n^2 + \Delta_n^2\right)^2} \left[\Delta_n\, |\partial_z u_0^*(z)\, u_n(z)|^2 + \frac{\hbar\left(\kappa_n^2 - 3\Delta_n^2\right)}{2m_P\left(\kappa_n^2 + \Delta_n^2\right)} |\partial_z^2 u_0^*(z)\, u_n(z)|^2\right].$$
$$(2.105)$$

Note that the z-derivative of the mode function is proportional to $\partial_z \sim k$. Hence, the two terms in the brackets correspond to first and second orders in the recoil frequency $\omega_r = \hbar k^2/2m_P$, which is assumed to be small, $\omega_r \ll \kappa_n, |\Delta_n|$. We may thus neglect the second order contribution for all practical purposes (except for the marginal cases where the first order term vanishes) and focus entirely on the first term.

---

[28] Rayleigh scattering can be viewed as absorption and immediate reemission of a pump photon into free space. The absorption is responsible for the radiation pressure force, whereas the reemission does not contribute on average because there is no preferred direction of scattering, $\langle n_z \rangle = \int \mathrm{d}^2 n\, R(\boldsymbol{n})\, n_z = 0$.

I conclude that damping may only occur for blue-detuned cavity modes, $\Delta_n > 0$, which agrees with the classical model from Sect. 2.1.3 illustrated in Fig. 2.3. Moreover, we find a similar parameter dependence as in the classical expression (2.35), which is was derived with less rigour from a slightly different set of assumptions. The slowing rate (2.105) is modulated by the z-dependence of the mode, but it does not flip sign and accelerate the particle for a given set of cavity parameters. It appears strongest neither at the nodes nor at the antinodes of each cavity mode, but rather in between, at the steepest points of the overlap $u_0^* u_n$. If we average over all z-positions we find that each cavity mode overlapping with the pump mode contributes a mean velocity damping rate of $\left|\overline{\beta}^{(n)}\right| \sim 8\omega_r \kappa_n \Delta_n \left|\widetilde{U}_{0n}\alpha\right|^2 / \left(\kappa_n^2 + \Delta_n^2\right)^2$. It is maximized for a detuning of $\Delta_n = \kappa_n/\sqrt{3}$.

2.2.3.3   Case Study: A Single Strongly Pumped Standing-Wave Mode

It is instructive to apply the results to the most elementary case of a PPP inside a single driven Fabry-Pérot standing-wave mode, as already discussed earlier and sketched in Fig. 2.1. If we set $u_0(z) = \cos kz$ we can compute the memory function explicitly,

$$
\begin{aligned}
G(z, m_P v) &= \frac{1}{2(\kappa + i\Delta)} + \frac{1}{4}\left[\frac{\exp(2ikz)}{\kappa + i(\Delta + 2kv)} + \frac{\exp(-2ikz)}{\kappa + i(\Delta - 2kv)}\right] \\
&= \frac{1}{2v} + \frac{v\cos 2kz + 2kv\sin 2kz}{2\left[v^2 + (2kv)^2\right]},
\end{aligned}
\tag{2.106}
$$

with the complex damping-detuning parameter $v = \kappa + i\Delta$. The non-conservative force term becomes

$$
\begin{aligned}
g_p^{(\text{dis})}(z, m_P v) = \hbar k \left|\widetilde{U}_0\alpha\right|^2 \Bigg[&\mathfrak{Im}\left\{\frac{1}{v} + \frac{v\cos 2kz + 2kv\sin 2kz}{v^2 + (2kv)^2}\right\}\sin 2kz \\
&+\mathfrak{Re}\left\{\frac{\sin 2kz}{v^2 + (2kv)^2} - 2kv\frac{v\cos 2kz + 2kv\sin 2kz}{\left[v^2 + (2kv)^2\right]^2}\right\}4\omega_r\cos 2kz\Bigg].
\end{aligned}
\tag{2.107}
$$

Once again, we may neglect the second line because of its higher-order dependence on the recoil frequency ω_r. Let us, for the moment, focus on the velocity dependence of the remaining term by averaging over the position in the standing wave,

$$
\overline{g_p^{(\text{dis})}(m_P v)} = \frac{-4\left|\widetilde{U}_0\alpha\right|^2 \omega_r \kappa \Delta}{\left|v^2 + (2kv)^2\right|^2}m_P v + \mathcal{O}\left(\omega_r^2\right).
\tag{2.108}
$$

I plot the velocity dependence for different positive detunings, which correspond to a net slowing effect, in Fig. 2.5. Given a fixed cavity-pump detuning $\Delta > 0$, we
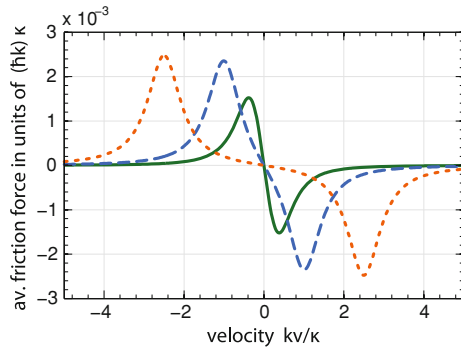
Fig. 2.5 Position-averaged friction force (2.108) of a pumped Fabry-Pérot cavity as a function of velocity for different cavity-pump detunings (adapted from [1]). It is positive on the *left* and negative on the *right* of $v = 0$, which means that it slows the particle. I use an effective coupling rate of $\left|\tilde{U}_0\alpha\right| = 0.1\kappa$. The *solid*, the *dashed*, and the *dotted lines* correspond to $\Delta = \kappa/\sqrt{3}$, 2κ and 5κ, respectively. Both velocity and force are plotted in natural cavity-related units of κ/k and $(\hbar k)\kappa$

observe that only a limited range of velocities is efficiently slowed. If we increase the detuning, the maximum of the friction force shifts to larger velocities, and faster particles are more efficiently slowed at the expense of not capturing already slow ones. In the limit of very large detunings $\Delta \gg \kappa$ the velocity capture range is determined by $kv \approx \Delta$. On the other hand, we observe the strongest damping effect (steepest slope) for small velocities at the detuning $\Delta = \kappa/\sqrt{3}$ (solid line). This is no surprise since we have found one section earlier that this detuning corresponds to an optimal friction coefficient $\overline{\beta}$.

The friction force is accompanied by momentum diffusion, which prevents the cavity from slowing a particle arbitrarily close to zero velocity,

$$D_{pp}^{(\text{dis})}(z, m_P v) = 2(\hbar k)^2 \left|\tilde{U}_0\alpha\right|^2 \mathfrak{Re}\left\{\frac{v\sin^2 2kz - 2kv\sin 2kz\cos 2kz}{v^2 + (2kv)^2}\right\},$$

(2.109)

$$\overline{D_{pp}^{(\text{dis})}(m_P v)} = \frac{(\hbar k)^2 \kappa \left|\tilde{U}_0\alpha\right|^2}{\left|v^2 + (2kv)^2\right|^2}\left[|v|^2 + (2kv)^2\right].$$

(2.110)

Although the position-averaged diffusion coefficient is strictly positive, this does not hold everywhere in the standing wave. The diffusion coefficient (2.109) is plotted as a function of z in Fig. 2.6 for various particle velocities. In the vicinity of the antinodes of the standing wave the diffusion coefficient assumes negative values at nonzero velocities. The positive regions clearly dominate for slow particles, $|kv| \lesssim \kappa$, where the position-averaged expression (2.110) assumes its maximum. Moreover, the positive and negative parts nearly compensate for faster particles (solid line).
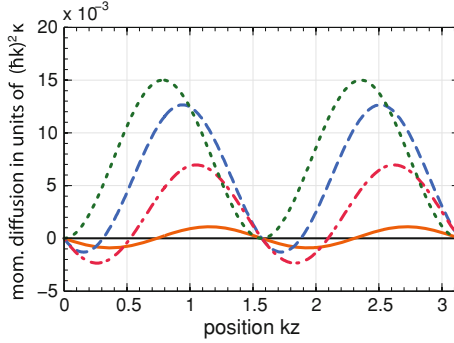
Fig. 2.6 Momentum diffusion coefficient (2.109) of a pumped Fabry-Pérot cavity as a function of position for different particle velocities (adapted from [1]). We use the effective coupling rate $\left|\widetilde{U}_0\alpha\right| = 0.1\kappa$ and the detuning $\Delta = \kappa/\sqrt{3}$. The *solid, dashed, dash-dotted*, and *dotted line* correspond to $kv = 5\kappa, \kappa, 0.5\kappa$, and 0, respectively. The diffusion coefficient and the position are expressed in cavity-related units of $(\hbar k)^2 \kappa$ and $1/k$

Anyway, the overall momentum diffusion effect vanishes in this case, because the cavity dynamics can no more keep up with the moving particle.

Completely positive Lindblad-type master equations must always yield positive semidefinite diffusion matrices $D_{jk}(z, p)$. In the present case, we have a vanishing position diffusion, $D_{zz}^{(\text{dis})} = 0$, and a non-diagonal element given by

$$D_{zp}^{(\text{dis})}(z, m_P v) = 2\hbar\omega_r \left|\widetilde{U}_0\alpha\right|^2 \mathfrak{Re}\left\{ \frac{4vkv\cos 2kz + \left[(2kv)^2 - v^2\right]\sin 2kz}{\left[v^2 + (2kv)^2\right]^2} \right\} \sin 2kz.$$
(2.111)

The resulting determinant is negative and the diffusion matrix is indefinite. This shows that the underlying master equation (2.87) is non-Markovian and cannot be cast into the completely positive Lindblad form. I attribute this to the memory effect of the cavity [60–62]. Its field does not adjust to the change in particle position instantaneously, but it reacts retardedly to the trajectory that is accumulated over the cavity lifetime $1/\kappa$. The negativity in the diffusion matrix is negligible in most practical cases when the cavity-induced slowing of large polarizable particles is concerned. The diffusion effect hardly affects the motional state of fast particles, which are far above the quantum limit of motion, as I will discuss in the following.

The whole cavity-induced damping-diffusion process can be understood as a random walk induced by the recoil related to the coherent scattering of pump photons between the two running-wave components of the standing-wave cavity mode. A moving particle emits Doppler-shifted light which is blue-detuned in the direction of motion and red-detuned in the opposite direction. By detuning the pump laser to the red side of the cavity resonance, we enhance the coherent scattering of photons into the direction of motion, thereby gradually taking away kinetic energy over many random walk cycles. It is then intuitively clear that the cavity-induced slowing

effect cannot decrease the kinetic energy of a particle further than the so-called recoil limit $\hbar\omega_r$. The accompanying momentum diffusion in units of $\hbar k$ simply cannot be overcome.

Is it then, at least in principle, possible to reach the recoil limit after a sufficiently long waiting time? Let me answer this question by estimating the final kinetic energy that can be obtained in the limit of $t \to \infty$. For this purpose consider again the time evolution equation (2.93) of the second moment in momentum, and ignore the z-modulation by averaging both the force and the diffusion term over the standing-wave profile. This cancels the conservative dipole force and leaves us with the dissipative terms (in the absence of absorption and Rayleigh scattering). Given the above expressions (2.108) and (2.110) in the limit of small particle velocities, $|kv| \ll \kappa$, we find that the average kinetic energy has a fixed point at the value[29]

$$\left\langle \frac{p^2}{2m_P} \right\rangle_\infty = -\frac{p \, \overline{D_{pp}^{(\mathrm{dis})}(p)}}{4m_P \, g_p^{(\mathrm{dis})}(p)} \approx \frac{\hbar}{8}\left(\Delta + \frac{\kappa^2}{\Delta}\right). \tag{2.112}$$

Ensembles of initially faster particles are eventually slowed down towards this limiting mean kinetic energy value. It depends on the cavity reaction time scale, and it reads as $\hbar\kappa/2\sqrt{3}$ in the case of the optimal detuning $\Delta = \kappa/\sqrt{3}$. Note that this limit is considerably higher than the fundamental recoil limit since $\omega_r \ll \kappa$. It illustrates that the cavity-induced slowing effect is in practice already limited by the finite cavity lifetime and the associated energy uncertainty. In the presence of absorption and Rayleigh scattering we must take the respective diffusion term (2.102) into account, which leads to the increased slowing limit

$$\left\langle \frac{p^2}{2m_P} \right\rangle_\infty \approx \frac{\hbar}{8}\left[\Delta + \frac{\kappa^2}{\Delta} + \frac{(\kappa^2 + \Delta^2)^2}{2\widetilde{U}_0^2 \kappa \Delta}\left(\gamma_{\mathrm{abs}} + \frac{7}{5}\gamma_{\mathrm{sca}}\right)\right]. \tag{2.113}$$

Concerning the interplay between friction and diffusion, I conclude: While the friction force determines the rate at which the kinetic energy of the particle is gradually dissipated through the cavity over many lifetime cycles of its field, the overall diffusion term sets the kinetic energy of the limiting velocity, which cannot be undercut in the present slowing scheme. Current sources for molecules and nanoparticles, which are used in matter-wave interferometry, are typically far above this limit. Assuming a cavity linewidth of $\kappa \sim 1$ MHz, the cavity-slowing limit corresponds to motional temperatures of the order of microkelvins.

---

[29] The expression (2.112) ceases to be valid for large velocities and at $\Delta = 0$, where the first-order friction term (2.108) vanishes.

2.2.3.4 Multimode Enhancement in Degenerate Resonator Configurations

Having studied the generic dissipation effect in the instructive case of a single Fabry-Pérot cavity mode, I now turn to a more practical multimode configuration, as sketched in Fig. 2.4. Each of the $M > 1$ empty cavity modes represents a dissipation channel which adds to the overall friction effect along the z-axis of the cavity. The strong pump mode is directed along the y-direction and should overlap with the cavity volume as much as possible to maximize the effective interaction region for each passing particle.

An experimental realization may be feasible in a setup where a large manifold of degenerate modes can be created in a confocal resonator configuration with two circularly symmetric curved mirrors. If the distance d between the mirrors is exactly the same as their radii of curvature, then, in principle, the resonator will support an almost infinite spectrum of higher-order transverse modes that share the same resonance frequency with a given fundamental standing-wave mode. These higher-order modes exhibit a larger effective mode waist, and the mode spectrum is in practice limited to a finite number M due to the finite aperture of real-life mirrors. In addition, if the setup is not precisely confocal, the contribution of higher-order modes to the friction force will decrease with shifting resonance frequency.

The controlled optical driving of one of the degenerate modes would require good mode matching, and it would lead to strong conservative dipole forces modulating the motion of particles along the standing wave. Both the mode matching and the dipole force can be avoided by shining a broad running-wave laser mode perpendicular to the cavity axis. It acts as an optical pump mode where it overlaps with the cavity modes, but it does not induce any significant dipole force along the cavity axis. Moreover, the absorption-induced momentum diffusion along the z-axis is also suppressed. This perpendicular pump configuration comes at the price of less available pump power. It could be enhanced by means of another cavity, of course.

In the following I will discuss the enhancement of the cavity-induced friction by the number M of accessible cavity modes. Once again, we restrict our view to the z-motion along the cavity axis, omitting any influence on the transverse motion of the particle. The resulting friction and diffusion terms still depend on the off-axis xy-coordinates of the particle, and we can average them over the trajectory of a particle traversing the cavity for an estimate of their mean effects.[30]

The modes of a confocal standing-wave resonator [28, 63–65] are characterized by one longitudinal mode index $n \in \mathbb{N}$ and two transverse mode indices $m, \ell \in \mathbb{N}_0$. From the boundary conditions at the curved mirror surfaces follow the respective resonance frequencies [65]

$$\omega_{n,m,\ell} = \frac{\pi c}{d} \left(n + m + \frac{\ell + 1}{2} \right), \tag{2.114}$$

---

[30] This corresponds to the experimental situation when a dilute beam of molecules or nanoparticles crosses the cavity, such that there is on average only one particle inside the cavity at a given time.

with d the mirror distance (and radius of curvature). A given fundamental mode $(n_0, 0, 0)$ of wavelength $\lambda = 2\pi/k$ shares the same resonance frequency with a huge manifold of transverse modes $(n < n_0, m, \ell)$, since $n_0 = 2d/\lambda$ is typically a large number. We can assign the effective waist parameter $w_{n,m,\ell} = w_0\sqrt{2m + \ell + 1}$ to each higher-order transverse mode [64, 65]; it describes the growing mode volume with respect to the fundamental mode of waist $w_0 = \sqrt{d\lambda/2\pi}$. If the waist is aperture-limited by $w_{n,m,\ell} \lesssim aw_0$, then both $2m$ and $\ell + 1$ are restricted to values less or equal to a^2, which leads to a total number of supported modes $M \lesssim a^4/2$. (The quantity a measures the aperture in units of w_0.)

The field distribution of each mode can be approximated by Laguerre-Gaussian functions[31] in the case of large-aperture mirrors [64], $a^2 \gg 1$. We obtain the explicit form of the three-dimensional mode function [65] by assuming linear polarization and omitting any off-axis corrections to the field polarization due to the transverse mode profile (see Appendix A.2 for the specific case of a Gaussian mode, $m = \ell = 0$). In cylindrical coordinates the full three-dimensional mode functions $\boldsymbol{u}_{n,m,\ell}(\boldsymbol{r}) = \boldsymbol{\epsilon} f_{m,\ell}(r, \phi, z) u_{n,m,\ell}(r, z)$ factorize into the on-axis standing-wave mode functions $u_{n,m,\ell}$, the Laguerre-Gaussian transverse mode profiles $f_{m,\ell}$, and a fixed polarization vector $\boldsymbol{\epsilon}$,

$$u_{n,m,\ell}(r, z) = \begin{Bmatrix} \cos \\ \sin \end{Bmatrix} \left[kz \left(1 + \frac{4r^2}{d^2\xi^2(z)} \right) - (2m + \ell + 1)\, \Phi(z) \right] \forall \begin{Bmatrix} n \text{ odd} \\ n \text{ even} \end{Bmatrix},$$
(2.115)

$$f_{m,\ell}(r, \phi, z) = \frac{\cos(\ell\phi)}{\xi(z)} \left(\frac{\sqrt{2}r}{w_0\xi(z)} \right)^\ell L_m^\ell \left(\frac{2r^2}{w_0^2\xi^2(z)} \right) \exp \left(\frac{-r^2}{w_0^2\xi^2(z)} \right). \quad (2.116)$$

Here, L_m^ℓ denotes the associated Laguerre polynomial [43], $\xi(z) = \sqrt{1 + 4z^2/d^2}$, and $\Phi(z) = \arctan(2z/d)$. We obtain a simple expression for the mode volume in the case of large apertures,

$$V_{n,m,\ell} = \frac{\pi}{8} w_0^2 d \,(1 + \delta_{\ell 0}) \frac{(\ell + m)!}{m!}, \quad (2.117)$$

if we approximate the on-axis function in the volume integral by an unmodified standing wave, $\int_{-d/2}^{d/2} dz \, u_{n,m,\ell}^2(r, z) \approx d/2$.

I now assess the contribution of each mode to the overall slowing effect in terms of its friction coefficient (2.105). To keep things simple, I assume that all contributing modes share the same linewidth κ and the optimal detuning $\Delta = \kappa/\sqrt{3}$, and I confine the analysis to the center of the cavity, $|z| \ll d$, where $\xi(z) \approx 1$. Moreover, we can safely omit the z-derivative of the orthogonally oriented pump mode. This leaves us with the estimate for the friction coefficient,

---

[31] Laguerre-Gaussian modes can only be used if the mirror system exhibits a cylindrical symmetry. This symmetry may be violated in applications with birefringent mirrors. In this case one must use the rectangular Hermite-Gaussian modes instead [64], which yield similar results as presented here.
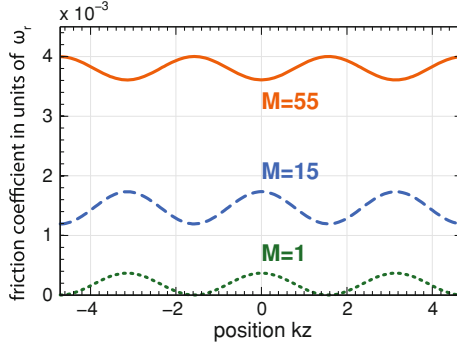
Fig. 2.7 Modulus of the overall friction coefficient of M confocal cavity modes in units of the recoil frequency and as a function of the on-axis position kz (reevaluated from [1]). The cavity mirrors are $d = 10$ mm apart. The *dotted line* represents the friction coefficient of the fundamental Gaussian mode $(20000, 0, 0)$ of wavelength $\lambda = 2\pi/k = 1\,\mu$m and waist $w_0 = 40\,\mu$m. It is pumped by a Gaussian wave of the same waist running along the y-axis. I assume an effective coupling of $|U_0\alpha| = 0.1\kappa$ between both modes, and a detuning of $\Delta = \kappa/\sqrt{3}$. The contributions (2.118) of the 14 and 54 closest degenerate transverse modes are added to the fundamental mode for the dashed and the *solid lines*, respectively. In all cases, the off-axis coordinates x and y are averaged over a *circle* of radius $5w_0$.

$$
\beta^{(n,m,\ell)}(r, \phi, z) \approx -\frac{3\sqrt{3}m!\omega_r\,|U_0\alpha|^2}{(\ell+m)!\,(1+\delta_{\ell 0})\,\kappa^2}\,\left|u_0(r, \phi, z)\,f_{m,\ell}(r, \phi, 0)\right|^2
$$
$$
\times \left(1 + \frac{4r^2}{d^2} - \frac{4m+2\ell+2}{kd}\right)^2
$$
$$
\times \begin{Bmatrix} \sin^2 \\ \cos^2 \end{Bmatrix} \left[kz\left(1 + \frac{4r^2}{d^2} - \frac{4m+2\ell+2}{kd}\right)\right]\;\forall\;\begin{Bmatrix} n\ \text{odd} \\ n\ \text{even} \end{Bmatrix},
$$

$$\tag{2.118}$$

to first order in the recoil frequency ω_r and in the parameters[32] z/d and $1/kd$. Here, the term U_0 is defined as the coupling rate between the pump mode and the fundamental Gaussian cavity mode $(n_0, 0, 0)$. The pump mode shall be given by a Gaussian running wave of the same waist w_0, $|u_0(r, \phi, z)| = \exp\left[-\left(z^2 + r^2\cos^2\phi\right)/w_0^2\right]$.

The total friction coefficient of the cavity is the sum over the terms (2.118) of all degenerate modes that are accessible by the pump laser. The overall cavity-induced slowing rate is amplified by the number of transverse modes supported by the cavity. This is demonstrated in Fig. 2.7 for a set of exemplary parameters. There, the friction rate is averaged over the off-axis coordinates[33] and plotted as a function of z close to the center of the resonator. The plot compares the contribution of the fundamental

---

[32] Second order terms of the form z^2/d^2, $1/k^2d^2$ and z/kd^2 are dropped. The inverse tangent is linearized as $\arctan(2z/d) \approx 2z/d$.

[33] The average friction rate depends on the size of the averaging area. A larger area covers more space outside the cavity where the friction effect is zero. Nevertheless, the average value is a meaningful
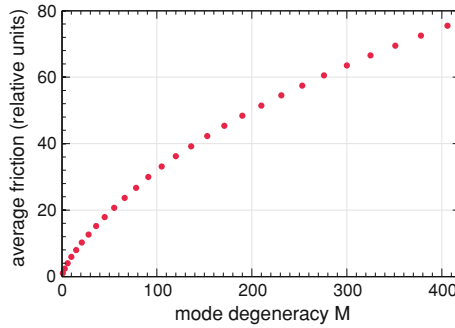
Fig. 2.8 Position-averaged friction coefficient of a confocal resonator as a function of the number *M* of degenerate modes that are taken into account. All the settings of Fig. 2.7 are used, and the results are additionally averaged over the range of *z*-coordinates depicted there. The data points are given in proportion to the average friction rate of the fundamental mode (mean value of the *dotted curve* in Fig. 2.7).

mode (dotted curve) to the collective friction rate of $M = 15$ (dashed) and $M = 55$ (solid) degenerate modes. Notice that, besides the overall multimode enhancement, the standing-wave modulation of the friction rate is also reduced. This is due to the equal contribution of both sine and cosine standing-wave modes in the confocal configuration. Hence, there is a nonzero slowing effect everywhere on the standing-wave axis.

In a real-life experiment the number of supported higher-order modes can be much higher, depending on the quality and aperture of the cavity mirrors. In Fig. 2.8 I plot the position-averaged friction rate of the resonator versus the number M of degenerate modes that were taken into account in the computation. The plotted data are normalized to the single-mode value. The rightmost point corresponds to $M = 406$ indicating an amplification of the single-mode friction effect by almost two orders of magnitude. The increase per mode gets diminished with growing mode volume due to the decreased overlap with the pump mode.

Let me close this section on the cavity-induced slowing of a PPP in the weak coupling regime with a few remarks. I have developed a rigorous quantum description of the dissipative motion of a particle in the presence of pump field and cavity by means of an effective (non-Markovian) master equation. It has led us to the understanding of the emergent friction and diffusion effects using a semiclassical phase-space approach. After studying the basic phenomena in an idealized single-mode configuration, I have provided a detailed assessment of the multimode case. At this point we should note that not only the friction force is enhanced by the presence of many modes, but also the accompanying momentum diffusion effect. While the former determines the effective rate at which the motion of the particle is damped,

---

(Footnote 33 continued)

quantity to assess the net slowing of particles that are trapped in or passing the chosen region in a given amount of time.

the latter raises the ultimate cooling limit. In other words, more modes imply a larger limiting kinetic energy value, down to which the particle can be damped by the cavity. Absorption and Rayleigh scattering contribute to this limit as well.

In many potential laboratory applications with molecules and clusters, one must often deal with particle ensembles whose initial temperature is far above this limit. In practice, it would be much more important to boost the effective damping rate from the unsuitably low values, as implied by the parameters listed in Table 2.1, to a feasible regime. This requires one to leave the weak coupling regime by increasing the pump field strength or by using even larger particles, as I will discuss in the next section. Another option is to increase the number of particles that interact with the cavity at the same time. In Appendix A.4 I show how to generalize our quantum treatment and the effective master equation to $N > 1$ particles in M driven or empty modes. There, however, the validity of the resulting friction and diffusion terms is restricted to an even more rigid weak-coupling limit. This is because the individual field fluctuations induced by each particle may add up. By breaking the weak-coupling limit with many particles one may benefit from strong cavity-mediated inter-particle correlations and from collective phenomena such as self-organisation [66, 67].

2.3 Mechanics of Spherical Particles in Coherent Light Fields

So far I have discussed the (off-resonant) light-matter interaction, and its mechanical action on matter-waves, in terms of point-like particles characterized by a scalar complex dipole polarizability χ. Whereas this is a good approximation for many molecules and clusters, which are by orders of magnitude smaller than the wavelength of the light they interact with, it ceases to be valid for nano- and microparticles of the same size as the wavelength or larger. The light scattering properties get more complex as higher-order multipole components take over, and a rigorous quantum description of both the light and the matter degrees of freedom is a difficult task due to several reasons:

- The quantization of the center-of-mass motion of the particle depends on explicit expressions for the force and the optical potential induced by the light field. However, we will see below that the force on extended particles cannot be reduced to a simple analytical expression anymore, but must be evaluated numerically in practice. Moreover, the result contains both the conservative light force and the radiation pressure force due to light absorption and Rayleigh scattering. Consequently, the optical potential cannot be directly deduced. We can avoid these difficulties in the effectively one-dimensional situation of matter-wave diffraction at optical standing-wave gratings in Sect. 2.3.2.
- If a large particle couples strongly to a high-finesse cavity field, it may change the spatial mode structure of the resonator. This is intuitively clear since the particle becomes a semitransparent mirror for the cavity field if it is large enough. Whereas one may benefit from the strong coupling when trying to observe cavity-induced

slowing of large particles, the theoretical modelling requires a proper treatment of the modified boundary conditions. I will present an approximate solution when I discuss the classical slowing of spherical particles in Sect. 2.3.3.

- A rigorous quantum description of the dynamics of both the light field and the particle requires an elaborate model for light scattering at extended material objects. This is a matter of current research [68], and it has gained interest with the upcoming of proposals to observe the ground-state motion of optically trapped microspheres [69, 70]. One possible model treats the extended object as an assembly of point-like scatterers at which single photons can scatter along multiple paths [68]. The resulting master equation gives proper account to the scattering-induced decoherence and diffusion effects, provided that the local fields are correctly described for each scatterer. Another possibility is to model the particle as a dielectric medium, which then requires the canonical quantization of the macroscopic field inside this medium [71]. However, this approach requires one to determine the precise momentum carried by the radiation field inside the dielectric medium when trying to assess the force density acting on the material—an old and controversial issue [6, 72].

- Apart from the center-of-mass effect, an extended dielectric object may also experience elastic stress due to light-induced bending and shearing forces. This may, in turn, deform the particle and modify its response to the light field depending on its stiffness properties [73]. Here, I avoid this additional complication by assuming rigid atomic clusters. Nevertheless, we must keep in mind that this might be an issue when dealing with hot or fluid particles, such as nanodroplets.

In this thesis I focus on generally hot and fast ensembles of particles far above the quantum limit of motion, which interact with strong coherent light fields. In the effective description of such particles, we may therefore avoid many of the aforementioned difficulties by assuming a stationary mode configuration and ignoring the full quantum nature of the photon field dynamics.

Moreover, I restrict the considerations to homogeneous dielectric spheres,[34] which is a good representation of many heavy clusters consisting of $N \gg 1$ atoms [31]. We can employ the Mie theory of light scattering at spherical objects [2, 3, 8, 74] to understand the light-matter interaction, as outlined in Appendix A.6. The idea is to start with a given light field E_0 in the absence of the sphere, and to expand it in the basis of spherical vector harmonics, that is, multipole components which respect the spherical symmetry of the problem. The origin of the coordinate system must be shifted to the center of the sphere r_0, accordingly. The spherical wave expansion is outlined in Appendix A.5.

Putting the sphere into the game introduces a different field E_{int} inside the dielectric medium, and it modifies the external field by adding a scattering component, $E_0 \rightarrow E_{\text{ext}} = E_0 + E_{\text{sca}}$. The expansion coefficients of the new field components

---

[34] Nonspherical particles scatter light in different patterns, that is, the multipole composition of the scattered field deviates from the spherical case. The basic consequences of leaving the subwavelength size regime are similar to the spherical case, with the additional complication of coupling to the rotation of the object.

E_{int} and E_{sca} are obtained from the boundary conditions at the sphere surface. I have done this explicitly for plane running and standing waves, and for Gaussian modes in Appendix A.6. In the following, let me discuss the consequences for the mechanical action of light onto the particle.

2.3.1 Light Extinction and Light-Induced Forces

Mie theory provides us with the field configuration when a dielectric sphere of relative permittivity ε is placed into an electromagnetic field $\{E_0, H_0\}$ at the position r_0. Following Appendix A.6, the field outside of the sphere is then complemented by the scattering component

$$E_{\mathrm{sca}} = \sum_{\ell=1}^{\infty} \sum_{m=-\ell}^{\ell} \left[\alpha_\ell C_{\ell,m}^{(\mathrm{M})} h_\ell\left(kr\right) X_{\ell,m}\left(\theta, \phi\right) + \frac{\beta_\ell C_{\ell,m}^{(\mathrm{E})}}{k} \nabla \times h_\ell\left(kr\right) X_{\ell,m}\left(\theta, \phi\right) \right],$$

(2.119)

with $h_\ell X_{\ell,m}$ and $\nabla \times X_{\ell,m} h_\ell$ the partial-wave multipole solutions (see Appendix A.5). The terms $C_{\ell,m}^{(\mathrm{M,E})}$ are the multipole expansion coefficients of the original field E_0, which depend on the position r_0 of the sphere. The coordinates $r = (r, \theta, \phi)$ are defined relative to r_0. The scattered field differs from the original field mainly by the scattering coefficients α_ℓ and β_ℓ. They read as

$$\alpha_\ell = \frac{j_\ell\left(\sqrt{\varepsilon}kR\right) \partial_R \left[Rj_\ell\left(kR\right)\right] - j_\ell\left(kR\right) \partial_R \left[Rj_\ell\left(\sqrt{\varepsilon}kR\right)\right]}{h_\ell\left(kR\right) \partial_R \left[Rj_\ell\left(\sqrt{\varepsilon}kR\right)\right] - j_\ell\left(\sqrt{\varepsilon}kR\right) \partial_R \left[Rh_\ell\left(kR\right)\right]},$$

(2.120)

$$\beta_\ell = \frac{\varepsilon j_\ell\left(\sqrt{\varepsilon}kR\right) \partial_R \left[Rj_\ell\left(kR\right)\right] - j_\ell\left(kR\right) \partial_R \left[Rj_\ell\left(\sqrt{\varepsilon}kR\right)\right]}{h_\ell\left(kR\right) \partial_R \left[Rj_\ell\left(\sqrt{\varepsilon}kR\right)\right] - \varepsilon j_\ell\left(\sqrt{\varepsilon}kR\right) \partial_R \left[Rh_\ell\left(kR\right)\right]},$$

(2.121)

for a dielectric sphere of radius R, as given in the Appendix. (There I also present the case of a hollow sphere, which leads to more cumbersome expressions.) Note that the coefficients are independent of the chosen mode structure of the light field, as given by the $C_{\ell,m}^{(\mathrm{M,E})}$. They are the same in a running wave as in a standing wave. In the case of a point-like particle, $kR \ll 1$, we find that the lowest-order contribution is given by[35] $\beta_1 \approx 2i (kR)^3 (\varepsilon - 1)/3(\varepsilon + 2)$. All other coefficients are of higher order in kR and thus negligible. One can convince oneself, using the identities and relations of Appendix A.5, that this yields the scattering field of the induced dipole $\chi E_0 (r = 0)$, with the complex polarizability of a subwavelength sphere [31],

$$\chi \approx 4\pi\varepsilon_0 R^3 \frac{\varepsilon - 1}{\varepsilon + 2} \quad \text{if } kR \ll 1.$$

(2.122)

---

[35] I use that the spherical Bessel functions can be approximated by $j_\ell(x) \approx x^\ell / [1 \cdot 3 \cdot \ldots \cdot (2\ell + 1)]$ and $y_\ell(x) \approx - [1 \cdot 3 \cdot \ldots \cdot (2\ell - 1)]/x^{\ell+1}$ to lowest order in $x \ll 1$, while the spherical Hankel function becomes $h_\ell(x) \approx iy_\ell(x)$.

Hence, the point-particle limit is properly reproduced by the Mie expansion. Having the Mie expression (2.119) at hand, we are now able to study the light extinction properties of the sphere, as well as the light-induced force acting on it. I will focus on standing-wave light modes, as opposed to running waves, since they are the basis of the optical diffraction gratings and the two-mirror cavities studied here.

2.3.1.1 The Poynting Vector and the Extinction Power of the Sphere

Scattering and absorption of light by finite geometries can be treated formally by means of the Poynting vector $S = \Re\{E\} \times \Re\{H\}$. It has the dimension W/m^2 and describes the net energy flux per unit surface $|S|$ into the direction $S/|S|$ in vacuum[36] [7, 8, 75]. That is, the time-averaged field energy flowing through a small surface element $dA = r^2 d\Omega$ at position r into direction n per unit time is given by $P_n(r) = \langle n \cdot S \rangle_t = -r^2 d\Omega \Re\{E(r) \cdot [n \times H^*(r)]\}/2$. From this it is intuitively clear how to obtain the total field energy per time scattered or absorbed by the sphere.

In order to assess the scattered power (2.123) we must take the outward-directed Poynting vector corresponding to the scattering field E_{sca} and integrate it over the sphere surface [3, 8]. The absorbed power (2.124) is given by the net energy flux into the sphere, that is, by the integrated inward-directed Poynting vector corresponding to the total external field $E_{\text{ext}} = E_0 + E_{\text{sca}}$. The extinction power (2.125) is defined as the sum of both contributions.

$$P_{\text{sca}} = -\frac{R^2}{2} \int d\Omega \, \Re\left\{ E_{\text{sca}}(Rn) \cdot [n \times H^*_{\text{sca}}(Rn)] \right\} \tag{2.123}$$

$$P_{\text{abs}} = \frac{R^2}{2} \int d\Omega \, \Re\left\{ E_{\text{ext}}(Rn) \cdot [n \times H^*_{\text{ext}}(Rn)] \right\} \tag{2.124}$$

$$P_{\text{ext}} = \frac{R^2}{2} \int d\Omega \, \Re\left\{ E_0(Rn) \cdot [n \times H^*_{\text{sca}}(Rn)] + E_{\text{sca}}(Rn) \cdot [n \times H^*_0(Rn)] \right\} \tag{2.125}$$

A straightforward calculation using the orthogonality properties of the multipole expansion given in Appendix A.5 leads to the explicit forms

$$P_{\text{sca}} = \frac{c\varepsilon_0}{2k^2} \sum_{\ell,m} \left[\left| \alpha_\ell C^{(\text{M})}_{\ell,m} \right|^2 + \left| \beta_\ell C^{(\text{E})}_{\ell,m} \right|^2 \right],$$

$$P_{\text{ext}} = -\frac{c\varepsilon_0}{2k^2} \sum_{\ell,m} \left[\Re\{\alpha_\ell\} \left| C^{(\text{M})}_{\ell,m} \right|^2 + \Re\{\beta_\ell\} \left| C^{(\text{E})}_{\ell,m} \right|^2 \right], \tag{2.126}$$

---

[36] All the calculations can be done in the vacuum surrounding the sphere, thus avoiding the discussion [72] which form of the Poynting vector to choose inside the medium.

and $P_{\mathrm{abs}} = P_{\mathrm{ext}} - P_{\mathrm{sca}}$. If the medium is non-absorptive, that is, if the refractive index $\sqrt{\varepsilon}$ is real, then one can easily check that $P_{\mathrm{abs}} = 0$ and $|\alpha_\ell|^2 = -\mathfrak{Re}\{\alpha_\ell\}$, $|\beta_\ell|^2 = -\mathfrak{Re}\{\beta_\ell\}$. We observe that the extinction power is a sum over the independent contributions of electric (E) and magnetic (M) multipole components.

The expressions simplify further in the case of a cosine-type standing wave,

$$P_{\mathrm{sca,ext}}(z_0) = \frac{\pi I_0}{k^2}\left[\Pi_{\mathrm{sca,ext}}^{(+)} + \Pi_{\mathrm{sca,ext}}^{(-)}\cos 2kz_0\right], \qquad (2.127)$$

with z_0 the z-coordinate of the sphere center and $I_0 = c\varepsilon_0 |E_0|^2 /2$ the field intensity at the antinodes. The offset factors $(+)$ and the modulation factors $(-)$ read as

$$\Pi_{\mathrm{sca}}^{(\pm)} = \sum_\ell (2\ell+1)(\pm)^\ell \left[|\alpha_\ell|^2 \pm |\beta_\ell|^2\right],$$

$$\Pi_{\mathrm{ext}}^{(\pm)} = -\sum_\ell (2\ell+1)(\pm)^\ell \left[\mathfrak{Re}\{\alpha_\ell\} \pm \mathfrak{Re}\{\beta_\ell\}\right]. \qquad (2.128)$$

It is once again easy to verify that the dipolar values (2.7) and (2.8) for the absorbed and scattered power are assumed in the limit $kR \ll 1$, with the polarizability given by (2.122).

Similar expressions hold in the case of a Gaussian standing-wave mode. The multipole expansion in (2.126) then includes corrections due to the finite Gaussian waist w, as listed in Appendix A.5. In many practical situations, however, one is only interested in the standing-wave modulation of the scattering and absorption power as a function of the on-axis coordinate z_0. If we neglect corrections of the order of $1/kw$, then formula (2.127) applies also to the Gaussian mode; we must simply append the Gaussian mode profile to the field intensity, $I_0 \to I(x_0, y_0) = c\varepsilon_0 |E_0|^2 \exp\left[-2\left(x_0^2 + y_0^2\right)/w^2\right]/2$.

Figure 2.9 illustrates the standing-wave light extinction as a function of the radius for gold spheres at the UV wavelength $\lambda = 157\,\mathrm{nm}$ ($\varepsilon_{\mathrm{Au}} = 0.9 + 3.2i$ is taken from [29]). The solid line on the left panel represents the offset factor $\Pi_{\mathrm{ext}}^{(+)}$, that is, the z_0-averaged extinction power (2.127) divided by $\pi I_0/k^2$, as a function of the radius on a logarithmic scale. The dashed and the dotted line represent the offset factors of the scattered power and the absorbed power, respectively. The mean absorption power grows like the volume, in proportion to $(kR)^3$, when the field fully penetrates the sphere in the subwavelength regime, $kR < 1$. The Rayleigh scattering power, which scales like $(kR)^6$, is strongly suppressed in this regime. The scattering contribution slowly takes over for larger radii, where the total extinction scales like the sphere surface, in proportion to $(kR)^2$. Absorption and reflection prevent the light field from entering deeply into the large sphere. The varying power laws in kR are nicely visible in the double-logarithmic plot.

The right panel in Fig. 2.9 shows the contrast of the z_0-modulation, $\Pi^{(-)}/\Pi^{(+)}$, for the extinction power (solid), the scattering power (dashed), and the absorption power (dotted). It starts at unity in the point-particle limit, decreases to smaller values
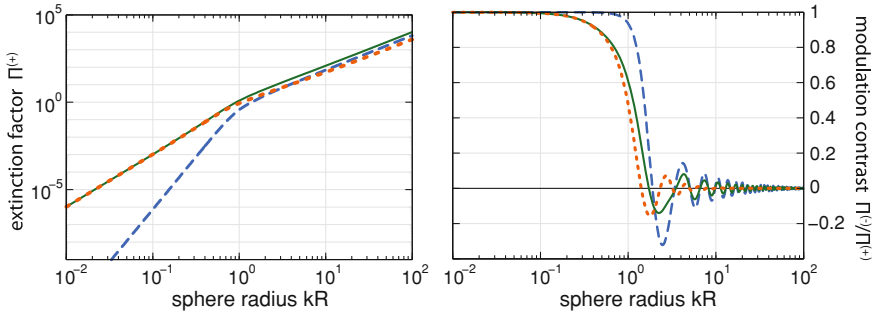
Fig. 2.9 Mean value (*left*) and modulation (*right*) of the UV light extinction power of gold spheres as a function of the sphere radius. We use the bulk permittivity of gold [29], $\varepsilon_{Au} = 0.9 + 3.2i$ at $\lambda = 157$ nm. The *solid*, the *dashed*, and the *dotted lines* correspond to the extinction, the scattering, and the absorption power, respectively. The mean value on the *left* diagram is plotted in dimensionless units $\pi I_0 / k^2$ relative to the field intensity I_0, as given by the $\Pi^{(+)}$-factors in (2.128). The modulation contrast on the *right* is given by the ratio of the modulation amplitude and the mean value

and oscillates finally between positive and negative values. We find that the standing-wave modulation is strongly suppressed once the particle extends over more than a single wavelength. Note that a negative value means that the sphere scatters more light when it is centered at a node of the standing wave. This can be explained by higher multipole (e.g. the quadrupole) components which are more dominantly addressed at the field nodes.
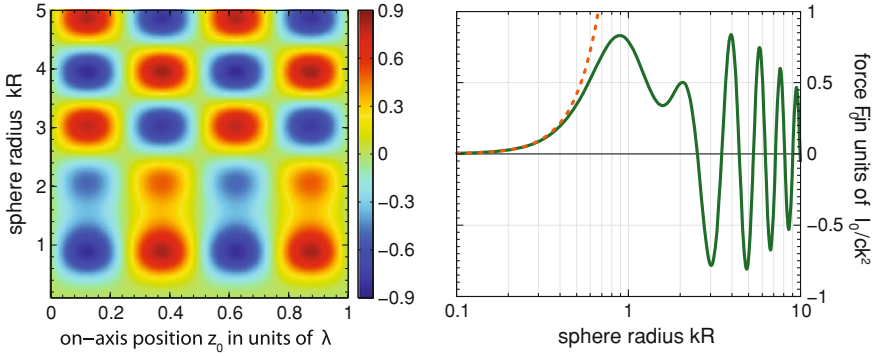
2.3.1.2 Maxwell Stress Tensor and Optical Forces

The light-induced forces acting on a dielectric are related to the Maxwell stress tensor

$$\mathsf{T} = \varepsilon_0 \left[\mathfrak{Re}\left\{ \boldsymbol{E} \right\} \circ \mathfrak{Re}\left\{ \boldsymbol{E} \right\} - \frac{\mathbb{I}}{2} \mathfrak{Re}\left\{ \boldsymbol{E} \right\} \cdot \mathfrak{Re}\left\{ \boldsymbol{E} \right\} \right]$$
$$+ \mu_0 \left[\mathfrak{Re}\left\{ \boldsymbol{H} \right\} \circ \mathfrak{Re}\left\{ \boldsymbol{H} \right\} - \frac{\mathbb{I}}{2} \mathfrak{Re}\left\{ \boldsymbol{H} \right\} \cdot \mathfrak{Re}\left\{ \boldsymbol{H} \right\} \right], \tag{2.129}$$

with $(\boldsymbol{a} \circ \boldsymbol{b})_{jk} = a_j b_k$ the dyadic product and $\mathbb{I}$ the three-dimensional identity matrix. In general, the change of the momentum carried by the field inside a finite volume of free space is given by the corresponding surface integral of the stress tensor [8, 75]. This implies that, if we take that the dielectric spheres to be rigid [73], the time-averaged force acting on the center of mass reads as

$$\boldsymbol{F} = \frac{R^2}{2} \int d\Omega \, \mathfrak{Re} \left\{ \varepsilon_0 \left[(\boldsymbol{n} \cdot \boldsymbol{E}_{\text{ext}}) \, \boldsymbol{E}_{\text{ext}}^* - \frac{\boldsymbol{n}}{2} |\boldsymbol{E}_{\text{ext}}|^2 \right] + \mu_0 \left[(\boldsymbol{n} \cdot \boldsymbol{H}_{\text{ext}}) \, \boldsymbol{H}_{\text{ext}}^* - \frac{\boldsymbol{n}}{2} |\boldsymbol{H}_{\text{ext}}|^2 \right] \right\}. \tag{2.130}$$

Fig. 2.10 On-axis force on finite-size gold spheres in a vacuum-UV standing-wave field ($\lambda = 157$ nm, $\varepsilon_{Au} = 0.9 + 3.2i$), as predicted by the Mie expression (2.130). The *left panel* is a density plot of the force versus the center position z_0 (in units of λ) and the normalized radius $kR = 2\pi R/\lambda$ of the sphere. The *right panel* depicts the maximum force with respect to z_0 as a function of the radius. The *solid line* represents the result of the full Mie calculation, whereas the *dotted line* corresponds to the point-particle approximation. The force data are plotted in natural units relative to the field intensity, I_0/ck^2

The external fields in the integral are evaluated on the sphere surface, $\boldsymbol{r} = R\boldsymbol{n}$. The force is always proportional to the intensity parameter $I_0 = c\varepsilon_0 |E_0|^2 /2$ of the input light mode $\boldsymbol{E}_0$.

In the idealized case of a plane standing or running wave the force must point into the z-direction, and it can only depend on the coordinate z_0 of the sphere. Transverse force components are excluded due to the symmetry under x_0- and y_0-translations. The left panel in Fig. 2.10 shows a density plot of the standing-wave force F_z on gold spheres as a function of z_0 and of the normalized sphere radius kR. I evaluated the integral (2.130) numerically, using the representation of the scattering field (2.119) and the expansion coefficients of a standing wave given in Appendix A.5. The force is given in proportion to the field intensity, that is, in units of I_0/ck^2. We observe that the symmetry of the standing wave sets the z_0-modulation of the force to be $F_z(z_0) = -F_0 \sin 2kz_0$, irrespective of the sphere size. In particular, the force is always zero at the nodes and antinodes of the field. At the same time, the radius R does affect the force amplitude F_0 significantly. The latter even flips its sign for $kR \gtrsim 2$, in clear contradiction to the behaviour of a polarizable point particle.

The disparate behaviour of point particles and extended spheres is more clearly seen on the right panel, where I have plotted the force amplitude $F_0 = F_z(-\lambda/8)$ versus the radius (solid line). I compare it to the maximum PPP force (dashed line), $F_{PPP} = 2\pi I_0 k R^3 \mathfrak{Re}\{(\varepsilon - 1)/(\varepsilon + 2)\}/c$, which would be obtained if the sphere were approximated by a point-like particle with the polarizability (2.122). This approximation ceases to be valid already for $kR \gtrsim 0.5$. From this point on the force does not grow with the sphere volume any longer. We observe quite a contrary behaviour; the force term oscillates between positive and negative values. In other words, the sphere may become an *effective low-field seeker*. An explanation for this
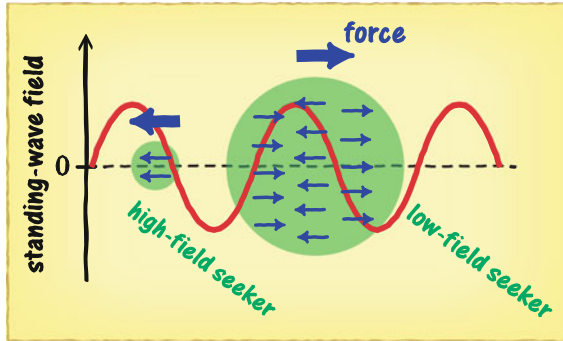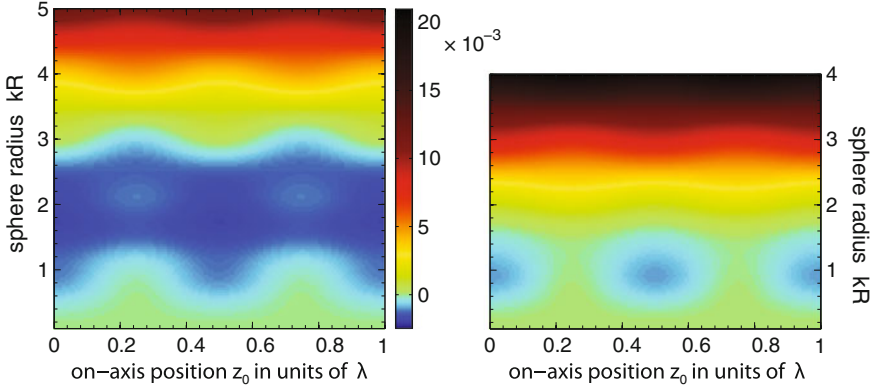
Fig. 2.11 Sketch of the optical forces on a small and a large dielectric sphere in a standing-wave field. Both sphere centers are between an antinode and a node of the field. The net force on the small sphere points towards the high field since most of its volume is subject to the same field polarization and dipole force. The large sphere experiences a net force towards the low field. Different parts of the sphere experience are subject to opposite field polarizations and are drawn to opposite directions

remarkable size effect is illustrated in Fig. 2.11 depicting a small and a large sphere placed in between a node and an antinode of the standing-wave field. Suppose that we decompose each sphere into small volume elements, and assume that the individual elements are subject to the local dipole force (We neglect both the modification of the local field and the absorption inside the sphere). We arrive at the total force by adding the individual contributions. This leads to a high-field seeking behaviour of the small sphere because all constituents are drawn to the same antinode of the field. The net force on the large sphere, on the other hand, points to the low field, because different parts are drawn to opposite directions.

Let me now turn to the more realistic case of a Gaussian standing-wave mode with finite waist w. Here we must distinguish between the force F_z along the standing-wave axis and the non-vanishing off-axis forces $F_{x,y}$. Considering the former, we should merely expect small corrections to the ideal standing-wave modulation studied before. This follows by comparing the multipole expansion of the ideal standing wave with the Gaussian one, as given in Appendix A.5. Corrections to the standing-wave modulation are of the order of the waist parameter $1/kw \ll 1$, and we may neglect them for most practical purposes.[37] In this case we may again use the standing-wave results after replacing the standing-wave intensity parameter I_0 by the local intensity $I(x_0, y_0)$ in the Gaussian mode.

The same argument does not apply to the off-axis transverse forces $F_{x,y}$ which are by themselves terms of the order of $1/kw$. A numerical evaluation of the transverse forces reveals some peculiar size effects which become evident when we compare the

---

[37] This argument holds as long as the sphere is not too far away from the focus of the Gaussian mode. The reason is that the representation of the Gaussian TEM_{00} mode given in Appendix A.2 ceases to be valid for far-off center coordinates $|r_0| \gg w$. This limit should hardly be of relevance in any practical implementation.

numerical results with the subwavelength approximation based on the polarizability expression (2.122),

$$\begin{pmatrix} F_x^{(\mathrm{PPP})}(\boldsymbol{r}_0) \\ F_y^{(\mathrm{PPP})}(\boldsymbol{r}_0) \end{pmatrix} = -\begin{pmatrix} x_0 \\ y_0 \end{pmatrix}\frac{4\pi R^3 I_0}{cw^2}\mathfrak{Re}\left\{\frac{\varepsilon - 1}{\varepsilon + 2}\right\}e^{-2(x_0^2+y_0^2)/w^2}\,(1 + \cos 2kz_0)$$

$$= -\frac{2F_{\mathrm{PPP}}}{kw^2}e^{-2(x_0^2+y_0^2)/w^2}\left[\begin{pmatrix} x_0 \\ y_0 \end{pmatrix} + \begin{pmatrix} x_0 \\ y_0 \end{pmatrix}\cos 2kz_0\right]. \qquad (2.131)$$

At first one might think that, if one took the average of the transverse force over one period of the standing wave, the point-particle approximation would be still valid for particles that are larger than the wavelength, and yet smaller than the waist. This would be a wrong assertion, as demonstrated in Fig. 2.12, once again for the exemplary case of gold spheres in vacuum-UV light. Here I plot the x-force (left) and the y-force (right) at $x_0 = y_0 = w/2$, as obtained from the full Mie calculation, versus the sphere radius R and the on-axis coordinate z_0. The forces are again plotted in units of I_0/ck^2. I have assumed a realistic waist of $w = 100\,\lambda$. Judging from an extensive numerical analysis and from the plotted data, I have found a similar functional dependence of the two components $F_{x,y}$ of the Mie force (2.130) on $\boldsymbol{r}_0$ as in the point-particle approximation,

$$\begin{pmatrix} F_x(\boldsymbol{r}_0) \\ F_y(\boldsymbol{r}_0) \end{pmatrix} = -\frac{2}{kw^2}e^{-2(x_0^2+y_0^2)/w^2}\left[\begin{pmatrix} x_0 F_x^{(+)} \\ y_0 F_y^{(+)} \end{pmatrix} + \begin{pmatrix} x_0 F_x^{(-)} \\ y_0 F_y^{(-)} \end{pmatrix}\cos 2kz_0\right]. \qquad (2.132)$$
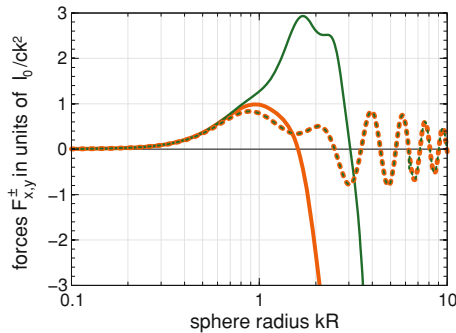
Fig. 2.13 Offset factors $F_{x,y}^{(+)}$ (*solid lines*) and modulation factors $F_{x,y}^{(-)}$ (*dotted lines*) of the transverse forces (2.132) as a function of the normalized radius kR of gold spheres in a Gaussian standing-wave mode ($\lambda = 157\,\text{nm}$, $\varepsilon_{\text{Au}} = 0.9 + 3.2i$). The data were computed with help of the Mie expression (2.130) and plotted in units of I_0/ck^2. The *dark green curves* correspond to the x-direction, which is also the main polarization direction of the electric field. The *light orange curves* represent the y-direction. The two modulation factors (*dashed*) are almost identical, except for small numerical uncertainties

Figure 2.12 shows that the force components differ significantly from a point-particle behaviour at sphere radii $kR \gtrsim 1$. At smaller radii, the average force is negative (i.e. pointing inwards the center of the Gaussian mode) and exhibits a pronounced standing-wave modulation. Then, however, the modulation dies off quickly, and we notice a non-recurring inversion of the sign once the sphere diameter approaches the wavelength, $kR \lesssim \pi$. The gold spheres turn into low-field seekers; they are effectively pushed away from the center of the Gaussian mode profile, although their radii are still much smaller than the mode waist. Moreover, we observe that the cylindrical symmetry breaks down, since the x- and the y-components are no longer the same.

We see this more clearly in Fig. 2.13, where the four terms $F_{x,y}^{(\pm)}$ extracted from a numerical evaluation of (2.132) are plotted as a function of R. The differences between the two transverse directions indicate the presence of non-conservative forces. If the two transverse components were identical, $F_x^{(\pm)} = F_y^{(\pm)}$, and if the modulation factors matched the on-axis force factor, $F^{(-)} = F_0$, then the force could be written as the gradient of the potential $V(\boldsymbol{r}_0) = -\exp\left[-2\left(x_0^2 + y_0^2\right)/w^2\right]$ $\left(F^{(+)} + F^{(-)} \cos 2kz_0\right)/2k$. Evidently, no such potential exists for (sufficiently large) gold spheres in the Gaussian mode. The non-conservativity is related to the radiation pressure induced by the absorption and free-space scattering of light, and it leads to notable asymmetries and a low-field seeking behaviour at large radii, as shown in the diagram.

One important practical consequence is the following: One cannot deduce the optical potential of wavelength-sized particles coupled to Gaussian modes from the electromagnetic force alone. We must find a different method to extract the position-dependent coupling energy between such a particle and a high-finesse cavity mode

in order to assess cavity-induced dissipation effects. I will deal with this issue in Sect. 2.3.3. Before that, let me briefly discuss the effect of optical standing-wave gratings on extended spherical particles.

2.3.2 Optical Standing-Wave Gratings

With the extensive discussion of Mie theory in the preceding section at hand, I will now generalize the model of optical standing-wave gratings developed in Sect. 2.1.4. There I discussed how a coherent standing-wave field can act as a diffraction grating for matter-wave states of polarizable point particles in the limit of short interaction times. Two separate processes can contribute to the diffraction effect: The periodic phase modulation of the matter-wave due to the action accumulated in the optical dipole potential and the amplitude modulation that occurs if the absorption of single photons depletes the matter-wave state.

In the following, I will generalize both effects to dielectric spheres of finite radius. We will see that the effective grating modulation becomes less effective with growing particle size. A more detailed analysis of the consequences for mater-wave interferometry will be given in Chap. 3.

Note that the grating modulation acts along the standing-wave axis, and we are only concerned with the reduced one-dimensional z-state of the matter-waves. The latter are assumed to interact sufficiently shortly with the light field such that any transverse forces and corrections due to the finite mode waist can be safely omitted. We can therefore reduce our Mie-theory considerations to the case of an ideal standing wave with a Gaussian intensity profile.

2.3.2.1 Phase Modulation Effect

The phase modulation is described by the eikonal phase factor (2.36) for a point particle. If we neglect any z-motion during interaction time we arrive at the standing-wave expression (2.37). It is equivalent to the transformation rule $\langle z|\psi\rangle \mapsto \exp\left[i\left(\phi_0/2\right)\cos 2kz\right]\langle z|\psi\rangle$ for a given matter-wave state $|\psi\rangle$ up to a constant global phase. The term ϕ_0 denotes the eikonal phase collected at the antinodes of the standing-wave field.

Fortunately, the transformation rule can be adopted to the case of dielectric spheres of larger radii without further trouble. The reason is that, according to Sect. 2.3.1.2, the on-axis force on a dielectric sphere is always of the form $F_z\left(z\right) = -F_0\sin 2kz$, if higher-order corrections by the Gaussian mode profile are neglected. Since there are no transverse forces to be considered either, we are left in a one-dimensional situation with no non-conservative corrections. The force can be integrated to obtain an expression for the optical potential (up to an arbitrary constant), $V\left(z\right) = -\left(F_0/2k\right)\cos 2kz$. The force factor F_0 must be computed by means of the Mie formula (2.130); it will be proportional to the standing-wave intensity $I_0 = c\varepsilon_0\left|E_0\right|^2/2$ at the antinodes.

Comparing this to the point-particle model in Sect. 2.1.4.1, we must simply substitute

$$\mathfrak{Re}\{\chi\} \mapsto \frac{4F_0}{k\,|E_0|^2} =: \frac{2c\varepsilon_0}{k}\,f_0 \tag{2.133}$$

in all the eikonal phase terms ϕ_0 to generalize from point particles to finite-size spheres. Here I have removed the field intensity using the convenient notation $F_0 = f_0 I_0$ in terms of the factor f_0.

2.3.2.2 Amplitude Modulation Effect

Standing-wave gratings can modulate the amplitude of matter-waves by optical depletion if the absorption of one or a few photons ionizes, fragments, or removes a particle by other means from the matter-wave ensemble. I have discussed in Sect. 2.1.4.2 that the corresponding transmission probability can be obtained in a Poissonian model from the mean number of absorbed photons. For point particles, this quantity can be written as $\bar{n}(z) = (n_0/2)(1 + \cos 2kz)$, where $n_0 \propto \sigma_{\text{abs}} I_0$. The offset factor and the z-modulation factor are the same in this expression, and no photons are absorbed in the field nodes.

This is different in the case of larger spheres. Here we must distinguish between the offset and the standing-wave modulation. We must replace the PPP-absorption power $\sigma_{\text{abs}} I_0$ by the Mie expression $P_{\text{abs}}(z) = P_{\text{ext}}(z) - P_{\text{sca}}(z)$, as obtained from (2.127). We arrive at the form $\bar{n}(z) = n_+ + n_- \cos 2kz$ with two different coefficients $n_\pm$. The transformation $n_0/2 \mapsto n_\pm$ from the PPP-expressions given in Sect. 2.1.4.2 to the generalized form for finite spheres is done by substituting the absorption cross section, $\sigma_{\text{abs}} \mapsto 2\pi \Pi_{\text{abs}}^{(\pm)}/k^2$. The absorption terms $\Pi_{\text{abs}}^{(\pm)} = \Pi_{\text{ext}}^{(\pm)} - \Pi_{\text{sca}}^{(\pm)}$ are determined by the Mie expressions (2.128).

Putting everything together, the following grating modulation parameters must be used for spherical particles passing a thin standing-wave beam of input laser power P_L and waist w_y at the velocity v:

$$\widetilde{\phi}_0 = \frac{8 f_0 P_L}{\sqrt{2\pi}\,\hbar k v w_y}, \quad n_\pm = \frac{4\sqrt{2\pi}\,\Pi_{\text{abs}}^{(\pm)} P_L}{\hbar c k^3 v w_y}. \tag{2.134}$$

If the grating is realized by a short laser pulse of energy E_L and spot area a_L, we find

$$\widetilde{\phi}_0 = \frac{4 f_0 E_L}{\hbar k a_L}, \quad n_\pm = \frac{4\pi \Pi_{\text{abs}}^{(\pm)} E_L}{\hbar c k^3 a_L}. \tag{2.135}$$

I will mostly refer to the case of single-photon depletion, where the absorption of one photon already removes the particle from the ensemble. Then the grating transmission function (2.41), which describes the matter-wave state transformation $\langle z|\psi\rangle \mapsto t(z)\langle z|\psi\rangle$, reads as

$$t\left(z\right) = \exp\left[-n_+ + \left(i\frac{\widetilde{\phi}_0}{2} - n_-\right)\cos 2kz\right]. \tag{2.136}$$

We notice here a general complication for wavelength-sized spheres: While the position-averaged overall transmission probability decreases exponentially with the term n_+, the modulation contrast between the nodes and the antinodes of the grating depends on n_-. As seen for the exemplary case of gold spheres in vacuum-UV gratings in Fig. 2.9, the ratio $n_-/n_+ = \Pi_{\mathrm{abs}}^{(-)}/\Pi_{\mathrm{abs}}^{(+)}$ is strongly suppressed for large spheres. That is to say, a pronounced optical grating mask goes along with a massive loss of matter-wave signal in the case of wavelength-large spheres. This will impose a hard mass limitation of optical matter-wave interferometry, as will be discussed in Chap. 3.

Another limitation might arise from the decoherence associated with the increased scattering[38] of photons at large dielectric spheres. This side effect does not generalize in a straightforward manner from the point-particle case discussed in Sect. 2.1.4.3 to large spheres. The reason is that we cannot adopt the local field coupling model, which describes the momentum transfer by scattering and absorption in terms of Lindblad master equations $\mathcal{L}_{\mathrm{sca,abs}}$, if the coupling extends over a large volume. A proper description of decoherence would, for instance, require a rigorous multi-path scattering model of light at an extended dielectric object, as presented in [68]. This goes beyond the scope of the present work. As I will show later, the proposed scheme of high-mass matter-wave interferometry [41, 76] studied in the present work is already more or less confined to the subwavelength regime due to the above mentioned tradeoff between transmission and modulation at optical depletion gratings.

2.3.3 Slowing and Trapping of Microspheres by a Cavity

Let me conclude the present chapter with a final glance at the cavity-induced slowing of polarizable particles. I have started from a classical one-dimensional model of the mechanical action of a driven cavity mode on a polarizable particle in Sect. 2.1.3. There I could simulate the slowing and trapping of a strongly coupled particle in a high-finesse standing-wave cavity, as plotted in Fig. 2.2. Later I reassessed the effect in a more realistic scenario with molecules and nanoclusters, which exhibit a much weaker coupling strength and slowing rate. This led to the rigorous weak-coupling quantum model in Sect. 2.2.

We are now in a position to be able to reconsider the strong-coupling situation. Mie theory offers us the means to describe the optical properties of realistic particles that are sufficiently extended to couple strongly enough to be eventually trapped by a cavity. Let me show that it is indeed feasible in a realistic setting to trap wavelength-sized dielectric spheres crossing a strongly pumped cavity mode. The corresponding

---

[38] Decoherence by absorption becomes relevant, too, but only if the optical depletion effect requires more than one photon to be triggered.

experiments are prepared and conducted in the labs of my group in Vienna and elsewhere [77].

I resort to the exemplary case of silicon spheres ($\varrho_{Si} = 2,300\,kg/m^3$) at the IR telecommunications wavelength $\lambda = 1,560\,nm$. The reason is that the silicon material is highly refractive and almost perfectly transparent at this wavelength. No heating losses or absorption-induced diffusion need to be taken into account. I will estimate the sphere permittivity by the bulk value $\varepsilon_{Si} = 12.1$ [29]. Moreover, I will consider the following demanding but feasible resonator configuration for the cavity [27]: Two 25 mm-curved high-reflectivity mirrors shall be placed at 1 mm distance, constituting a resonator with a narrow linewidth $\kappa = 1\,MHz$. The TEM$_{00}$ standing-wave resonator mode shall have the waist $w = 40\,\mu m$, which results in the mode volume $V = 0.0013\,mm^3$. (See Appendix A.2 for details on the Gaussian mode.) It is driven by a laser with several Watts of continuous-wave input power.

For a preliminary assessment of the coupling let us assume that the silicon spheres of radius R are described by the subwavelength polarizability (2.122). Then both the cavity resonance shift and the optical dipole force depend on a single coupling rate parameter, $U_0 = -2\pi\omega\left(R^3/V\right)(\varepsilon_{Si} - 1)/(\varepsilon_{Si} + 2)$. A coupling rate of, say, $U_0 = -\kappa$ would correspond to $R = 59\,nm$. The subwavelength approximation may still seem reasonable in this case, which represents the bottom end of the strong-coupling regime. Larger spheres should also be taken into consideration. Hence, before we can continue solving the classical cavity-particle equations of motion, we must address a yet omitted issue: The effect of the particle on the cavity field.

2.3.3.1 Cavity Resonance Shift Induced by Microspheres

Throughout the preceding sections I applied Mie theory to study the optical forces and the light extinction properties of large spherical particles. The Mie ansatz is based on a stationary scattering situation: One starts from a given field configuration $\{E_0, H_0\}$ in the absence of the scatterer, which is, in principle, determined by some asymptotic boundary conditions at infinite distance. Parts of these fields are scattered off the sphere in the form of outgoing multipolar waves $\{E_{sca}, H_{sca}\}$, which do not involve the asymptotic boundary conditions.

This is where the Mie ansatz runs into problems. By construction, it cannot account for the modified boundary conditions in a finite-size resonator due to the presence of the sphere. On the other hand, we know that small refractive modifications within the resonator configuration amplify to a substantial change of the intra-cavity light that cycles many times between the mirrors. We did not run into these difficulties in the point-particle limit, since the optical dipole potential was there responsible for both the light-induced forces and the cavity resonance shift. In the present case, the optical potential cannot be deduced from the light force anymore.

One way to resolve this issue, at least to a reasonable degree of approximation, is to invoke the principles of cavity perturbation theory [78]. Let us assume that the presence of the dielectric sphere leads to a small shift of the cavity resonance frequency, $|\delta\omega| \ll \omega$, which modifies the Maxwell equations in the resonator volume,

$$\nabla \times \begin{Bmatrix} \boldsymbol{E}_0 \\ \boldsymbol{H}_0 \end{Bmatrix} = i\omega \begin{Bmatrix} \mu_0\boldsymbol{E}_0 \\ -\varepsilon_0\boldsymbol{H}_0 \end{Bmatrix} \quad \rightarrow \quad \nabla \times \begin{Bmatrix} \boldsymbol{E} \\ \boldsymbol{H} \end{Bmatrix} = i\,(\omega + \delta\omega) \begin{Bmatrix} \mu_0\boldsymbol{E}_0 \\ -\varepsilon\,(\boldsymbol{r})\,\varepsilon_0\boldsymbol{H}_0 \end{Bmatrix}.$$
(2.137)

Here I denote by $\{\boldsymbol{E}, \boldsymbol{H}\}$ the intra-cavity fields in the presence of the sphere. The permittivity $\varepsilon\,(\boldsymbol{r})$ is piecewise constant; it assumes ε_{Si} inside the sphere and unity outside. By making use of the vector identity $\nabla \cdot (\boldsymbol{a} \times \boldsymbol{b}) = \boldsymbol{b} \cdot (\nabla \times \boldsymbol{a}) - \boldsymbol{a} \cdot (\nabla \times \boldsymbol{b})$ we can combine the above four equations to obtain the two mixed identities

$$\nabla \cdot \left(\boldsymbol{H} \times \boldsymbol{E}_0^*\right) = -i\,(\omega + \delta\omega)\,\varepsilon\,(\boldsymbol{r})\,\varepsilon_0\boldsymbol{E}_0^* \cdot \boldsymbol{E} + i\omega\mu_0\boldsymbol{H}_0^* \cdot \boldsymbol{H},$$
(2.138)

$$\nabla \cdot \left(\boldsymbol{H}_0^* \times \boldsymbol{E}\right) = i\omega\varepsilon_0\boldsymbol{E}_0^* \cdot \boldsymbol{E} - i\omega\mu_0\boldsymbol{H}_0^* \cdot \boldsymbol{H}.$$
(2.139)

These, in turn, can be combined to

$$-i\nabla \cdot \left(\boldsymbol{H} \times \boldsymbol{E}_0^* + \boldsymbol{H}_0^* \times \boldsymbol{E}\right) = \omega\varepsilon_0\,[1 - \varepsilon\,(\boldsymbol{r})]\,\boldsymbol{E}_0^* \cdot \boldsymbol{E} - \delta\omega\left[\varepsilon\,(\boldsymbol{r})\,\varepsilon_0\boldsymbol{E}_0^* \cdot \boldsymbol{E} + \mu_0\boldsymbol{H}_0^* \cdot \boldsymbol{H}\right].$$
(2.140)

At this point we can explicitly use the cavity boundary conditions by integrating the expression over the resonator volume V. It follows from Gauss' theorem that the left hand side must vanish due to the vanishing boundary conditions at the mirror surfaces. We are left with an equation that determines the shift $\delta\omega$ from the fields,

$$\frac{\delta\omega}{\omega} = \frac{-\varepsilon_0 \int_{r<R} \mathrm{d}^3r\,\mathfrak{Re}\left\{(\varepsilon_{\text{Si}} - 1)\,\boldsymbol{E}_{\text{int}} \cdot \boldsymbol{E}_0^*\right\}}{\int_V \mathrm{d}^3r\,\mathfrak{Re}\left\{\varepsilon\,(\boldsymbol{r})\,\varepsilon_0\boldsymbol{E} \cdot \boldsymbol{E}_0^* + \mu_0\boldsymbol{H} \cdot \boldsymbol{H}_0^*\right\}},$$
(2.141)

where I have taken the real part to arrive at physical expressions in the end. The integral in the numerator extends merely over the polarization density $\boldsymbol{P} = \varepsilon_0\,(\varepsilon_{\text{Si}} - 1)\,\boldsymbol{E}_{\text{int}}$ inside the sphere. The denominator can be rewritten as

$$4H_{\text{f}} + \int_V \mathrm{d}^3r\,\mathfrak{Re}\left\{\varepsilon_0\,[\varepsilon\boldsymbol{E} - \boldsymbol{E}_0] \cdot \boldsymbol{E}_0^* + \mu_0\,[\boldsymbol{H} - \boldsymbol{H}_0] \cdot \boldsymbol{H}_0^*\right\},$$
(2.142)

with $H_{\text{f}} = \hbar\omega\,|\alpha|^2$ the free energy of the unmodified cavity field. We are still not able to compute $\delta\omega$ in practice since we must know the exact form of the modified fields $\{\boldsymbol{E}, \boldsymbol{H}\}$, which depend on the frequency shift, too. If we regard the sphere as a small perturbation, however, we should not only expect that the relative shift $\delta\omega/\omega$ is small, but also that the fields are hardly modified in most of the resonator volume. We can therefore neglect the addition to the field energy term in the denominator, and we can insert the Mie expression for the internal field $\boldsymbol{E}_{\text{int}}$ from Appendix A.6, to obtain the approximate formula

$$\frac{\delta\omega}{\omega} = -\frac{\varepsilon_0}{4H_{\text{f}}} \int_{r<R} \mathrm{d}^3r\,\mathfrak{Re}\left\{(\varepsilon_{\text{Si}} - 1)\,\boldsymbol{E}_{\text{int}} \cdot \boldsymbol{E}_0^*\right\}.$$
(2.143)

A tedious but straightforward calculation using the multipole expansion properties from Appendix A.5, and a few additional integration steps,[39] yield the expansion

$$\delta\omega = \frac{-\omega}{2k^3 V \left|E_0\right|^2} \sum_{\ell,m} \left[\Im\{\beta_\ell\} \left|C_{\ell,m}^{(E)}\right|^2 + \Im\{\alpha_\ell\} \left|C_{\ell,m}^{(M)}\right|^2 \right]. \qquad (2.144)$$

Here I have used that ε_{Si} is real. If we focus again on the standing-wave modulation of the resonance shift, then we can neglect higher-order corrections in the waist w of the Gaussian mode profile. The resonance shift reduces to the simple form

$$\delta\omega\left(\mathbf{r}_0\right) = \frac{1}{2} e^{-2\left(x_0^2+y_0^2\right)/w^2} \left[U^{(+)} + U^{(-)} \cos 2kz_0 \right],$$

$$U^{(\pm)} = -\frac{\pi\omega}{k^3 V} \sum_{\ell=1}^{\infty} (\pm)^\ell \, (2\ell+1) \, \Im\{\alpha_\ell \pm \beta_\ell\}, \qquad (2.145)$$

with $\mathbf{r}_0$ the position of the sphere center. The form is very similar to the expression (2.127) for the extinction power in a standing wave. It is easily checked that the two coupling rates $U^{(\pm)}$ reduce to the point-particle value in the limit of small radii, $U^{(\pm)} \approx U_0 = -2\pi R^3 \omega \left(\varepsilon_{Si} - 1\right) / \left(\varepsilon_{Si} + 2\right) V$.

Similar effective coupling rates can be defined for the on-axis z-force,

$$F_z\left(\mathbf{r}_0\right) = \hbar k U_z \left|\alpha\right|^2 \exp\left[-2\frac{x_0^2+y_0^2}{w^2} \right] \sin 2kz_0, \qquad (2.146)$$

as well as for the transverse forces $F_{x,y}\left(\mathbf{r}_0\right)$. In the latter case, the coupling rates are determined from (2.12) by the terms $F_{x,y}^{(\pm)} = -\hbar k \left|\alpha\right|^2 U_{x,y}^{(\pm)}$. All the various coupling rates $U^{(\pm)}$, U_z, $U_{x,y}^{(\pm)}$ reduce to U_0 in the limit $R \to 0$. Any substantial difference from U_0 indicates a breakdown of the point-particle approximation. I list the coupling rates of various silicon sphere sizes in Table 2.2, which was generated from a Mie calculation based on the given cavity parameters. We observe that the point-particle breakdown occurs already at relatively small radii compared to the wavelength. This is due to the large refractive index of silicon. The table also contains

---

[39] The following integral identities for spherical Bessel functions must be used [43]:

$$\int_0^X dx\, x^2 j_\ell(x)\, j_\ell(nx) = \frac{X^2}{1-n^2} \left[j_{\ell+1}(X)\, j_\ell(nX) - n j_\ell(X)\, j_{\ell+1}(nX) \right]$$

$$\int_0^X dx \left\{ \ell(\ell+1)\, j_\ell(x)\, j_\ell(nx) + [xj_\ell(x)]'\, [xj_\ell(nx)]' \right\} = \frac{nX^2}{1-n^2} \left[n j_{\ell+1}(X)\, j_\ell(nX) - j_\ell(X)\, j_{\ell+1}(nX) \right]$$

$$+ (\ell+1)\, X j_\ell(X)\, j_\ell(nX)$$

Table 2.2 Table of light coupling and extinction parameters for silicon spheres of different radii ($\varepsilon_{Si} = 12.1$) in a standing-wave cavity at the IR wavelength $\lambda = 1{,}560\,\text{nm}$

Radius	30 nm	60 nm	150 nm	200 nm	250 nm
m (amu)	1.57×10^8	1.25×10^9	1.96×10^{10}	4.64×10^{10}	9.07×10^{10}
ω_r (mHz)	3.29	0.411	0.0263	0.0111	5.68×10^{-3}
$U^{(+)}$ (MHz)	-0.130	-1.09	-23.7	-103	-24.0
$U^{(-)}$ (MHz)	-0.128	-1.02	-13.5	10.2	-122
U_z (MHz)	-0.128	-1.02	-13.5	12.0	-79.1
$U_x^{(+)}$ (MHz)	-0.130	-1.09	-23.7	-105	-75.5
$U_x^{(-)}$ (MHz)	-0.128	-1.02	-13.5	12.0	-79.1
$U_y^{(+)}$ (MHz)	-0.130	-1.09	-23.8	-101	16.9
$U_y^{(-)}$ (MHz)	-0.128	-1.02	-13.5	12.0	-79.1
$\gamma_{ext}^{(+)}$ (MHz)	2.41×10^{-3}	0.0160	5.36	56.1	208
$\gamma_{ext}^{(-)}$ (MHz)	2.41×10^{-3}	0.0160	4.74	-2.18	94.5

We assume a Gaussian mode of waist $w = 40\,\mu\text{m}$ and volume $V = 0.0013\,\text{mm}^3$

the light extinction rate parameters $\gamma_{ext}^{(\pm)} = 2\pi c \Pi_{ext}^{(\pm)} / k^2 V$, as determined by the Mie expressions (2.127) and (2.128).

We notice that the point-particle limit already fails at $R = 60\,\text{nm}$. At the same time, however, all offset terms $(+)$ and modulation terms $(-)$ of the coupling rates are practically identical for spheres smaller than $R = 200\,\text{nm}$; the cylindrical symmetry remains valid. In this quasi-conservative size regime the cavity resonance shift and the mechanical action of the light field on the spheres are fully characterized by the effective optical potential

$$V\left(\boldsymbol{r}_0\right) = \frac{1}{2}\hbar \left|\alpha\right|^2 \exp\left[-2\frac{x_0^2 + y_0^2}{w^2}\right]\left(U^{(+)} + U^{(-)}\cos 2kz_0\right). \qquad (2.147)$$

2.3.3.2 Classical Simulation of Slowing and Trapping

With the relevant parameters at hand we can finally draw our attention to the cavity-induced slowing effect in a realistic strong-coupling scenario with silicon spheres. The effect will be studied in the classical regime, far above the quantum limit of motion. Hence, I will not account for any kind of diffusion or other quantum corrections, and I base my considerations on the coupled classical equations of motion for the center-of-mass $\boldsymbol{r}_0(t)$ of the particle and the intra-cavity field $\alpha(t)$. I have derived a set of equations for the one-dimensional point-particle case in Sect. 2.1.3. Using the results from Mie theory, the Eqs. (2.30) and (2.31) can be readily generalized to the case of silicon spheres of mass $m = 4\pi \varrho_{Si} R^3 / 3$ in three dimensions,

$$\partial_t \alpha = \eta - (i\Delta + \kappa)\,\alpha$$
$$- \frac{1}{2}g\left(\sqrt{x_0^2 + y_0^2}\right)\left[iU^{(+)} + \frac{\gamma_{\text{ext}}^{(+)}}{2} + \left(iU^{(-)} + \frac{\gamma_{\text{ext}}^{(-)}}{2}\right)\cos 2kz_0\right]\alpha, \tag{2.148}$$

$$\partial_t^2 \begin{pmatrix} x_0 \\ y_0 \end{pmatrix} = \frac{2\hbar}{mw^2}|\alpha|^2\, g\left(\sqrt{x_0^2 + y_0^2}\right)\left[\begin{pmatrix} x_0 U_x^{(+)} \\ y_0 U_y^{(+)} \end{pmatrix} + \begin{pmatrix} x_0 U_x^{(-)} \\ y_0 U_y^{(-)} \end{pmatrix}\cos 2kz_0\right], \tag{2.149}$$

$$\partial_t^2 z_0 = \frac{\hbar k}{m}U_z|\alpha|^2\, g\left(\sqrt{x_0^2 + y_0^2}\right)\sin 2kz_0. \tag{2.150}$$

Here, the Gaussian profile is denoted by $g(r_0) = \exp\left(-2r_0^2/w^2\right)$. Note that the light extinction effect merely adds to the cavity loss channel since I neglect its contribution to momentum diffusion. The driving term $\eta = \sqrt{2\kappa P_{\text{in}}/\hbar\omega}$ is related to the power P_{in} of the driving laser. In the following, I shall fix the cavity-pump detuning to $\Delta = \kappa$, which is where the Lorentzian intra-cavity intensity is most sensitive to the refractive index change induced by the particle.

Table 2.2 shows that the strong-coupling condition is already fulfilled for relatively small spheres. We may restrict our considerations to the quasi-conservative size regime, where the forces are symmetric and the angular momentum $L = x_0 p_y - y_0 p_x$ is conserved. This reduces the Eqs. (2.149) and (2.150) to two equations of motion for the radius $r_0(t)$ and the axial position $z_0(t)$ in cylindrical coordinates, $\mathbf{r}_0 = (r_0, \varphi_0, z_0)$. They evolve under the forces resulting from the effective radial potential

$$V_{\text{eff}}(r_0, z_0) = \frac{\hbar|\alpha|^2}{2}g(r_0)\left(U^{(+)} + U^{(-)}\cos 2kz_0\right) + \frac{L^2}{2mr_0^2} \tag{2.151}$$

The angular coordinate follows $\partial_t \varphi_0 = L/mr_0^2$. The centrifugal barrier in the effective potential prevents particles from reaching the center of focus if they impinge on the cavity mode with a finite impact parameter. Let us, for the moment, assume that the cavity adjusts instantaneously to the presence of the particle, so that we may set $\alpha = \eta/\Omega(r_0, z_0)$, with Ω the curly-bracketed term in (2.148). We are left with a strictly conservative motion in the adiabatic potential

$$V_{\text{ad}}(r_0, z_0) = \frac{\hbar\eta^2 g(r_0)}{2\,|\Omega(r_0, z_0)|^2}\left(U^{(+)} + U^{(-)}\cos 2kz_0\right) + \frac{L^2}{2mr_0^2}, \tag{2.152}$$

and no dissipation effect can occur. The potential is positive for sufficiently large or small r_0, where the centrifugal term dominates. In between it may assume a minimum at negative values, depending on the light coupling parameters.

The adiabatic potential proves useful when discussing the conditions for radial slowing and trapping, in addition to the conventional standing-wave slowing of the z_0-coordinate which we have found in Sect. 2.1.3. A trapping of both r_0 and z_0 means
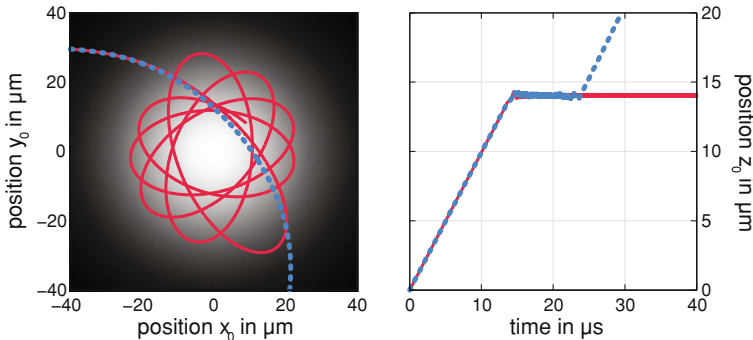
Fig. 2.14 Simulated trajectory of a silicon sphere of 60 nm radius that is captured and trapped by a Gaussian standing-wave cavity mode. All parameters are taken from Table 2.2; the initial conditions are given in the text. The xy-projection of the trajectory is plotted on the *left*, where the background shading indicates the Gaussian intensity profile of the mode. The z-component is plotted on the *right* versus time. The full simulation based on the coupled cavity-particle dynamics (*solid line*) is compared with a hypothetical trajectory (*dotted line*), where the cavity is assumed to react without delay to the particle. The simulation was run up to $t = 50\,\mu s$

that the particle is captured in the Gaussian mode and that it orbits around the center of focus $r_0 = 0$ with a constant angular momentum, while it oscillates around a field antinode along the z-direction. If we assume that the z-coordinate is already trapped then the radial coordinate evolves approximately under the one-dimensional potential $V_{ad}(r_0, 0)$. In the purely conservative case, a particle would be accelerated towards the center, $r_0 = 0$, until it hits the centrifugal barrier and gets reflected. The particle would pass the cavity on a deflected trajectory in the xy-plane.

The delayed cavity reaction modifies this adiabatic trajectory and may dissipate kinetic energy from the radial motion. For trapping to occur the parameters must be chosen such that V_{ad} exhibits a pronounced local minimum close to the centrifugal barrier into which the particle could be captured. This happens if the particle has lost enough kinetic energy to remain bounded after it has been reflected at the centrifugal barrier.

In Fig. 2.14 I plot a simulated trapping trajectory for the 60 nm silicon sphere from Table 2.2. The particle approaches the cavity with the initial velocity $v_0(0) = (10, 0, 1)$ m/s starting from the point $r_0(0) = (-200, 30, 0)\,\mu m$. The cavity is pumped with an input power of $P_{in} = 1$ W, which amounts to a steady-state number of about 8×10^{12} intra-cavity photons in the absence of the particle. This value is almost doubled as the particle gets trapped and shifts the cavity closer to resonance. The solid line in the left panel of Fig. 2.14 represents the xy-projection of the particle trajectory. (The shading of the background mimics the Gaussian intensity profile $g(r_0)$.) We find that the particle is at first deflected and then eventually trapped in a stable orbit precessing around the central cavity axis.

Notice that the centrifugal barrier keeps the particle away from the center, which explains the empty spot in the middle of the bound orbit. For comparison I have also
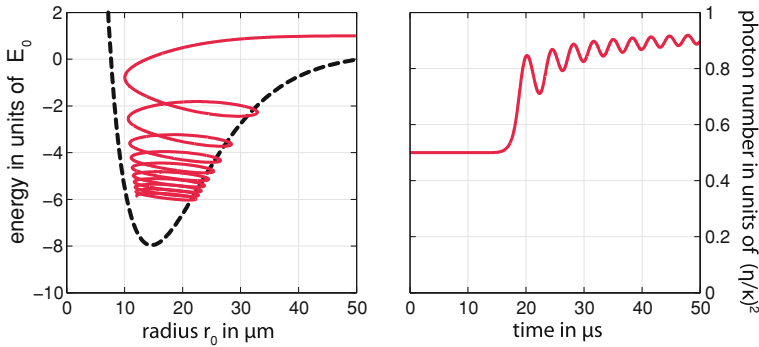
Fig. 2.15 Energy and field intensity diagrams for the simulated trajectory of Fig. 2.14. In the *left panel* we plot the total (kinetic plus potential) energy of the particle versus its off-axis distance $r_0 = \sqrt{x_0^2 + y_0^2}$ in units of its initial kinetic energy E_0. The *dashed line* represents the adiabatic potential $V_{\text{ad}}(r_0, 0)$, as defined in the text. On the *right* we plot the intra-cavity photon number $|\alpha|^2$ versus time. It is normalized to the maximum possible value $(\eta/\kappa)^2$ on resonance

plotted the strictly conservative trajectory (dotted line), which would be obtained if the particle moved under the influence of the adiabatic potential (2.152). No dissipation can occur in this case. The particle is merely deflected on its passage through the cavity. The z-component of both trajectories is plotted as a function of time on the right panel. Also here the trapping effect appears only in the simulated trajectory that includes dissipation (solid line).

The cavity-induced slowing cycles are clearly seen in Fig. 2.15. On the right panel, the above trajectory is depicted in an energy diagram. The total energy of the sphere is given by the sum of kinetic and potential energy, $E = mv_0^2/2 + V_{\text{eff}}(r_0, z_0)$. It is plotted relative to the initial value $E_0 = E(0) = m|v_0(0)|^2/2$ versus the radial coordinate r_0. We notice that the energy is dissipated over many slowing cycles while the particle orbits around the central cavity axis. The particle gets deeper and deeper trapped in a potential well approximately given by the adiabatic potential $V_{\text{ad}}(r_0, 0)$ (dashed line). At the same time, the cavity is shifted more and more towards resonance, which increases the photon number $|\alpha|^2$ towards the on-resonance value $(\eta/\kappa)^2$. The ratio between the photon number and the on-resonance value is plotted against time in the right panel. It starts at the steady-state value 0.5 corresponding to the initial detuning $\Delta = \kappa$ in the absence of the sphere.

With this I have demonstrated that the strong coupling and radial trapping of subwavelength nanospheres by a standing-wave cavity is feasible in a realistic setup. I should remark, however, that the exemplary trapping behaviour shown here does not necessarily improve when going to even larger particles with coupling rates way beyond the cavity decay rate κ. Coupling rates of the order of 100κ imply that the particle is able to shift the cavity resonance by 100 linewidths, and the initial cavity-pump detuning Δ would have to be adjusted accordingly. Otherwise the particle would simply kick the cavity out of resonance and switch off the field immediately

upon entrance. A more serious obstruction is related to the large light extinction rate that comes with the coupling. Recall that the dissipation effect can only be achieved with high-finesse resonator modes, which exhibit a long lifetime on the scale $1/\kappa$ of the intra-cavity field. This prerequisite becomes obsolete, and the cavity will effectively loose finesse, when the particle directly extincts the cavity field at a much faster rate. As a result, the particle effectively depletes the cavity by its presence.

Here ends the first part of this thesis, which contains a detailed overview of the principles and consequences of the linear coupling between polarizable objects and light. The possibility to cool and trap dielectric nanoparticles by cavity light represents one of the key results regarding potential applications in the lab. (It is in fact being implemented in the Vienna group as I write these lines.) The other key topic of this chapter, optical diffraction gratings for molecules and nanoparticles, will be applied in the next chapter on high-mass matter-wave interference methods.

References

1. S. Nimmrichter, K. Hammerer, P. Asenbaum, H. Ritsch, M. Arndt, Master equation for the motion of a polarizable particle in a multimode cavity. New J. Phys. **12**, 083003 (2010)
2. H.C. van de Hulst, *Light Scattering by Small Particles* (Dover, New York, 1981)
3. C.F. Bohren, D.R. Huffman, *Absorption and Scattering of Light by Small Particles* (Wiley, New York, 1998)
4. A.P. Kazantsev, G.I. Surdutovich, V.P. Yakovlev, *Mechanical Action of Light on Atoms* (World Scientific, Singapore, 1990)
5. S. Haroche, J.-M. Raimond, *Exploring the Quantum: Atoms, Cavities, and Photons (Oxford Graduate Texts)* (Oxford University Press, Oxford, 2006)
6. S.M. Barnett, R. Loudon, On the electromagnetic force on a dielectric medium. J. Phys. B Atomic Mol. Opt. Phys. **39**, S671 (2006)
7. B. Thidé, *Electromagnetic Field Theory (Online Version)* (Dover, New York, 2011)
8. J.D. Jackson, *Classical Electrodynamics*, 3rd edn. (Wiley, New York, 1999)
9. H.-P. Breuer, F. Petruccione, *The Theory of Open Quantum Systems* (Oxford University Press, Oxford, 2002)
10. H.M. Wiseman, G.J. Milburn, *Quantum Measurement and Control* (Cambridge University Press, Cambridge, 2010)
11. M. Gallis, G. Fleming, Environmental and spontaneous localization. Phys. Rev. A **42**, 38 (1990)
12. S. Nimmrichter, K. Hornberger, H. Ulbricht, M. Arndt, Absolute absorption spectroscopy based on molecule interferometry. Phys. Rev. A **78**, 063607 (2008)
13. H. Du, R.-C.A. Fuh, J. Li, L.A. Corkan, J.S. Lindsey, PhotochemCAD: a computer-aided design and research tool in photochemistry. Photochem. Photobiol. **68**, 141 (1998)
14. J.M. Dixon, M. Taniguchi, J.S. Lindsey, PhotochemCAD 2: a refined program with accompanying spectral databases for photochemical calculations. Photochem. Photobiol. **81**, 212 (2007)
15. K. Hornberger, J.E. Sipe, M. Arndt, Theory of decoherence in a matter mave Talbot-Lau interferometer. Phys. Rev. A **70**, 53608 (2004)
16. K. Hansen, E. Campbell, Thermal radiation from small particles. Phys. Rev. E **58**, 5477 (1998)
17. K. Hornberger, S. Gerlich, P. Haslinger, S. Nimmrichter, M. Arndt, Colloquium: quantum interference of clusters and molecules. Rev. Mod. Phys. **84**, 157 (2012)
18. P. Horak, G. Hechenblaikner, K. Gheri, H. Stecher, H. Ritsch, Cavity-induced atom cooling in the strong coupling regime. Phys. Rev. Lett. **79**, 4974 (1997)

19. M. Gangl, H. Ritsch, Collective dynamical cooling of neutral particles in a high-Q optical cavity. Phys. Rev. A **61**, 011402 (1999)
20. V. Vuletić, S. Chu, Laser cooling of atoms. Ions Mol. Coherent Scattering Phys. Rev. Lett. **84**, 3787 (2000)
21. H. Chan, A. Black, V. Vuletić, Observation of collective-emission-induced cooling of atoms in an optical cavity. Phys. Rev. Lett. **90**, 063003 (2003)
22. P. Maunz, T. Puppe, I. Schuster, N. Syassen, P.W.H. Pinkse, G. Rempe, Cavity cooling of a single atom. Nature **428**, 50 (2004)
23. S. Nußmann, K. Murr, M. Hijlkema, B. Weber, A. Kuhn, G. Rempe, Vacuum-stimulated cooling of single atoms in three dimensions. Nat. Phys. **1**, 122 (2005)
24. M. Wolke, J. Klinner, H. Keßler, A. Hemmerich, Cavity cooling below the recoil limit. Science **337**, 75 (2012)
25. B. Lev, A. Vukics, E. Hudson, B. Sawyer, P. Domokos, H. Ritsch, J. Ye, Prospects for the cavity-assisted laser cooling of molecules. Phys. Rev. A **77**, 023402 (2008)
26. C. Gardiner, P. Zoller, *Quantum Noise: A Handbook of Markovian and Non-Markovian Quantum Stochastic Methods with Applications to Quantum Optics (Springer Series in Synergetics)* (Springer, Berlin, 2010)
27. P. Asenbaum, *Private Communication* (University of Vienna, Austria, 2012)
28. B.E.A. Saleh, M.C. Teich, *Fundamentals of Photonics* 2nd edn. (Wiley, New York, 2007)
29. E.D. Palik, G. Ghosh, *Handbook of Optical Constants of Solids* (Academic Press, New York, 1985)
30. M.L. Gorodetsky, A.D. Pryamikov, V.S. Ilchenko, Rayleigh scattering in high-Q microspheres. J. Opt. Soc. Am. B **17**, 1051 (2000)
31. U. Kreibig, M. Vollmer, *Optical Properties of Metal Clusters (Springer Series in Materials Science)* (Springer, Berlin, 1995)
32. M.S. Dresselhaus, G. Dresselhaus, P.C. Eklund, *Science of Fullerenes and Carbon Nanotubes: Their Properties and Applications* (Academic Press, New York, 1996)
33. G. Lach, B. Jeziorski, K. Szalewicz, Radiative corrections to the polarizability of helium. Phys. Rev. Lett. **92**, 233001 (2004)
34. A. Miffre, M. Jacquey, M. Büchner, G. Trénec, J. Vigué, Measurement of the electric polarizability of lithium by atom interferometry. Phys. Rev. A **73**, 011603 (2006)
35. R.J. Glauber, High-energy collision theory. in *Lectures in Theoretical Physics: Lectures Delivered at the Summer Institute for Theoretical Physics* (University of Colorado, Boulder, Wiley, 1959), p. 315
36. S. Nimmrichter, *Matter Wave Talbot-Lau Interferometry Beyond the Eikonal Approximation* (Diploma thesis, Technische Universität München, 2007)
37. S. Nimmrichter, K. Hornberger, Theory of near-field matter-wave interference beyond the eikonal approximation. Phys. Rev. A **78**, 023612 (2008)
38. P.R. Berman, *Atom Interferometry* (Academic Press, San Diego, 1996)
39. A.D. Cronin, D.E. Pritchard, Optics and interferometry with atoms and molecules. Rev. Mod. Phys. **81**, 1051 (2009)
40. K. Hornberger, S. Gerlich, H. Ulbricht, L. Hackermüller, S. Nimmrichter, I.V. Goldt, O. Boltalina, M. Arndt, Theory and experimental verification of Kapitza-Dirac-Talbot-Lau interferometry. New J. Phys. **11**, 43032 (2009)
41. S. Nimmrichter, P. Haslinger, K. Hornberger, M. Arndt, Concept of an ionizing time-domain matter-wave interferometer. New J. Phys. **13**, 075002 (2011)
42. A. Turlapov, A. Tonyushkin, T. Sleator, Talbot-Lau effect for atomic de Broglie waves manipulated with light. Phys. Rev. A **71**, 043612 (2005)
43. I.S. Gradshteyn, I.M. Ryzhik, A. Jeffrey, D. Zwillinger, *Table of Integrals, Series, and Products* (Academic Press, New York, 2007)
44. S.M. Dutra, *Cavity Quantum Electrodynamics: The Strange Theory of Light in a Box* (Wiley, New York, 2005)
45. R.J. Glauber, *Quantum Theory of Optical Coherence* (Wiley, New York, 2006)
46. D. Walls, G.J. Milburn, *Quantum Optics* 2nd edn. (Springer, Berlin, 2007)

47. G.J. Milburn, Lorentz invariant intrinsic decoherence. New J. Phys. **8**, 96 (2006)
48. G. Hechenblaikner, M. Gangl, P. Horak, H. Ritsch, Cooling an atom in a weakly driven high-Q cavity. Phys. Rev. A **58**, 3030 (1998)
49. M. Poot, H.S. van der Zant, Mechanical systems in the quantum regime. Phys. Rep. **511**, 273 (2012)
50. F. Marquardt, A. Clerk, S. Girvin, Quantum theory of optomechanical cooling. J. Mod. Opt. **55**, 3329 (2008)
51. S. Gröblacher, K. Hammerer, M.R. Vanner, M. Aspelmeyer, Observation of strong coupling between a micromechanical resonator and an optical cavity field. Nature **460**, 724 (2009)
52. M. Aspelmeyer, S. Gröblacher, K. Hammerer, N. Kiesel, Quantum optomechanics-throwing a glance. J. Opt. Soc. Am. B **27**, A189 (2010)
53. P. Domokos, H. Ritsch, Mechanical effects of light in optical resonators. J. Opt. Soc. Am. B **20**, 1098 (2003)
54. S. Stenholm, The semiclassical theory of laser cooling. Rev. Mod. Phys. **58**, 699 (1986)
55. J. Cirac, R. Blatt, P. Zoller, W. Phillips, Laser cooling of trapped ions in a standing wave. Phys. Rev. A **46**, 2668 (1992)
56. K. Jaehne, K. Hammerer, M. Wallquist, Ground-state cooling of a nanomechanical resonator via a Cooper-pair box qubit. New J. Phys. **10**, 095019 (2008)
57. P. Domokos, P. Horak, H. Ritsch, Semiclassical theory of cavity-assisted atom cooling. J. Phys. B At. Mol. Opt. Phys. **34**, 187 (2001)
58. H. Risken, T. Frank, *The Fokker-Planck Equation: Methods of Solution and Applications (Springer Series in Synergetics)* (Springer, Berlin, 2008)
59. W.P. Schleich, *Quantum Optics in Phase Space* (Wiley, Berlin, 2001)
60. S. Barnett, S. Stenholm, Hazards of reservoir memory. Phys. Rev. A **64**, 033808 (2001)
61. J. Salo, S.M. Barnett, S. Stenholm, Non-Markovian thermalisation of a two-level atom. Opt. Commun. **259**, 772 (2006)
62. J. Piilo, K. Härkönen, S. Maniscalco, K.-A. Suominen, Open system dynamics with non-Markovian quantum jumps. Phys. Rev. A **79**, 062112 (2009)
63. G.D. Boyd, J.P. Gordon, Confocal multimode resonator for millimeter through optical wavelength masers. Bell Syst. Tech. J **40**, 489 (1961)
64. N. Hodgson, H. Weber, *Optical Resonators: Fundamentals, Advanced Concepts, Applications (Springer Series in Optical Sciences)* (Springer, New York, 2005)
65. P. Asenbaum, *Towards Cavity Cooling of a Molecular Beam* (Diploma thesis, Universität Wien, 2009)
66. P. Domokos, H. Ritsch, Collective cooling and self-organization of atoms in a cavity. Phys. Rev. Lett. **89**, 253003 (2002)
67. A. Black, H. Chan, V. Vuletić, Observation of collective friction forces due to spatial self-organization of atoms: from rayleigh to bragg scattering. Phys. Rev. Lett. **91**, 203001 (2003)
68. A. Pflanzer, O. Romero-Isart, J.I. Cirac, Master-equation approach to optomechanics with arbitrary dielectrics. Phys. Rev. A **86**, 013802 (2012)
69. O. Romero-isart, M.L. Juan, R. Quidant, J.I. Cirac, Toward quantum superposition of living organisms. New J. Phys. **12**, 33015 (2010)
70. D.E. Chang, C.A. Regal, S.B. Papp, D.J. Wilson, J. Ye, O. Painter, H.J. Kimble, P. Zoller, Cavity opto-mechanics using an optically levitated nanosphere. Proc. Nat. Acad. Sci. **107**, 1005 (2010)
71. B. Dalton, E. Guerra, P. Knight, Field quantization in dielectric media and the generalized multipolar Hamiltonian. Phys. Rev. A **54**, 2292 (1996)
72. S.M. Barnett, R. Loudon, The enigma of optical momentum in a medium. Philos. Trans. A **368**, 927 (2010)
73. L.D. Landau, L.P. Pitaevskii, E. Lifshitz, *Electrodynamics of Continuous Media (Course of Theoretical Physics)*, 2nd edn, vol. 8 (Butterworth-Heinemann, 1984)
74. L. Tsang, J.A. Kong, K.-H. Ding, *Scattering of Electromagnetic Waves: Theories and Applications* (Wiley, New York, 2000)
75. J.A. Stratton, *Electromagnetic Theory* (Wiley, New York, 2007)

76. S. Nimmrichter, K. Hornberger, P. Haslinger, M. Arndt, Testing spontaneous localization theories with matter-wave interferometry. Phys. Rev. A **83**, 43621 (2011)
77. O. Romero-Isart, A.C. Pflanzer, F. Blaser, R. Kaltenbaek, N. Kiesel, M. Aspelmeyer, J.I. Cirac, Large Quantum Superpositions and Interference of Massive Nanometer-Sized Objects. Phys. Rev. Lett. **107**, 20405 (2011)
78. D.M. Pozar, *Microwave Engineering* 4th edn. (Wiley, New York, 2011)

Macroscopic Matter Wave Interferometry
Nimmrichter, S.
2014, XIV, 279 p. 38 illus., 18 illus. in color., Hardcover
ISBN: 978-3-319-07096-4